Orbital outcomes of STIPs and consequences for hot-Jupiter formation and planet diversity

by

Águeda Paula Granados Contreras

B.Sc. in Physics, Universidad de Guanajuato, Mexico, 2010

M.Sc. (Astronomy), Universidad Nacional Autónoma de México, Mexico, 2013

A THESIS SUBMITTED IN PARTIAL FULFILLMENT OF

THE REQUIREMENTS FOR THE DEGREE OF

DOCTOR IN PHILOSOPHY

in

The Faculty of Graduate and Postdoctoral Studies

(Astronomy)

THE UNIVERSITY OF BRITISH COLUMBIA

(Vancouver)

November 2018

The following individuals certify that they have read, and recommend to the Faculty of Graduate and Postdoctoral studies for acceptance, the dissertation entitled:

Orbital outcomes of STIPs and consequences for hot-Jupiter formation and planet diversity

submitted by Agueda Paula Granados Contreras in partial fulfillment of the requirements for the degree of Doctor in Philosophy in Astronomy

Examining Committee:

Dr. Aaron C. Boley, Astronomy
Supervisor

Dr. Brett Gladman, Astronomy
Supervisory Committee Member

Dr. Ingrid Stairs, Astronomy
Supervisory Committee Member

Dr. Douglas Scott, Astronomy
University Examiner

Dr. Neil Balmforth, Mathematics
University Examiner

Additional Supervisory Committee Members:

Dr. Jaymie Matthews, Astronomy
Supervisory Committee Member

Supervisory Committee Member

Abstract

The discovery of exoplanets on short orbital periods ($P \lesssim 100$ days), including hot-Jupiters and Systems with Tightly-packed Inner Planets (STIPs), defies predictions from classic planet formation theory. Their existence requires either large-scale migration of planets through disks or rethinking fundamental steps in the planet formation process or some combination of both. It is further unclear whether the known STIPs harbor additional, undetected planets at even larger stellarcentric distances, which would have fundamental implications for how the systems formed. Through numerical simulations, we explore: (1) the in-situ formation of hot-Jupiters as an extreme outcome of early metastability of STIPs in the presence of gas; and (2) the dynamical effects of distant gas giants on STIPs using two case studies. In addition, we use synthetic systems to explore whether hot-Jupiters could form in-situ within dynamically unstable STIPs through the consolidation of a critical core $M \geq 10M_{\oplus}$. We compare the dynamical outcomes of gas-free and gas-embedded planetary systems, in which consolidation of a critical core was only possible in the gas-free simulations. In contrast, STIPs are resistant to instability when gas is present, resulting in coplanar and nearly circular systems. The instability of the configurations after 10 Myr increases if the eccentricity is perturbed to $e \sim 0.01$. In some cases, the planet-disk interaction produces co-orbiting planets that are stable even when the gas is removed. We explore the transit detectability of these configurations and find that the coorbital transit signature is difficult to identify in current transit detection pipelines due to the system dynamics. To explore STIP evolution in the presence of an outer giant planet, we vary the semi-major axis of the perturber between 1 and 5.2 au. We find that the presence of the outer perturber, in most locations, only alters the STIP precession frequencies but not its evolution or stability. In those locations where the perturber causes secular eccentricity resonances, the STIP becomes unstable. Secular inclination resonances can affect the observed multiplicity of transiting planets by driving the orbits of one or more planets to inclinations about $16°$.

Lay summary

The variety of exoplanets so far discovered demonstrates that astronomers do not understand planet formation as well as previously thought. In particular, the formation mechanism of planetary systems that are compact and very close to their host star remains hotly debated. My main focus is on understanding these tightly-packed planetary systems, in which there are a large multiplicity of planets, like in the Solar System, with orbits compressed within the equivalent of Earth's orbital distance to the Sun. It is also uncertain whether these systems have additional, undetected planets at much larger distances from their host star, making them like a more densely populated Solar System. With the aid of numerical simulations, I explore in this work an alternative planet-formation mechanism for short-period planets, as well as investigating how these systems would interact with a distant companion and what the observational signature might be.

Preface

The research presented here is based on numerical simulations of planetary systems using the N-body integrators `Mercury6` and the 15th-order Integrator with Adaptive Time-Stepping (`IAS15`), as described in Chapter 2. I modified the original `Mercury6` code (Chambers, 1999, publicly available) to include additional physical interactions with the star, which are described in Sections 2.1.1 and 4.1. `IAS15` is my own implementation of the Rein and Spiegel (2015) algorithm (Section 2.1.4 and 3.1.2), and it is utilized in Section 3.3. Due to the number of numerical simulations (more than 500) needed for these studies, we used the Orcinus computing cluster, provided by WestGrid (`www.westgrid.ca`) and Compute Canada Calcul Canada (`www.computecanada.ca`).

Throughout Chapter 4, the secular theory code `resmap` is employed to find the secular eigenfrequencies and eigenvectors for a given planetary system, as well as the eccentricity and inclination forcing that the system exerts on a test particle. The `resmap` code, briefly described in Section 2.2, was written by my supervisor Dr. Boley and is publicly available in `https://github.com/norabolig/resmap`.

Some of the material discussed in Sections 3.1.1 and 3.2 has been published in an article coauthored by me and led by my supervisor (Boley, A. C.; Granados Contreras, A. P.; and Gladman, B. The In Situ Formation of Giant Planets at Short Orbital Periods. Astrophys. J., Lett. 817:L17, 2016). Dr. Boley coordinated the overall project, including writing the manuscript and analyzing the bulk of the simulation output. Dr. Gladman was also involved in the conceptual development of in-situ formation of hot-Jupiters and in providing feedback for the manuscript. I set up and ran the 1000 N-body simulations for the study, helped to analyze the simulation output, and contributed to the writing of the manuscript, specifically the parts included in this thesis.

A large fraction of the material described in Chapter 4 has been previously published in a refereed journal article on which I was the lead author (Granados Contreras, A. P. and Boley, A. C. The Dynamics of Tightly-packed Planetary Systems in the Presence of an Outer Planet: Case Studies Using Kepler-11 and Kepler-90. Astron. J. 155:139, 2018). I was responsible for running the numerical simulations, analyzing the data, and writing the manuscript. Dr. Boley was involved in the interpretation of the results, as well as the writing and editing of the manuscript.

Table of Contents

Appendices

List of Tables

List of Figures

List of Acronyms

BS	Bulirsch-Stoer	26
DFT	discrete Fourier transform	43
EPE	Extrasolar Planets Encyclopaedia	4
FFT	fast Fourier transform	43
FT	Fourier transform	43
GR	general relativity	22
gSPG	gas short-period giant	45
HJ	hot-Jupiter	1
`IAS15`	15th-order Integrator with Adaptive Time-Stepping	21
K11	Kepler-11	21
K90	Kepler-90	21
MMEN	Minimum Mass Extrasolar Nebula	15
MMR	mean motion resonance	8
MMSN	Minimum Mass Solar Nebula	15
MVS	mixed-variable symplectic	26
RV	radial velocity	2
SPG	short-period giant	46
STIP	System with Tightly-packed Inner Planets	2
TDV	transit duration variation	94
TPS	Kepler Transit Planet Search pipeline	67
TTV	transit timing variation	3
WJ	warm-Jupiter	11

List of symbols

$\mathcal{P}_{\mathrm{tr}}$	transit detection probability
R_*	stellar radius
R_{p}	planetary radius
M_*	stellar mass
M_{p}	planetary mass
P	orbital period
a	semi-major axis
e	eccentricity
I, i	orbital inclination (not to be confused with the subindex i)
ϖ	longitude of pericenter
Ω	longitude of the ascending node
$\mathcal{M}$	mean anomaly
λ	mean longitude (if not otherwise stated)
	characteristic disk density decay timescale
K	radial velocity (RV) amplitude
G	gravitational constant
T	temperature
r	stellarcentric distance
N_{p}	number of planets in a system or configuration
R_{mH}	mutual Hill radius
μ	planet-star mass fraction
$\eta = f$	semi-major axis difference between two planets in units of R_{mH}
σ_{solids}	disk surface density of solids
σ_{gas}	disk surface density of gas
$\mathcal{F}_{\mathrm{disk}}$	total disk mass relative to the MMSN
Z_{rel}	disk metallicity relative to the MMSN
$\mathbf{F}_{\mathrm{D}}$	drag force
C_{D}	drag coefficient
ρ	density
s	particle's radius
$\mathbf{v}$	velocity relative to gas

b	effective cross sectional radius
v_{esc}	escape velocity
σ_v	velocity dispersion between objects
$\mathcal{F}_{\mathrm{g}}$	gravitational focusing
Σ_{p}	surface density of a swarm of planetesimals
$\dot{M}$	mass growth rate
$\Omega_{\mathrm{p}} = n$	orbital frequency or mean motion of a planet
M_{iso}	isolation mass
$\sigma_\rho(r)$	surface density of solids at a stellarcentric distance r
$\mathbf{a}_{\mathrm{GR}}$	General Relativity corrected acceleration vector
c	speed of light
$\mathbf{a}_{\mathrm{TD}}$	gaseous tidal damping acceleration vector
$\mathbf{v}$	velocity vector
$\boldsymbol{\rho}$	radial component of the position vector in cylindrical coordinates
$\hat{\mathbf{k}}$	unit vector of the vertical component
v_ρ	magnitude of velocity vector's radial component (in cylindrical coordinates)
v_z	magnitude of velocity vector's vertical component (in cylindrical coordinates)
τ_e	eccentricity damping timescale
τ_i	inclination damping timescale
v_{c}	circular Keplerian velocity
τ_{wave}	characteristic wave time
c_{s}	isothermal sound speed
$\mathcal{R}$	gas constant
τ_{local}	local τ_{wave} scaled at 1 au
H	disk scale height
$\tau_o^{1\mathrm{au}}$	scaled value of τ_{local} at 1 au
$\sigma^{\mathrm{MMEN}}(\rho)$	MMEN surface density at a radial distance ρ
$\mathbf{a}_{\mathrm{mig}}$	migration acceleration vector
τ_{mig}	migration timescale at 1 au
$\mathbf{r}$	position vector in Cartesian coordinates
$\dot{\mathbf{r}}$	velocity vector in Cartesian coordinates
(q, p)	canonical variables, generalized coordinates and momenta
t	time variable
τ	timestep variable
$\mathcal{H}$	Hamiltonian
$K(r_{ij})$	factor to account for close encounters in Mercury6's hybrid integrator
E	error term of an approximation (in this case the Gauss-Radau quadrature)
$P_n(x)$	Legendre polynomials of order n
h_n	n-spacing of Gauss-Radau quadrature

g_k	integration constants of the `IAS15`
b_k	integration constants of the `IAS15`
U_k	central potential felt by mass m_k
$\mathcal{R}_k$	disturbing function of mass m_k
μ_k	product of gravitational constant and mass m_k
α_{ij}	ratio of semi-major axis of particle/body i and j
$\bar{\alpha}_{ij}$	conditioned semi-major axis ratio
$\mathcal{R}_{\mathrm{D}}$	direct part of the disturbing function
$\mathcal{R}_{\mathrm{I}}$	indirect part of the disturbing function due to an internal perturber
$\mathcal{R}_{\mathrm{E}}$	indirect part of the disturbing function due to an external perturber
$b_s^{(k)}(\alpha_{ij})$	Laplace coefficients
A_{ij}	elements of the secular matrix $\mathbf{A}$ associated with e and ϖ
B_{ij}	elements of the secular matrix $\mathbf{B}$ associated with I and Ω
(h_i, k_i)	eccentricity vector of particle/body i
(p_i, q_i)	inclination vector of particle/body i
g_l	eigenvalues of the secular matrix $\mathbf{A}$ of mode l
β_l	phase associated with g_l
f_l	eigenvalues of the secular matrix $\mathbf{B}$ of mode l
γ_l	phase associated with f_l
e_{free}	free eccentricity of a test particle
I_{free}	free inclination of a test particle
$\mathcal{F}_t[f(t)](\nu)$	Fourier transform (FT)
$\mathcal{F}_k[f_k{}_{f=0}^{N-1}](n)$	discrete Fourier transform (DFT)
ν	linear frequency
A_n	amplitude of the FT
ϕ	phase of the FT
	offset angle between two planets (as seen from the central mass)
s_i	difference of semi-major axes of two coorbiting planets at time i
$H(\phi)$	function of the angle between two coorbiting planets
W	average arc length of a coorbiting planet
s_{180}	difference in semi-major axes of two planets when separated by $\phi = 180°$
ϕ_{min}	minimum angle between two coorbiting planets
R_{l}	radius of the larger planet in a coorbital configuration
R_{s}	radius of the smaller planet in a coorbital configuration
q, Q	pericenter and apocenter values of a planet, respectively
$\dot{\Omega}, \dot{\varpi}$	nodal and apsidal precession frequencies
$P_{\mathrm{node}}, P_{\mathrm{ap}}$	nodal and apsidal precession periods
φ	resonant angle between two planets

Acknowledgments

I acknowledged my supervisory committee for their support and patience after a few changes in the delivery of this thesis. I am grateful to my supervisor, Dr. Aaron Boley, for his support, feedback, time, comments, and patience. Also to Dr. Brett Gladman for his comments and suggestions on my research and simulations.

I am grateful to my parents for their support and for raising me as a strong and independent individual. I could not have gotten this far without them.

This research has made use of the NASA Exoplanet Archive, which is operated by the California Institute of Technology, under contract with the National Aeronautics and Space Administration under the Exoplanet Exploration Program.

Chapter 1

Introduction

Throughout history, astronomers and planetary scientists have been intrigued by the formation and evolution of planets. Before the discovery of 51 Peg b by Mayor and Queloz (1995), which is the first confirmed extra-solar planet (exoplanet) orbiting a main-sequence star, planet formation theory focused on explaining the origin of the Solar System (Lissauer, 1993). However, the characteristics of 51 Peg b required a general re-examination of planet formation theory. The planet is similar to Jupiter ($M_{\mathrm{p}} = 0.47\,M_{\mathrm{J}}$), but has an orbital period 1000 times shorter ($P = 4.27$ days). The surface temperature of 51 Peg b is expected to be as high as 1300 K, due to its short orbital distance of 0.05 au, or 8 times closer to its star than Mercury is to the Sun. The planet became the first of a new class of planets: hot-Jupiters (HJs). At the time, Mayor and Queloz (1995) suggested that 51 Peg b formed at ~ 5 au and then migrated inward by two orders of magnitude in semi-major axis to reconcile its location with standard ideas for giant planet formation.

All modern planet formation theories posit that planet building takes place in young circumstellar disks of gas and dust (a protoplanetary disk) (Lissauer, 1993; Armitage, 2007; Raymond, 2010; Perryman, 2011, and references therein). These disks arise as a natural consequence of the gravitational collapse of interstellar material, in which high-angular momentum gas and dust cannot fall directly onto the newly-forming star. Although the details are not understood, planetesimals form from small solid condensates in the disk, as well as any dust that survived the disk formation process. Depending on a number of different factors, including the efficiency of planetesimal formation, the growth of planetary embryos, and the availability of gas, a range of planetary types is possible. In this scenario, the planet's birth location with respect to the host star is of importance (Pollack et al., 1996), because the protoplanetary disk temperature generally decreases with increasing distance from the star. This causes chemical differentiation among both gaseous and solid disk materials to be a function of stellar distance. Depending on the details of the disk, condensation thresholds can lead to rapid changes in the availability of solids, particularly ices, in some portions of the disk. Thus, some disk regions could favor the rapid growth of planetary cores. This framework works well for explaining the Solar System's architecture, which is divided into an inner and outer system, delineated by planetary size and composition. Rocky small planets make up the inner Solar System, while only gas and ice giants are found in the outer system. For context, all Solar System giant planets are between 5 and

30 times more distant from the Sun than is Earth. The discovery of massive planets at short orbital periods, such as 51 Peg b, was therefore a surprise, when considering the ideas built on Solar System formation theory.

While short-period giants are fairly rare, short-period planets are not. Several different exoplanet surveys have been carried out, using multiple detection techniques, with the most successful being the transit and radial velocity (RV) methods. As of May 31, 2018, 3735 planets have been discovered and confirmed (NASA Exoplanet Archive, 2018). The orbital period distribution of the known exoplanets shows that 80% have a $P \leq 100$ days. According to observations, most of the stellar hosts with planets detected have a single confirmed planet (78%), while 614/2825 of stellar host have two or more planets. From these multiplanet systems, around 20% are tightly packed, which means that three or more planets in the system have orbital periods shorter than 100 days (Schneider et al., 2011). These Systems with Tightly-packed Inner Planets (STIPs) can have a range of planetary masses, and are inherently different from the Solar System's inner configuration. The fraction of extrasolar systems with planets on short orbital periods is non-negligible,[1] and it is now clear that the formation theory based on the Solar System is either incomplete or inadequate to address the diversity of exoplanets.

Several questions have arisen from the discovery of exoplanets, such as: why is the Solar System so different from the observed extrasolar planetary systems? What is missing in the formation mechanisms developed to date? How do short-period giant planets get to their current locations? Are there more distant (undetected) planets in the systems already discovered? Are there other formation mechanisms that we should explore?

As a consequence of these open questions, the formation scenario of STIPs is hotly debated, with two basic mechanisms in the literature: in-situ assembly/formation and planet migration (see Raymond et al., 2014, for a review). In the planet migration scenario, giant planets form at disk distances at which water can condense (i.e., beyond the water ice line) and then migrate inwards due to interactions with the gaseous disk or due to dynamical interactions followed by tidal circularization. Initially, planet migration seemed to be the only viable formation mechanism, particularly for gas giants, due to the inferred lack of materials for planet building at short orbital periods (Lin et al., 1996). However, as will be discussed in the following section, the frequency of planets in or near period commensurabilities, a fundamental prediction of convergent migration, is lower than expected in STIPs (e.g., Hands et al., 2014; Fabrycky et al., 2014). Recent work has also shown that disks could be massive enough to form planets at short orbital periods, especially if small solids migrate inward first due to aerodynamic drag (Hansen and Murray, 2012; Boley et al., 2014; Tan et al., 2015).

In the following sections, we will provide a summary of the cumulative characteristics of the

[1]In the solar neighborhood the occurrence rate of HJs is a tenth that of STIPs. This point will be discussed further throughout Sects. 1.1.1 to 1.1.3.

detected exoplanets (Sect. 1.1), as well as a description of the classical formation mechanism of terrestrial and giant planets (Sect. 1.2). Emphasis will especially be placed on planet configurations with short orbital periods and their formation and evolution. We will test the in-situ formation of short-period giant planets through numerical simulations (Chap. 3) based on stability considerations discussed in Sect. 1.1.4.

1.1 Exoplanets

The number of known and confirmed exoplanets has increased markedly since the discovery of the first set of exoplanets orbiting the millisecond pulsar PSR B1257+12 (Wolszczan and Frail, 1992). To date, we know about 4000 exoplanets, with different orbital periods, sizes and masses. Of these planets, 2919 were detected using the transit method, 673 using radial velocities (RVs), 60 using microlensing, 15 using transit timing variations (TTVs) and 68 with other techniques (NASA Exoplanet Archive, 2018). The most efficient detection method for exoplanets so far has been the transit method, with the *Kepler* mission making the largest contribution.

In the transit method, photometric monitoring of a star looks for periodic decreases in the stellar flux, which could be due to a planet passing in front of the star. The orbital period and the planet-to-star size ratio can be measured directly from the observed lightcurves. If the stellar size and mass are known, then the candidate's orbital semi-major axis and planetary radius can be derived. The transit detection probability averaged over the orbit orientation is given by

$$\begin{aligned} \mathcal{P}_{\rm tr} &= \frac{R_* + R_{\rm p}}{a\,(1-e^2)}, \\ &\approx \frac{0.24}{1-e^2}\left(\frac{P}{\rm day}\right)^{-2/3}\left(1+\frac{R_{\rm p}}{R_\odot}\right), \end{aligned}$$

where $R_\odot$ and $R_{\rm p}$ are the solar and planetary radii, a is the planetary semi-major axis, and e and P are the orbital eccentricity and period. For a given stellar size, larger planets at short orbital periods are more likely to be detected with this technique. In addition, the transit method is biased towards configurations with low mutual inclinations due to the near edge-on geometry necessary to observe a transit.

The RV approach, which is the second most successful detection method, relies on measuring variations in the star's motion along the observer's line-of-sight (i.e., the radial motion with respect to the observer). As the planet and the star orbit each other, the stellar motion leads to periodic Doppler shifts in the measured locations of stellar atmospheric absorption features. In the case of a single planet, those variations can be characterized by a period and an amplitude, where the RV amplitude is given by

$$
\begin{aligned}
K &= \left(\frac{2\pi G}{P}\right)^{1/3} \frac{M_\mathrm{p} \sin I}{(M_* + M_\mathrm{p})^{2/3}} \frac{1}{\sqrt{1-e^2}}, \\
&\propto M_\mathrm{p} \sin I \, P^{-1/3},
\end{aligned}
$$

in which M_p and M_* are the planetary and stellar masses, G the gravitational constant and I is the angle between the orbital plane's normal and the line-of-sight. For a given stellar mass, the RV method is most sensitive to massive planets and to planets at short-orbital periods. With the observed amplitude and period, the product $M_\mathrm{p} \sin I$ can be determined, assuming the stellar mass is known and that $M_* \gg M_\mathrm{p}$. The planetary mass itself can only be derived if the orbital inclination is measured separately. It would seem that for both detection methods, a large eccentricity increases the likelihood of detecting a planet, especially for the transit method. Nonetheless, a large eccentricity reduces the transit duration, depending on the observed phase of the orbit, due to its dependence on $1-e$ for a given planetary mass and orbital period. In either technique, there are additional variables that affect the planet detection, e.g., the age of the star and the presence of more than one planet in the system.

There are different online databases that keep track of the orbital parameters of the newly found exoplanets, e.g., NASA Exoplanet Archive (2018), Extrasolar Planets Encyclopaedia (EPE)[2] (Schneider et al., 2011) and the Exoplanet Orbit Database[3], which are meant to facilitate the statistical analysis of exoplanets. The total number of planets that each database provides depends on their definition of a confirmed planet and whether they also include candidates. As an example, according to the NASA Exoplanet Archive (2018), there are 3735 confirmed planets (updated to May 31, 2018), while the EPE cites 3781. From these nearly 4000 confirmed planets, to date, there are 973 planets with measured masses, 449 with $M_\mathrm{p} \sin I$ measured and 2953 with measured radii (NASA Exoplanet Archive, 2018). Only a small fraction of planets, around 10% of the total confirmed planets, have both mass and size independently determined (Chen and Kipping, 2017; NASA Exoplanet Archive, 2018).

1.1.1 Characteristics of detected planets.

In this section, we describe some of the characteristics of the exoplanet population. The data presented here come from a variety of sources, including published journal articles and exoplanet databases (Schneider et al., 2011; Wright et al., 2011; Han et al., 2014; NASA Exoplanet Archive, 2018). Special attention is paid to the distribution of orbital periods, planetary sizes and masses. The planetary densities are only known for some exoplanets, as independent mass and radius measurements are needed. For those planets that do have inferred densities, it is possible to

[2] `http://www.exoplanet.eu`
[3] `http://www.exoplanets.org`

constrain the planet's bulk composition.

The *Kepler* mission's discoveries have demonstrated that planetary systems with multiple planets on short orbital periods are common. Among the *Kepler* candidates, 23% of the host stars harbor multiple planet candidates; and 46% of all candidates reside in known multiplanet systems (Burke et al., 2014). For the solar neighborhood, the frequency of planets at short orbital periods is between 30 and 50% (Howard et al., 2012; Mayor et al., 2011), suggesting that short-period multiplanet systems may be present around at least 5% of stars in the solar neighborhood. Likewise, distributions for planetary sizes and masses are emerging for these planets (Fig. 1.1), and demonstrate that planets with periods $P < 100$ days are diverse in size, mass, and composition (see Wright et al., 2011).

The masses and sizes shown in figures throughout this introduction will be given in Jupiter units. The conversion factors between Jovian and terrestrial size and mass are $R_\oplus \approx 0.09\, R_\mathrm{J}$ and $M_\oplus \approx 0.003\, M_\mathrm{J}$.

Fig. 1.1 shows the orbital periods, planetary masses and radii of the available confirmed planets and planet candidates in the EPE. This plot includes the combination of observables from the transit and RV techniques, the strong biases inherent to these detection techniques have not been removed from the presented data. The top panel displays the orbital period distribution of: (1) all the exoplanets in the database with measured periods (black solid line); and (2) Jupiter analogues (planets with $0.1 < M_\mathrm{p} < 60\, M_\mathrm{J}$ and $R_\mathrm{p} > 0.5\, R_\mathrm{J}$). Different features are identified in the period distributions. The majority of the detected planets have a period shorter than 100 days, regardless of their size or mass. There is also a distinctive peak at 3 days for the Jupiter analogue population, commonly known as the "3-day pileup" (e.g. Udry et al., 2003; Gaudi et al., 2005; Cumming et al., 2008), which is absent in the complete exoplanet population (Howard et al., 2012; Fressin et al., 2013). This apparent pileup is meaningful for some migration-driven formation mechanisms of HJs (Rasio and Ford, 1996; Weidenschilling and Marzari, 1996; Fabrycky and Tremaine, 2007; Beaugé and Nesvorný, 2012). The counts of both populations drop for $1 < P < 4$ d, which seems to be a physical cutoff rather than observational bias (Cumming et al., 2008).

The planetary size and mass distributions are shown on the right of Fig. 1.1. After almost 30 years of exoplanet detection, it is clear that exoplanets come in a variety of sizes and masses, ranging from a few lunar-radii to radii greater than 1 R_J,[4] and from lunar-mass objects

[4] Objects with sizes above 2 R_J are problematic to explain using solely the equation of state that describes gas giant planets (Zapolsky and Salpeter, 1969). The corresponding mass-radius relationship has a critical mass of around 3 M_J which correlates to a maximum radius of 1 R_J. In general, intrinsic or extrinsic heating mechanisms could explain the slow cooling and contraction of these enlarged planets (for a description of these heating mechanisms, see Ginzburg and Sari, 2016), but not sizes much larger than about 2 R_J.

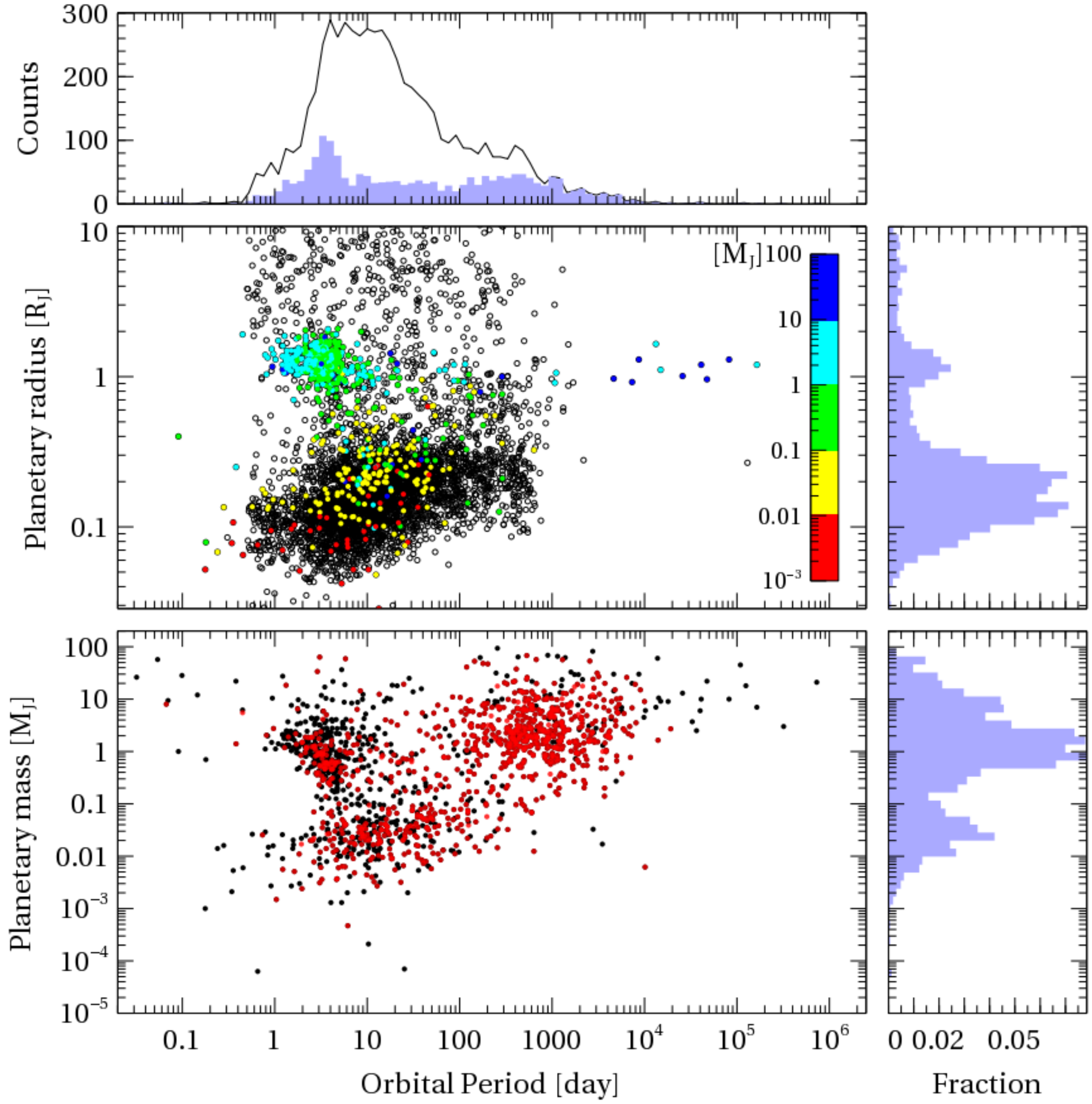

Figure 1.1: Planetary sizes and masses as a function of orbital period of confirmed and candidate extrasolar planets. The data from `exoplanet.eu` includes 3781 confirmed and 2723 candidate planets Schneider et al. (2011). *Top panel:* orbital period distribution of all objects with measured periods (black line) and of Jupiter analogues ($0.1 < M_{\rm p} < 60\,M_{\rm J}$ and $R_{\rm p} > 0.5\,R_{\rm J}$). *Middle panels:* planetary size as a function of orbital period (left) along with the planet size distribution (right). The colored circles correspond to planets with both mass and radius measured while the open circles have only the planet's size measured. The colorbar indicates the planet mass range in Jovian masses. Red shows Earth-mass planets, yellow Neptune-mass planets, green Saturn-mass planets, cyan Jovian mass planets, and blue brown dwarfs. Notice that the objects with $P > 2000$ days have masses larger than $1\,M_{\rm J}$. On the histogram on the right, the planet size distribution shows two clear peaks at $0.17\,R_{\rm J}$ and $1.1\,R_{\rm J}$. *Bottom panels:* measured planetary masses as a function of the orbital periods. The red circles indicate measurements of $M_{\rm p} \sin I$. The histogram at the right is the observed mass distribution in Jupiter masses. There are two peaks again the distribution, this time at $0.025\,M_{\rm J}$ and $1.2\,M_{\rm J}$.

($M_\mathrm{p} \sim 10^{-5}\,M_\mathrm{J}$) up to few tens of M_J[5] in mass. Both distributions present two prominent peaks. The primary peak in the size distribution is located at $\sim 0.17\,R_\mathrm{J} \approx 1.8\,R_\oplus$, while a secondary peak is at $1.1\,R_\mathrm{J} \approx 12R_\oplus$. A recent analysis of the size distribution of the *Kepler* planets, as part of the California-Kepler Survey, found that the there is a deficit of planets with sizes between $1.5 < R_\mathrm{p}/R_\oplus < 2.0$ (Fulton et al., 2017).

The mass distribution (either M_p or $M_\mathrm{p}\sin I$) peaks at $0.025\,M_\mathrm{J} \approx 8\,M_\oplus$ and at $1.2\,M_\mathrm{J}$, with a higher cumulative fraction of planets within the larger mass range. The mass and size distributions both have peaks that are separated by a valley at $0.13\,M_\mathrm{J} \approx 40\,M_\oplus$ and $0.4\,R_\mathrm{J} \approx 4\,R_\oplus$, respectively, which seems to distinguish the giant planets from all other types.

When the mass, size and orbital period distributions are considered altogether, small planets at short orbital periods are more common than giants planet at those same periods (Howard et al., 2010; Mayor et al., 2011). Furthermore, Jupiter-mass planets are divided into short-period and long-period groups, with a gap between 20 and 100 days. The planets with a measured mass and/or radius are shown in the size versus orbital period plot in Fig. 1.1. The planets with solely a measured size are indicated in open circles, while the colored points indicate different ranges of mass. Earth-like planets would correspond to red points and sizes $\lesssim 0.1\,R_\mathrm{J}$. The density of bigger and more massive planets is easier to determine than smaller planets in the same period range. Nonetheless, a combination of observations and planet interior models suggests that rocky planets have sizes $R_\mathrm{p} < 1.6\,R_\oplus$ or $< 0.14\,R_\mathrm{J}$ (Rogers, 2015).

Exoplanet surveys have shown that about 40% of the planets reside in systems with multiple members ($N_\mathrm{p} \geq 2$), which, as previously noted, means that 20% of host stars have two or more planets. Table 1.1 presents a summary of the number of stellar hosts with a given planet multiplicity. The different values, corresponding to two different exoplanet databases, depend on the planet's status and also whether all candidates suspected to orbit a single star have been confirmed. Low eccentricities (Wright et al., 2009) and planets with small sizes (Latham et al., 2011) characterize a significant number of multiplanet systems, or multis. Giant planets have also been observed in multis, but at a lower occurrence rate. More recently, Weiss et al. (2018) found that the planet sizes and spacings in multiplanet systems are correlated, meaning that neighboring planets are likely to have similar sizes and have regular spacings.

Although there are similarities among multis, there are also clear differences, particularly in the orbital distributions. Fig. 1.2 shows the period ratio distribution for systems[6] in the EPE. All possible planet combinations within systems are included. The period ratio distribution provides a way to test formation theories because disk migration models predict that planet

[5]The upper limit in mass used by the EPE for planets is $60\,M_\mathrm{J}$, based on a revised density-mass relationship for planets, brown dwarfs and stars. Gas giant planets and brown dwarfs seem to follow the same relation, which has a clear cutoff at $60\,M_\mathrm{J}$ (Hatzes and Rauer, 2015). Brown dwarfs are typically thought to have a lower mass limit of $13M_\mathrm{J}$ based on the deuterium fusion limit (Burrows et al., 2001).

[6]Confirmed planets and planet candidates.

Multiplicity	No. of stellar hosts with given planet multiplicity		
	Confirmed		Confirmed + candidate
	NASA	EPE	EPE
1	2174	2193	4291
2	399	419	550
3	136	139	152
4	51	46	52
5	20	16	16
6	6	8	9
7	1	1	1
8	1	1	1
Total	2788	2823	5071

Table 1.1: Multiplicity of extrasolar planetary systems. The second column shows the number of systems with a given multiplicity, according to the NASA Exoplanet Archive (2018), accessed in May 2018. The third and fourth columns correspond to the EPE (Schneider et al., 2011), accessed in May 2018.

pairs should tend to be trapped in or near mean motion resonances (MMRs), particularly first-order resonances (Goldreich and Tremaine, 1980; Lee and Peale, 2002). Dynamically important commensurabilities are indicated in Fig. 1.2 with dotted lines. There are indeed weak features for period ratios in or near first-order MMRs (Lissauer 2011), i.e., commensurabilities of the form $k+1{:}k$, which means that the inner planet completes $k+1$ orbits when the outer planet completes k orbits. Moreover, Fig. 1.2 shows that a pattern seems to surface near the 2:1 and 3:2 MMRs, where at slightly shorter period ratios there is a count deficit, followed by an overabundance at slightly larger commensurabilities. Some recent studies have been able to reproduce this pattern using either the disk migration theory, but accounting for planetary eccentricity (Goldreich and Schlichting, 2014), or accounting for interactions with the planetesimal disk (Chatterjee and Ford, 2015). Nevertheless, the majority of planet pairs are not in a resonance. Altogether, this suggests that disk migration may be occurring, but may not be the only (or even the dominant) mechanism for the existence of planets on short orbital periods.

In the sample of confirmed and candidate planets, there are six pairs with period ratios close to 1 ± 0.06, which suggest that either these pairs are strongly coupled or that they share the same orbit. Three of the pairs have been confirmed: Kepler-132 b and c; Kepler-271 d and b (Lissauer et al., 2012; Rowe et al., 2014; Morton et al., 2016); and Kepler-1625 b and Kepler-1625 b I (Teachey et al., 2018). The Kepler-132 and Kepler-271 stars might have a bound stellar companion, and therefore the pairs might not orbit the same star. In the case of Kepler-1625 b I, the transit signature is thought to be the first detection of an exomoon (extrasolar moon) (Teachey et al., 2018; Teachey and Kipping, 2018; Heller, 2018). The status of the other three pairs (K06242.02 and K06242.03, K00521.01 and K00521.02, K02248.04 and K02248.01) remain unknown at this time. In Sect. 3.4, we will discuss 1:1 MMRs further.

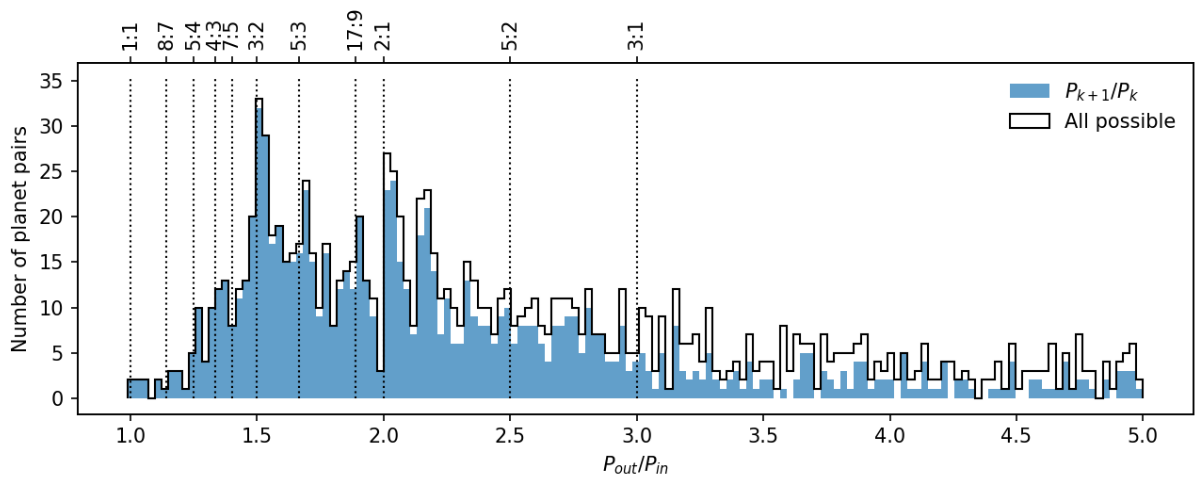

Figure 1.2: Exoplanet period ratio distribution of all possible combinations among the planets in their respective system (black line) and with the nearest neighbor (in blue). The label $P_{\rm out}/P_{\rm in}$ indicates that the period ratio shown is that of an outer planet to that of an inner planet, and therefore it is always larger than 1. Confirmed and candidate planets are included in this plot. Planets seem to avoid exact first-order MMRs, but do concentrate at slightly longer period ratios.

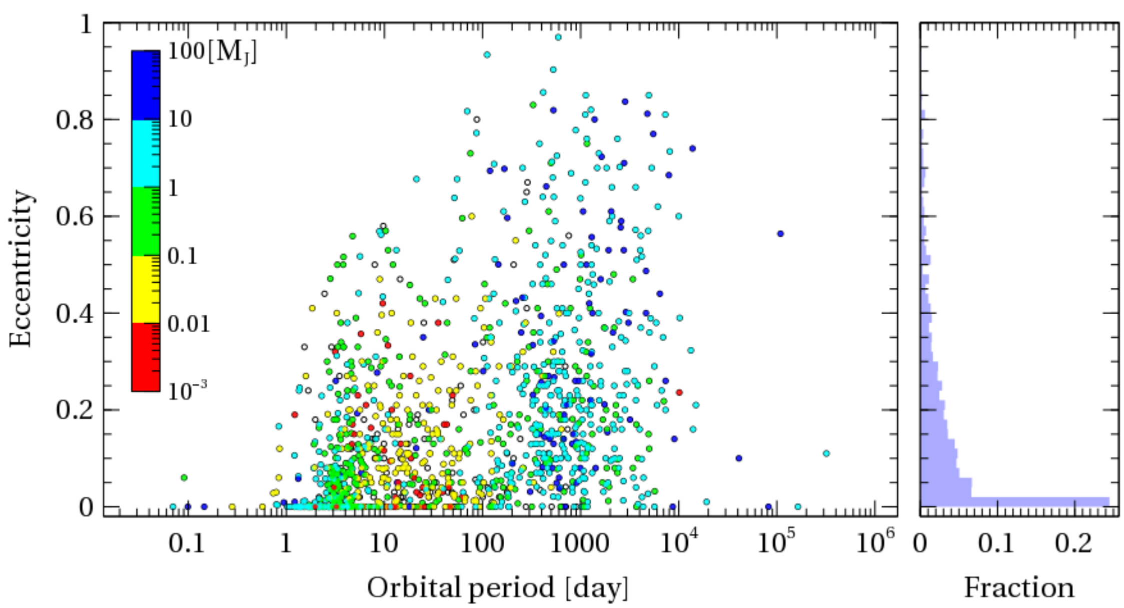

Figure 1.3: Measured eccentricities versus orbital periods of detected exoplanets (data obtained from Schneider et al., 2011). The different colors indicate the measured mass of each planet in Jupiter masses, as shown in the colorbar. There is a significant fraction (24%) of planets with nearly zero eccentricity, as shown on the right histogram.

Eccentricity and inclination are two orbital elements that can also be constrained from observations, although they require more detailed observations and modeling than for determining the period. The majority of the measured eccentricities were obtained with the RV technique. However, it is also possible to estimate the eccentricity of transiting planets from transit durations and TTVs, if the period, stellar size and impact parameter are known (Winn and Fabrycky, 2015). Fig. 1.3, shows the exoplanet eccentricity distribution as a function of orbital period. The different colors indicate the planetary mass in Jovian units. A significant fraction of exoplanets are consistent with circular orbits (right panel), with smaller planets tending to have lower eccentricities (Wright et al., 2009; Mayor et al., 2011). Giant planets (green to dark blue) have a wider range of eccentricities, especially those with long orbital periods. The eccentricity distribution spans from 0 to 1 and the typical eccentricity decreases with decreasing period. This trend may result from a combination of physical phenomena, along with RV detection bias against $e \gtrsim 0.6$, which is due to poor data sampling at periastron when eccentricities are large (Cumming, 2004). In Fig. 1.3 there is a sharp edge at about 1 day. For shorter periods, all eccentricities are zero,[7] regardless of their mass, which is usually attributed to tidal circularization (Ogilvie, 2014). Fabrycky and Tremaine (2007) suggested a Kozai cycle[8] with tidal friction during phases of high eccentricity to explain the shape of the upper boundary in the distribution. In this mechanism, planets with an inclined companion are driven to a high mutual eccentricity by Kozai cycles, and suffer periodic close approaches with the star. During the close approach, the tidal forces cause the planet to heat, which is then dissipated gradually. The energy dissipation decreases the eccentricity and semi-major axis (and therefore the period) over time.

The determination of the orbital inclination of exoplanets is of importance, mainly for RV detection and mass estimation. Furthermore, the mutual inclination of planets in multis is of interest to planet formation theory. The low mutual inclinations in the Solar System are attributed to its formation from a rotating disk. Neither the transit nor the RV techniques are particularly sensitive to mutual inclinations. Fabrycky et al. (2014) found that the *Kepler* multiplanet systems have mutual inclinations smaller than a few degrees, and are consistent with a Rayleigh distribution[9] with $\sigma_{\mathrm{I}} \approx 1.8°$. Several observational and dynamical studies comparing the mutual inclinations of the *Kepler* multiplanet and single-planet systems observed differences among both distributions, in which the best fit for the multis was inconsistent with the best fit for the singles (Lissauer et al., 2011b; Johansen et al., 2012; Hansen and Murray, 2013; Ballard and Johnson, 2016). As result, the singles are thought to belong to two different populations: some part of a flat system in which only the innermost planet transits, while others are part

[7] Except for PSR J1719-1438 b, with a mass similar to Jupiter, an orbital period $P = 0.090706293$ d and an eccentricity $e < 0.06$ (Bailes et al., 2011). PSR J1719-1438 b is thought to be a white dwarf rather than a planet, due to its density.

[8] The Kozai cycles occur when the orbit of a binary system is perturbed by a third distant object, which causes the libration of the argument of pericenter. This libration is observed as a cyclic exchange of the eccentricity and inclination.

[9] The Rayleigh distribution has the functional form:

$$f(x;\sigma) = \frac{x}{\sigma^2} \mathrm{e}^{-x^2/2\sigma^2}$$

being σ the mode of this distribution.

of a low multiplicity system or a system with much higher mutual inclinations (Lissauer et al., 2011a).

The orbital inclination with respect to the stellar spin axis has been determined for a few multiplanet systems using the Rossiter-McLaughlin effect.[10] Most of the measured stellar spin axes are aligned with the normals to the planetary orbital planes (Fabrycky and Winn, 2009; Southworth, 2011). Yet for several systems (e.g. HAT-P-07, KELT-17, Kepler-63, WASP-08, WASP-33), there is a significant spin-orbit misalignment, which might be the outcome of a wide range of processes, such as early misalignment of the protoplanetary disk with respect to the stellar equator (Batygin, 2012; Crida and Batygin, 2014; Lai, 2014; Bate et al., 2010), pure dynamical interactions between the planets (Kaib et al., 2011; Batygin et al., 2011; Boué and Fabrycky, 2014a,b) or intrinsic stellar processes (Rogers et al., 2012, 2013).

1.1.2 Hot and warm Jupiters

The giant planet population, i.e., planets with $0.1 < M_\mathrm{p}/M_\mathrm{J} < 60$ and $R_\mathrm{p} > 0.5\,R_\mathrm{J}$, is typically sub-divided into period ranges, which are then related to a temperature adjective (cold, warm and hot). This temperature association comes from the expected equilibrium surface temperature of the planet, T, which is a function of stellarcentric distance, r, with a proportionality $T \propto r^{-1/2}$ or $T \propto P^{-1/3}$, in terms of the orbital period. A hot-Jupiter (HJ) is a giant planet with an orbital period $P < 10$ d, with an equilibrium surface temperature of about 1300 K. Following this reasoning, warm-Jupiters (WJs) are expected to have lower temperatures than HJs because their orbital periods are longer, $10 < P < 200$ days, and hence they are further away from their host star. The rest of the giant planet population is referred to as cold-Jupiters. HJs are uncommon. Their occurrence rate in FGK stars in the solar neighborhood is $\approx 1\%$ Wright et al. (2012), while in the *Kepler* data it is 0.5% (Howard et al., 2012).

Different studies using RVs and TTVs have found that HJs, in contrast to WJs, seem to lack close companions (Wright et al., 2009; Steffen and Agol, 2005; Latham et al., 2011; Steffen et al., 2012; Huang et al., 2016). A key word here is "close", which refers to smaller planets with similar orbital periods to either the WJs or HJs. The only known HJ with a close companion is WASP-47b (Becker et al., 2015), which is flanked by two mini-Neptunes. The most recent study to determine the frequency for which WJs and HJs have companions (Huang et al., 2016) investigated systems with planets that transit interior to the *Kepler* sample of gas giants with orbital periods within 0.5 and 200 days. A planet was deemed to be a gas giant if its radius was $8 < R_\mathrm{p}/R_\oplus < 20$. Huang et al. found that the companion fraction of WJ and HJ are mutually exclusive and confirmed that HJs typically do not have close inner companions. In

[10]The Rossiter-McLaughlin effect is the change to a rotationally broadened stellar spectral line due to the planet blocking different portions of the star at different times during the transit. The shape of the spectral lines provides information on the direction of the planet with respect to the rotation of the star.

comparison, half of the WJ have close companions. This led the authors to suggest that WJ and HJ are formed by two different mechanisms, in which the latter might represent in-situ formation. It must nonetheless be noted that planetary frequency does drop off rapidly within a few days, so other effects might be at play to shape the distributions. When companions at $5 < a < 20$ au are analyzed (Bryan et al., 2016), the fraction of outer companions of WJs with $1 < M_{\mathrm{p}}/M_{\mathrm{J}} < 20$ is lower than that of HJs. Both observations, low fraction of close companions and high fraction of distant companions, point to a disruptive formation or evolution mechanism for HJs.

Studies of the stellar host metallicity and giant planet occurrence have found that the detected giant planets often orbit metal-rich hosts (Gonzalez, 1997; Santos et al., 2004; Fischer and Valenti, 2005). The stellar metallicity is usually used as proxy for the metallicity of the protoplanetary disk, and therefore, the correlation between giant planets and stellar metallicity is interpreted as an indication that giant planets are formed in protoplanetary disks with a high solid-to-gas ratio. A correlation between stellar metallicity and orbital eccentricity has also been found. Dawson and Murray-Clay (2013) determined that giant planets around metal-rich stars have higher eccentricities than those around metal-poor stars. They suggest that metal-rich stars had protoplanetary disks that were rich in solid material and consequently formed more planets, which could have then engaged in planet-planet interactions.

In addition, the metallicity and planet occurrence rate do not correlate for all planet sizes and orbital periods (Petigura et al., 2018). Warm super-Earths ($10 < P < 100$ days and $1.0 < R_{\mathrm{p}}/R_{\oplus} < 1.7$) have a near-constant distribution over metallicities, from 0.4 to 2.5 times solar values. Warm sub-Neptunes, on the other hand, double their occurrence rate over the same metallicity range.[11] Metallicity seems to correlate with the occurrence rate of planets with $P < 10$ days and with planets that have sizes $R > 1.7\,R_{\oplus}$ (Petigura et al., 2018). The interpretation of these correlations remains unclear.

The orbital period distribution of short-period giant planets is still a matter of debate, particularly the existence and significance of the 3-day pileup. This feature was first observed in the RV data (Wright et al., 2009), but later found to be absent when taking into account the *Kepler* population (Howard et al., 2012). However, a recent study of the RV signal among *Kepler* giant planets, with false-positives removed from the sample, found that the occurrence rate of these planets in the orbital period range $1 < P < 400$ days decays by an other of magnitude, with the highest occurrence at 400 days (Santerne et al., 2016). This occurrence distribution has an important deficit between 10 to 40 d. This deficit could be interpreted as a pileup at about 4 days, which is a prediction of HJ formation through eccentricity excitation plus tidal circularization.

[11] Meaning that at a metallicity 2.5 solar the sub-Neptune occurrence rate is twice than that at 0.4 solar (see Fig. 10 of Petigura et al., 2018).

1.1.3 Systems with Tightly-packed Inner Planets (STIPs)

The Systems with Tightly-packed Inner Planets (STIPs) are the main focus of this thesis. These are multiplanet systems with short orbital periods, ranging from 1 to 100 days. The orbital period and multiplicity of these systems is not well constrained. The inner orbital period cutoff is real, while the outer one is still debatable and dependent on observational limits and challenges. Here, "tightly-packed" means that the planet period ratios are within 1 and 3 (Ford, 2014). These small spacings are likely to affect the stability of the systems (discussed in more detail in the next subsection). The minimum multiplicity for a system to be considered a STIP is not well-established and hence one needs to pick a working definition. We require that the multiplicity of a STIP be $N_\mathrm{p} \geq 3$, because their dynamical evolution is richer than a two-planet system, while their stability state cannot be predicted analytically. The formation and dynamics of STIPs are a challenge that increases in complexity with planet multiplicity.

The fraction of confirmed planetary systems that are STIPs based on the above definitions is about 5 to 6%. This fraction does not change significantly if the outer period cutoff is extended to larger periods, as it is dominated by shorter orbital periods. In literature, the period cutoff is at 100 days for STIPs, which will be used throughout this work to avoid confusion with other studies. We further require that there are at least three planets with orbital period shorter than 100 days. These two requirements select those systems that are difficult to reconcile with planet formation theories based on our Solar System (described in Sect. 1.2).

While STIPs are not limited to planets with a particular range of sizes and masses, the majority of planets in known STIPs are either super-Earths or mini-Neptunes, i.e., planets with masses within 1.0 to 10 $M_\oplus$. Hence, the composition of most of these planets is likely dominated by rock, ice and/or water, but not gas, even for low density planets. Moreover, formation mechanisms should be able to reproduce the mass-radius relationship and orbital distribution of STIPs.

As mentioned earlier, two main formation mechanisms for STIPs have been suggested: in-situ assembly/formation and planet migration. Planet migration is the favored theory but it has a few apparent inconsistencies. For example, we cannot reliably explain the direction or magnitude of planet migration (Goldreich and Tremaine, 1980; Lin and Papaloizou, 1986; Ward, 1997; Paardekooper and Mellema, 2006; Paardekooper et al., 2010, 2011), which depends on a large number of disk parameters. Neither can we explain why migration stops at particular distances (Ida and Lin, 2004a,b; Alibert et al., 2005; Masset et al., 2006). Furthermore, we cannot easily discern from observations whether the inner regions of disks have a different metallicity from their host star, e.g., due to the local enhancement of solids, which would directly impact the ability of a disk to form planets at short orbital periods. Planet migration might explain some STIPs and short-period giant planets, but not all. Alternative formation scenarios need to be explored, particularly those that address planetary diversity using a single framework.

1.1.4 Stability of extrasolar planets

Determining whether a planetary system is likely to be stable for long timescales is of broad interest, both for exoplanets and the Solar System. Several studies have looked into this problem, but so far there is not a straightforward answer.

A pair of planets in a two-planet system with initially circular-orbits will always be stable if they are separated by a dimensionless distance $\Delta > 2.4\,(\mu_0 + \mu_1)^{1/3}$ (Gladman, 1993), where μ_0 and μ_1 are the mass ratios of the inner and outer planet relative to the star, respectively. The second planet's semi-major axis is thus $a_1 = a_0(1 + \Delta)$, where a_0 is the semi-major axis of the inner planet. Planet separations can also be described in units of mutual Hill radii (Smith and Lissauer, 2009; Lissauer et al., 2014a; Marzari, 2014; Pu and Wu, 2015), where the mutual Hill radius $R_{\rm mH} = 0.5\,(a_0 + a_1)\,[(\mu_0 + \mu_1)/3]^{1/3}$. This gives $\eta \equiv (a_1 - a_0)/R_{\rm mH}$, for which two-planet stability requires $\eta \gtrsim 3.46$. For example, a two Jupiter-mass planet system around a solar-mass star must have planet separations of 3.5 $R_{\rm mH}$ or greater.

For higher multiplicities, there is no analytical separation limit. Usually, only the typical timescale for planets to become orbit crossing in a given system can be determined statistically (e.g., Obertas et al., 2017). This timescale depends on the initial η and the number of adjacent planets with that η (e.g. Chatterjee et al., 2008). For Earth-mass planets with $N_{\rm p} \gtrsim 3$, a mutual Hill radius separation of 10 allows long-term stability (Smith and Lissauer, 2009). Planet multiplicities (Table 1.1) and spacings are relevant to STIPs. Few STIPs have planets with $\eta < 10$, suggesting that the known planets should be stable over the lifetime of most stars (Lissauer et al., 2014a; Obertas et al., 2017). In a similar study, Pu and Wu (2015) found through N-body simulations that the dynamical instability spacing threshold for planetary systems with $N_{\rm p} \geq 4$ is 10 mutual Hill spacings for circular orbits and 12 for those with $e \simeq 0.02$. They compare their findings with the observed *Kepler* exoplanets' mutual Hill radii, and find that the typical separation is 12, consistent with the limit determined from simulations. However, secular interactions can lead to the disruption of a system, even if the planetary spacing alone suggests long-term metastability. A classic example is the evolution of Mercury in the Solar System, which has a small but non-negligible probability of being driven to orbit crossing with Venus on 5 Gyr timescales (Laskar, 1994).

Statistical stability studies of known STIP analogues with different multiplicity has shown that these systems are metastable, or prone to decay (Volk and Gladman, 2015), with equal fractions of systems going unstable in each decade of integration. This metastability implies that, over time, the multiplicity of an initially more populated system decreases as a result of instability and collisions. Pu and Wu (2015) reach a similar conclusion, and suggest that STIPs were more tightly-packed and evolved to their current configurations through instability. This might mean that *Kepler* planets formed in a more dissipative environment than the terrestrial planets in the Solar System.

Because many STIPs have high multiplicity, we must ask whether a large fraction of the systems with only two or three planets are decay products themselves.[12] There are also observability considerations; in particular, the presence of outer perturbers can affect the observed planet multiplicity of transiting systems, which can have a bearing on how we interpret planet-star misalignment (e.g. Winn et al., 2005; Kaib et al., 2011; Boué and Fabrycky, 2014a,b), at least in part.

1.1.5 Minimum Mass Solar Nebula (MMSN) vs. Minimum Mass Extrasolar Nebula (MMEN)

The determination of protoplanetary disk densities, compositions and profiles is of great importance to planet formation models. The Minimum Mass Solar Nebula (MMSN) is a disk model that was derived by spreading the masses of the planets into annuli centered on their current orbits and then augmenting those masses to restore the composition to solar values (Weidenschilling, 1977b; Hayashi, 1981). A commonly used version of this model is

$$\sigma_{\text{solids}} = 3.7 \times 10^2 \, \mathcal{F}_{\text{disk}} \, Z_{\text{rel}} \left(\frac{a}{0.2 \text{ au}} \right)^{-1.5} \text{g cm}^{-2},$$

where $\mathcal{F}_{\text{disk}}$ and Z_{rel} are the total disk mass and metallicity relative to the MMSN (Chiang and Youdin, 2010). This construction is usually used to establish order of magnitude calculations due to its intrinsic uncertainties, which neglect the possibility that planets did not form in their current locations.

With the discovery of exoplanets, this approach could be compared with other systems. Chiang and Laughlin (2013) estimated a Minimum Mass Extrasolar Nebula (MMEN), which is the solar-metallicity disk of gas and solids out of which the super-Earths uncovered by *Kepler* could have formed, if planet formation were 100% efficient and orbital migration were negligible. The authors employed 1925 planet candidates with radii $R < 5\, R_\oplus$ and $P < 100$ d from Batalha et al. (2013). In this model, each planet is assigned a surface density

$$\sigma_{\text{solids},i} \equiv \frac{M_i}{2\pi a_i \Delta a_i} = \frac{M_i}{2\pi a_i^2},$$

which is the surface density required to form the known planets in-situ. The mass-radius relationship $M_i = (R_i/R_\oplus)^{2.06} M_\oplus$ (Lissauer et al., 2011b) and $a_i = (P/\text{yr})^{2/3}$ were used to

[12]In planet building through planetesimal accumulation and then giant impacts, this is always true to some extent. Here we are referring specifically to otherwise fully built planetary systems that achieve instability in less than approximately 1 Gyr.

obtain the surface density of solids:

$$\sigma_{\text{solids}} = 6.2 \times 10^2 \, \mathcal{F}_{\text{disk}} \left(\frac{a}{0.2 \text{ au}} \right)^{-1.6} \text{g cm}^{-2},$$

with a corresponding gas surface density about 200 times higher:

$$\sigma_{\text{gas}} = 1.3 \times 10^5 \, \mathcal{F}_{\text{disk}} \left(\frac{a}{0.2 \text{ au}} \right)^{-1.6} \text{g cm}^{-2}.$$

These surface densities are related by $Z_{\text{solar}} \times Z_{\text{rel}} = 0.0049$, where Z_{rel} is the fraction of metals that could have condensed as solids in the hot inner disk ($Z_{\text{solar}} = 0.015$). We point out that the MMSN given here has been adapted from Chiang and Youdin (2010) to match the scaling of the MMEN.

Again, these surface densities have intrinsic uncertainties and therefore, their use is mainly to provide order of magnitude estimates for formation models. For example, using the MMEN, the typical coagulation times for close-in rocky planets can be as short as 10^4 to 10^7 yrs for $R_{\text{p}} = 1 - 5 \, R_{\oplus}$ within $a = 0.1 - 0.5$ au (see Eq. 14 from Chiang and Laughlin, 2013).

The MMEN depends strongly on the mass-radius relationship, the chosen planet sample and the temperature profile. It does not account for different compositions throughout the disk or possible density profile changes. Nonetheless, we will use the MMEN in Chap. 3 as a baseline for gas surface densities.

1.2 Planet formation

A number of formation mechanisms have been proposed and developed to explain the origin of both rocky planets and gas/ice giants. While there are many parts of the planet formation process that are believed to be understood, there are also many outstanding questions, particularly regarding planetesimal formation. In the case of giant planet formation, there are two main accepted ideas: the core accretion model and gravitational instability. In this section, we will only briefly describe the formation of rocky planets and the core accretion model for forming giant planets. Giant planet formation by disk instability is thought to be most relevant for wide (50-100 au) orbit planets (Boley, 2009). Because we are principally concerned with STIPs and planets on moderate orbits, we do not discuss this mechanism further and refer the reader to Helled et al. (2014) for a review.

1.2.1 Formation of rocky planets

Briefly, the formation of a rocky planet starts with the settling of interstellar dust particles and disk condensates to the mid-plane of the protostellar (or circumstellar) disk, collisionally growing from micron to planetary scales (13 order of magnitude in size) (Armitage, 2007). Radiogenic dating of the Solar System materials and observations of protoplanetary disks around stars of different ages constrain the bulk of planet formation to occur in a few Myr (Wadhwa et al., 2007), followed by additional evolution over 10^7 to 10^8 yr. Select stages of planetary growth and potentially dominant processes during that stage are highlighted in Table 1.2.

Stage of growth	Physical process	Diameter range (m)	Time scale (yr)
Dust to pebbles	Settling and radial migration	$10^{-6} - 10^{-2}$	10^3?
Pebbles to rocks	Uncertain mechanism	$10^{-2} - 10^3$	$10^3 - 10^6$?
Pebbles to rocks and planetesimals	Pairwise collisional growth	$10^2 - 10^4$	
Large planetesimals	Runaway growth ($\sigma_v \lesssim v_{\rm esc}$)	$10^4 - 10^5$	$10^3 - 10^4$
Large planetesimals to planet embryos	Oligarchic growth ($\sigma_v \gtrsim v_{\rm esc}$)	$10^5 - 10^6$	10^5
Planet embryos to terrestrial planets	Chaotic growth	$10^6 - 10^7$	$10^6 - 10^8$

Table 1.2: Summary of the growth sequence to form rocky planets starting from dust particles. The physical processes and typical growth timescales are also included. The question marks indicate timescales that are not well defined. Adapted from Perryman (2011).

First, we introduce two important physical phenomena affecting the interactions of solid objects with the gas and other particles: aerodynamical drag and gravitational focusing. Each acts on different size/mass regimes. Aerodynamic drag (gas drag) is due to the relative velocity of a solid body moving through gas. The gas in a protoplanetary disk has partial radial support throughout most of the disk due to an outward pressure gradient. This causes the gas to typically orbit more slowly than is necessary for solids, the latter of which do not directly feel the same pressure gradient. The drag force is given by

$$\mathbf{F}_{\rm D} = -\frac{1}{2} C_{\rm D} (\pi s^2) \rho v \mathbf{v},$$

where ρ is the gas density, and s and $\mathbf{v}$ are the particle's radius and velocity relative to the gas, respectively. The drag coefficient, $C_{\rm D}$, depends on the gas mean free path[13] λ, the particle's shape (usually assumed to be spherical) and its size s (see Armitage, 2007, for more details). Depending on the local disk conditions, solids with sizes around the millimeter to decameter scales can experience rapid inward radial drift. For example, bodies with $R \simeq 1$ m migrate from 1 au all the way to the star in about 100 yr, for a MMSN. Gas drag places an apparent barrier to the growth beyond 1 meter scales (or smaller) due to the expected inward migration timescales, commonly known as the "meter-barrier" (Weidenschilling, 1977a).

[13]For a MMSN, $\lambda \sim 0.01$ m (Perryman, 2011).

While gas drag seemingly frustrates the growth of planetesimals, once formed, the collision cross-section of an object can be enhanced by its gravity. The effective cross sectional radius, b, is given by

$$b = R\left(1 + \frac{v_{\rm esc}^2}{\sigma_v^2}\right) = R\,\mathcal{F}_{\rm g}.$$

Here $v_{\rm esc} = \sqrt{2GM\,R^{-1}}$ is the escape velocity of the massive object with mass M, and radius R, and σ_v is the velocity dispersion between objects. $\mathcal{F}_{\rm g}$ is known as the gravitational focusing factor and it is important for objects with $R \gtrsim 10$ km.[14] A massive body, such as a planetary embryo, that is immersed in a swarm of planetesimals with surface density $\Sigma_{\rm p}$ will have a mass growth rate given by

$$\dot{M} = \frac{{\rm d}M}{{\rm d}t} = \frac{1}{2}\Sigma_{\rm p}\,\Omega_{\rm p}\,\pi R^2\mathcal{F}_{\rm g},$$

where $\Omega_{\rm p}$ is the orbital frequency (Armitage, 2007). The growth of an embryo is then a function of $v_{\rm esc}/\sigma_v$; if the planetesimals have a smaller velocity dispersion than the embryo's escape velocity, then $\dot{M} \propto R^4$ and the embryo grows fast, or "runs away". On the contrary, if $v_{\rm esc} < \sigma_v$ then $\mathcal{F}_{\rm g} \to 1$ and $\dot{M} \propto R^2$. This means that the embryo would grow at a slower pace than in the runaway stage but still faster than smaller objects. The latter is known as "oligarchic growth" because it gives opportunity to less massive planets to catch up.

As Table 1.2 indicates, the dust condenses from the protostellar disk as it cools down, followed by growth while it rapidly settles to the mid-plane of the disk. Once in the mid-plane, the particles drift inward due to gas drag until they reach a terminal velocity and in the meantime, grow through electrostatic and mechanical sticking. When the silicate dust grains reach a millimeter in size, the collisions do not continue to form aggregates because they bounce off each other. This is known as the "bouncing barrier" (Zsom and Dullemond, 2008; Güttler et al., 2009). The growth mechanism from cm-sized particles to full planetesimals is unknown, due to a combination of radial drift and particle bouncing. Different processes have been suggested to explain the rapid growth to planetesimal scales; we refer the reader to Armitage (2007).

Once objects reach sizes around 1 km, the planetesimals become decoupled from the gas on short timescales, allowing the dominant growth mechanism to be pairwise collisions. Initially, the presence of the gas keeps the velocity dispersion of the planetesimals low, and therefore those with a bigger size run away. When the bigger aggregates of planetesimals are about 100 km, they stir up the orbits of the smaller objects and the velocity dispersion increases, reducing the gravitational focusing and entering the oligarchic growth phase.

The growth of a planet embryo is limited by the availability of planetesimals at a disk distance

[14] This threshold depends on the assumed σ_v, which roughly scales as the product of the eccentricity, e and the circular velocity, v_c, of the planetesimals at a given stellarcentric distance, such that: $\sigma_v \sim e\,v_c \propto e\,r^{-1/2}$, implying that at larger stellarcentric distances the gravitational focusing becomes important for smaller objects than closer to the star.

r, within an annulus $2\Delta r$. The maximum mass of an embryo, or isolation mass, is then

$$\begin{aligned} M_{\rm iso} &= 4\pi\, r \Delta r\, \sigma_\rho(r) = 16\pi\, r^2 \left(\frac{M_{\rm iso}}{3M_*}\right)^{1/3} \sigma_\rho(r), \\ &= \sqrt{\frac{\left[16\pi\, r^2\, \sigma_\rho(r)\right]^3}{3\, M_*}}, \end{aligned} \tag{1.1}$$

where M_* is the stellar mass, and $\sigma_\rho(r)$ is the surface density of solids at r. These isolated embryos can still affect the orbits of the neighboring planetesimals and other embryos, particularly if the mass of the embryo is comparable to the total mass of planetesimal disk. The cumulative effect is a chaotic environment that could lead to collisions and merging of the embryos or to protracted accretion of planetesimals. The final assembly of rocky planets continues with the embryo mergers, until the orbital spacing results in a quasi-stable configuration, which takes a few Myr to potentially over 100 Myr under standard planet formation models (Chambers and Wetherill, 1998; Goldreich et al., 2004; Moorhead and Adams, 2005; Kokubo et al., 2006; Kenyon and Bromley, 2006).

1.2.2 Giant planets: core accretion plus gas capture model

The core accretion model, also known as "core nucleated instability", posits that giant planets form in three distinct stages. First, there is an initial core formation of rocky planets, as described above. Second there is a protracted period of slow gas and planetesimal growth, which transitions to a runaway gas capture phase when a critical mass threshold is reached.

A rocky planet core keeps accreting both disk solids and gas as available within its gravitational reach. When there are no more solids in the vicinity, the planet opens a gap in the solid surface distribution, but not necessarily in the gaseous disk. The planet steadily accretes gas, but the capture onto an envelope depends on the cooling and contraction of the accreted gas as much as the planetary mass. Under the right conditions, the planetary mass keeps increasing until it reaches a critical mass at which gas runaway accretion starts. The critical mass definition depends of the time dependence of the model used. In static models, where there is a steady accretion of planetesimals, the critical core mass is that above which the gaseous envelope cannot support hydrostatic equilibrium (Mizuno, 1980; Stevenson, 1982; Rafikov, 2006, 2011). On the other hand, if the model is time-dependent, a critical core mass is defined when the envelope grows superlinearly. This occurs when the self-gravity of the envelope becomes significant, i.e., when the envelope has as much mass as the core, and the thermal disequilibrium increases (runaway cooling, Pollack et al., 1996; Ikoma et al., 2000). The growth stops either when a gap is opened in the gaseous disk or when the disk dissipates, starting the isolation stage of growth.

The core accretion model is thought to be more efficient in regions of the disk with a higher local solid-to-gas ratio, particularly beyond the ice line. The temperature gradient within a disk is $\propto (r/1\mathrm{au})^{-p}$, where p is a positive exponent, and therefore, the temperature decays with stellarcentric distance, eventually allowing additional solids to condense from the gas.

In principle, if rocky planets are formed efficiently and fast within the lifetime of the gaseous disk, regardless of their stellarcentric distance, it facilitates the subsequent gas acquisition. This opens the door to the possibility of in-situ formation of gas giant planets. Simplistically, the amount of gas accreted onto a planet depends on: (1) availability of gas in the disk; (2) the gravitational well of the planet; and (3) cooling rate of the planet to hold the envelope. The availability of gas is related to the disk lifetime and gap opening, while the gravitational well depends on the mass of the planet. The cooling rate depends on the heat transport of the envelope, which can be affected by dust. We then could ask: can rocky planets form efficiently in the innermost region of the disk before the gas disperses? If so, can they reach a critical mass to start runaway gas accretion? Is orbital planetary metastability present when the gas is around? How many rocky planets can be formed?

1.3 This thesis

Throughout this work we seek to answer two main questions. Firstly, assuming that rocky planets form efficiently in the inner region of the disk before the gas disperses, is metastability present when the gas is still around? If so, can critical cores form from this initial instability? Secondly, what dynamical effects originate from the presence of a planetary perturber outside known STIPs?. This thesis is divided into six additional chapters. In Chap. 2, we provide an overview of the methodology used in the following two chapters, including a description of the numerical methods, i.e., N-body integrators and secular code. The experimental development and analysis of the two main science questions are developed in Chap. 3 and Chap. 4. In Chap. 3, we evaluate whether critical cores can be formed through the metastability of primordial high-multiplicity STIPs in a gas-free and gas-rich environment; while, in Chap. 4, we determine dynamical effects that an outer planetary perturber has on STIPs, and how they affect the stability and observability of the inner system. We discuss the results of the numerical simulations and analysis in Chap. 5, including limitations of each experiment with possible ways to improvement as future work, as well as the importance and implications of the results. In Chap. 6, we summarize the main take away points of each experiment. Finally, a list of complementary and improved experiments as possible future work is provided in Chap. 7.

Chapter 2

Methodology overview

We designed a series of N-body simulations: 1) to explore the in-situ formation scenario of hot-Jupiters (HJs), in which giant planet formation is envisaged to be the outcome of planet-planet scattering followed by collisions and consolidation; and 2) to investigate the effects of the long-term gravitational perturbations, i.e., secular effects, of an outer giant planet on known STIPs. In both studies, numerical experiments are carried out using a large number of planetary system realizations that have initial conditions based on STIP prototypes with a planet multiplicity $N_{\mathrm{p}} \geq 6$.

As part of these studies, we evaluate system stability for any given STIP prototype by perturbing the initial conditions for each realization, keeping initial planetary masses and semi-major axes fixed. The specifics of the initial conditions will be described in Sect. 3.1. The first experiment is divided into two stages, each with increasing dynamical complexity. Initially, planet-disk interactions are ignored so that we can estimate the fraction of systems in which at least one planet with $M_{\mathrm{p}} \geq 10\,M_{\oplus}$ forms through consolidation. We then include a gaseous tidal damping prescription in the N-body integrator to account for planet-disk interactions, as described in Sect. 2.1.1. We run the realizations without planet-disk interactions with `Mercury6`, while 15th-order Integrator with Adaptive Time-Stepping (`IAS15`) is employed whenever the gaseous tidal damping is used, on account of the non-conservative forces. I should emphasize that the `IAS15` code is my personal implementation, in C language, of the algorithm developed by Rein and Spiegel (2015), which will be described in Sect. 2.1.4.

It is uncertain whether the known STIPs have any outer companions. Should such companions exist, they could affect the dynamics of STIPs through gravitational perturbations. To explore this situation, we run N-body simulations of known STIPs, but include a Jupiter-like perturber. We use Kepler-11 (K11) and Kepler-90 (K90) as prototypes (see Sect. 4.1). The perturber's distance to the host star is varied from 5.2 au to 1 au to explore a range of secular dynamics. For certain system configurations, we calculate the theoretical secular precession eigenfrequencies and determine whether there is strong inclination or eccentricity forcing. In addition, we obtain the synthetic secular precession frequencies and compare them to the theory. Discrepancies between the theoretical and synthetic spectra can reveal strong gravitational interactions, such as mean motion resonances or non-linear secular resonances.

2.1 Numerical simulations

In this section, we describe the main integration codes and algorithms used in this work: `Mercury6` (Chambers, 1999) and `IAS15` (Rein and Spiegel, 2015). The physical forces included in the simulations, along with explanations regarding their relevance, are discussed in Sect. 2.1.1. The handling of close encounters and collisions is detailed in Sect. 2.1.2, which is crucial to addressing planetary consolidation. Sect. 2.1.3 provides an overview of `Mercury6`'s hybrid-symplectic integration algorithm, and finally, Sect. 2.1.4 details the `IAS15` integrator, comparing my implementation to that of Rein and Spiegel (2015).

2.1.1 Beyond Newtonian Gravity: additional forces

The effects of general relativity (GR) become important for planets with short orbital periods, as it changes the precession of the planet's longitude of pericenter, ϖ. In all simulations, we include a correction for GR as defined by (Nobili and Roxburgh, 1986), which is modeled as a dipole-like potential and only depends on the position of the body, i.e.,

$$\mathbf{a}_{\mathrm{GR}} = -\frac{6\,G^2 M^2}{c^2 r^4}\,\mathbf{r}. \tag{2.1}$$

With this approximation, GR can be modeled in both `Mercury6` and `IAS15`. Some simulations also include gaseous tidal damping, i.e., damping due to the gravitational interaction between the planet and the spiral waves launched by the planet. This interaction is prescribed here as:

$$\begin{aligned} \mathbf{a}_{\mathrm{TD}} &= -\frac{1}{\tau_e}\frac{(\mathbf{v}\cdot\boldsymbol{\rho})}{\|\boldsymbol{\rho}\|^2}\boldsymbol{\rho} - \frac{(\mathbf{v}\cdot\hat{\mathbf{k}})}{\tau_i}\hat{\mathbf{k}} \\ &= -\frac{v_\rho}{\tau_e}\hat{\boldsymbol{\rho}} - \frac{v_z}{\tau_i}\hat{\mathbf{k}}. \end{aligned} \tag{2.2}$$

Here, we use cylindrical coordinates (as shown in Fig. 2.1), where $\boldsymbol{\rho} = x\,\hat{\mathbf{i}} + y\,\hat{\mathbf{j}}$, and v_ρ and v_z are the magnitude of the radial and vertical components of the velocity. This prescription successfully damps the eccentricity and inclination of planets in a way that is in overall agreement with the results of Cresswell et al. (2007). Furthermore, this damping is similar to that used by Papaloizou and Larwood (2000), but different by a factor of 2. This difference is ultimately absorbed by the eccentricity and inclination damping timescales τ_e and τ_i, respectively. These timescales control the magnitude of the damping acceleration, as shown in Eq. 2.2, and are given by

$$\frac{1}{\tau_e} = \frac{K_e}{K_e\tau_{\mathrm{wave}} + \left|\frac{v_\rho}{v_c}\right|^3} \qquad \text{and} \qquad \frac{1}{\tau_i} = \frac{K_i}{K_i\tau_{\mathrm{wave}} + \left|\frac{v_z}{v_c}\right|^3}. \tag{2.3}$$

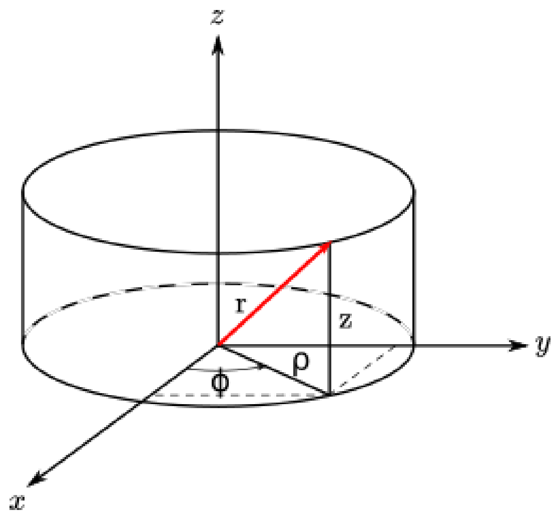

Figure 2.1: Notation used in cylindrical coordinates.

where $v_{\rm c} = \sqrt{G\,M_*/\rho}$ is the circular velocity at ρ. Both timescales are related to the characteristic wave time, $\tau_{\rm wave}$, which is determined through tidal torque theory of planet-disk interactions in isothermal disks (see Tanaka and Ward, 2004, Eq. 49). This wave time describes the mean timescale for the orbital elements of a planet to evolve due to the forcing by density waves within a gaseous disk; namely

$$\tau_{\rm wave} = \left(\frac{M_{\rm p}}{M_*}\right)^{-1} \left(\frac{\sigma_{\rm p}\,a^2}{M_*}\right)^{-1} \left(\frac{c_{\rm s}}{a\,\Omega_{\rm p}}\right)^{4} \Omega_{\rm p}^{-1}, \tag{2.4}$$

where $M_{\rm p}$ and M_* are the masses of the planet and star, respectively. The wave time also depends on the planet's semi-major axis, a, and mean motion, $\Omega_{\rm p}^2 = GM_* a^{-3}$, often presented as n in astrodynamics. The disk properties are included in the surface density, $\sigma_{\rm p}(\rho)$, and the isothermal sound speed at radius ρ, i.e.,

$$c_{\rm s}(\rho) = \sqrt{\frac{\mathcal{R}T}{\mu}}$$

with molecular weight of the gas $\mu = 2.3$ (in g/mol), which corresponds to the value for the interstellar gas that was thought to lead to the formation of the Solar System. In `IAS15`, $K_e t_{\rm wave} = 0.00253$ and $K_i t_{\rm wave} = 0.00075$ are treated as constants (Cresswell et al., 2007). Consequently, as $\tau_{\rm wave}$ changes according to the local disk conditions, the values of K_e and K_i also change.

In practice, we do not use $\tau_{\rm wave}$ directly. In `IAS15`, we introduce the timescale $\tau_{\rm local}$, which is in part a scaled version of Eq. 2.4, at 1 au. This reduces the number of calculations in the code and allows us to include the vertical distribution of gas in the disk and the density decay with time. The timescale $\tau_{\rm local}$ depends on the local disk conditions and the planet's position and mass in a similar way to Eq. 2.4. We account for the vertical distribution of the gas, z, on the torque by assuming a Gaussian profile for the density, with scale height $H = c_\mathrm{s}/\Omega_\mathrm{p}$. We also assume that the disk density decays exponentially with time using a characteristic timescale λ, such that

$$\tau_\mathrm{local}(\rho, z, \lambda, M_\mathrm{p}; t) = \tau_o^{1\mathrm{au}} \left(\frac{M_\mathrm{p}}{M_*}\right)^{-1} \left(\frac{\rho}{1au}\right)^{q-2p+3/2} \mathrm{e}^{z^2/2H^2}\, \mathrm{e}^{t/\lambda}, \tag{2.5}$$

where p and q are given by the chosen thermal and surface density profiles, respectively. The factor $\tau_o^{1\mathrm{au}}$ is a scaled wave time at $\rho = 1$ au, given by

$$\begin{aligned}
\tau_o^{1\mathrm{au}} &\equiv \left(\frac{\sigma_o\,\rho_o^2}{M_*}\right)^{-1} \left(\frac{\mathcal{R}\,T_o\,\rho_o}{\mu\,G\,M_*}\right)^{2} \left(\frac{G\,M_*}{\rho_o^3}\right)^{-1/2}\Bigg|_{\rho_o=1\mathrm{au}} \\
\tau_o^{1\mathrm{au}} &= \left(\frac{\rho_o^3}{G^5\,M_*^3}\right)^{1/2} \left(\frac{\mathcal{R}\,T_o}{\mu}\right)^{2} \sigma_o^{-1}\Bigg|_{\rho_o=1\mathrm{au}} \\
\tau_o^{1\mathrm{au}} &\approx 0.078 \text{ days.}
\end{aligned} \tag{2.6}$$

To obtain the numerical value, we assume $M_* = 1\,M_\odot$, $\rho = 1$ au, $\sigma_o = 9.899 \times 10^3$ g cm^{-2} and $T_o = 300$ K. For reference, at $t = 0$ the local damping timescale of an Earth mass planet located at 1 au and in the disk mid-plane ($z = 0$) is $\tau_\mathrm{local} \approx 71$ yr. The gaseous surface density profile, from which σ_o proceeds, is the MMEN (Chiang and Laughlin, 2013)

$$\sigma_\mathrm{p} = \sigma^\mathrm{MMEN}(\rho) = \sigma_o \left(\frac{\rho}{1 \text{ au}}\right)^{-q}, \tag{2.7}$$

where $q = 1.6$ and σ_o is a scaled surface density at 1 au with value $\sigma_\mathrm{g} = 9.899 \times 10^3$ g cm^{-2} for the gas or $\sigma_\mathrm{s} = 47.21$ g cm^{-2} for the solids. The thermal profile is set according to

$$T(\rho) = 300 \left(\frac{\rho}{1 \text{ au}}\right)^{-p} \mathrm{K}$$

with $p = 0.6$.

The use of τ_local provides a convenient way of setting the damping timescale (through τ_o) for experiment design. The convenience of Eqs. 2.5 and 2.6 is that they can be easily adapted for different assumptions of disk density and temperature profiles.

2.1.2 Close encounters and collisions

In most N-body integrators, the interacting bodies are taken as point masses as long as there are no close encounters or collisions. Close encounters occur whenever two bodies are within a threshold distance of each other. A collision, in it simplest form, occurs when the distance between two bodies is smaller than the sum of their "physical" radii ($r_{ij} \leq R_i + R_j$), a strategy that we also adopt for this work. Commonly, in simulations of planetary systems the close encounter threshold is set to be an integer multiple of the planets' mutual Hill radius

$$R_{\rm mH} = \frac{a_i + a_j}{2} \left(\frac{m_i + m_j}{3\,M_*} \right)^{1/3}, \tag{2.8}$$

where a is the semi-major axis, and m and M_* are the planetary and stellar masses, respectively. In practice, the multiple of $R_{\rm mH}$ ranges between 1 and 3 and is a trade-off between resolving the encounter properly and minimizing computational time, particularly for the hybrid-integrator in `Mercury6`. In `IAS15`, a close encounter is flagged whenever the distance between two bodies is $r_{ij} \leq 3\,R_{\rm mH}$,[15] which is evaluated at each substep.

The planetary size is indispensable in determining whether a collision has occurred within a simulation. `Mercury6` and `IAS15` calculate the size of the planets with the provided bulk density and mass. For most planets discovered by the transit method, only the size is known. On the other hand, for planets detected by the RV method, only the product of the mass times sin I is known. About 300 planets have independent measurements of both radius and mass (Chen and Kipping, 2017). As a consequence, the bulk density of the majority of planets is unknown. For planets with unknown masses or radii, several power-law mass-radius relationships have been suggested, such as

$$R_{\rm p} = R_\oplus \left(\frac{M_{\rm p}}{M_\oplus} \right)^{\nu}, \tag{2.9}$$

where ν takes different values according to the data used to fit the function (Valencia et al., 2006; Lissauer et al., 2011b; Wolfgang et al., 2016; Chen and Kipping, 2017). The database `exoplanets.org` takes the value $\nu = 0.485$ (Lissauer et al., 2011b), using a fit to the masses and radii of the planets in the Solar System from Earth to Saturn. Alternatively, Valencia et al. (2006) who included interior models of Earth-like planets with different compositions and mantle-core ratios, derived $\nu = 0.267 - 0.272$ for masses $1 < M_{\rm p}/M_\oplus < 10$.

It is often desirable to infer the bulk density of a planet, which can also be estimated from the mass-radius relationship:

$$\rho = \rho_\oplus \left(\frac{M}{M_\oplus} \right)^{1-3\nu}, \tag{2.10}$$

$$\rho = \rho_\oplus \left(3.33 \times 10^5\right)^{1-3\nu} \left(\frac{M}{M_\odot} \right)^{1-3\nu}. \tag{2.11}$$

Each expression is scaled either to the Earth's (Eq. 2.10) or the Sun's mass (Eq. 2.11), and $\rho_\oplus = 5514$ kg m^{-3} is Earth's bulk density.

[15] As discussed in Sect. 1.1.4, two planets need to be separated by a mutual Hill radii of $\eta \gtrsim 3.46$ to be stable (Gladman, 1993). Therefore, tagging a close encounter with smaller separation increases the probability of identifying a pair of planets that might be involved in a collision later in the simulation. By choosing the tagging distance at $3\,R_{\rm mH}$, we are being conservative in the early identification of close encounters.

Collisions in both codes are assumed to be inelastic. The new mass is determined as the sum of the colliding bodies, which is then used to determine the bulk density using Eq. 2.11. The new body's radius is then calculated from the mass and density. The position and velocity vectors of the consolidated body are then estimated from the center of mass of the parent bodies. Each time that a collision occurs, the size of the body array[16] remains the same but the order of the elements is changed. The lost planet is moved to the end of the array and assigned a zero mass, while the other planets are shifted accordingly one place lower in the array. As a final step, the total number of bodies is reduced by one, which shortens the loop for evaluating the number of planets, reducing the integration time. Other possible dynamical outcomes, besides collisions, are the loss of planets due to scattering outside the system or due to collisions with the star. In these two cases, the total number of interacting masses is reduced each time, as well as the total mass available for planet consolidation. When a planet is lost into the star, the center of mass is affected by the redistribution of mass. On the other hand, if a planet reaches a threshold distance from the star that is considered unbound to the planetary system, the code stops following the orbit.

2.1.3 Mercury6

`Mercury6` (Chambers, 1999) is primarily used to run the simulations that explore the feasibility of critical core consolidation in the absence of planet-disk interactions. `Mercury6` possesses five integration algorithms: a second-order mixed-variable symplectic (MVS) integrator (Wisdom and Holman, 1991; Wisdom et al., 1996); a general Bulirsch-Stoer (BS) (Stoer and Bulirsch, 1980; Press et al., 1992a); a conservative BS; a non-symplectic fifteenth-order integrator with Gauss-Radau spacings (RADAU, Everhart, 1985); and a hybrid symplectic/BS integrator (Chambers, 1999). From the five different integrators within `Mercury6`, the hybrid integrator was utilized due to its ability to accurately evolve systems for protracted periods of time and capture close encounters.

The hybrid integrator uses mixed-center variables conformed by heliocentric positions and barycentric velocities (mixed-variable symplectic, MVS) for most of the evolution, but it changes from the MVS to the BS integrator to resolve/integrate close encounters. Should close encounters not occur, then the system is integrated solely with the MVS algorithm.

A symplectic algorithm conserves the phase-space (q, p)[17], and is a numerical method for solving Hamilton's equations

$$\dot{p} = -\frac{\partial \mathcal{H}}{\partial q} \qquad \text{and} \qquad \dot{q} = \frac{\partial \mathcal{H}}{\partial p}, \tag{2.12}$$

where $\mathcal{H}(p, q) = T(p) + V(q)$ is the Hamiltonian, and q and p are the canonical position and

[16]This means that within the code, in C language, the bodies are defined in an array or vector, where each body is identified with an index.

[17]Not to be confused with the power-law indices q and p given above

momentum coordinates, respectively. The total variation with time of a quantity $z = z(q_i, p_i, t)$ for a system of N particles is

$$\begin{aligned}
\frac{\mathrm{d}z}{\mathrm{d}t} &= \sum_{i=1}^{N} \left(\frac{\partial z}{\partial q_i}\frac{\mathrm{d}q_i}{\mathrm{d}t} + \frac{\partial z}{\partial p_i}\frac{\mathrm{d}p_i}{\mathrm{d}t} \right) \\
&= \sum_{i=1}^{N} \left(\frac{\partial z}{\partial q_i}\frac{\partial \mathcal{H}}{\partial p_i} - \frac{\partial z}{\partial p_i}\frac{\partial \mathcal{H}}{\partial q_i} \right) \\
&= Fz,
\end{aligned}$$

where F is an operator defined as

$$F \equiv \sum_{i=1}^{N} \left(\frac{\partial \mathcal{H}}{\partial p_i}\frac{\partial}{\partial q_i} - \frac{\partial \mathcal{H}}{\partial q_i}\frac{\partial}{\partial p_i} \right). \tag{2.13}$$

The general solution of Hamilton's equations (Eqs. 2.12) is given by the integration of

$$\int_{z(t-\tau)}^{z(t)} \frac{\mathrm{d}z}{z} = \int_{t-\tau}^{t} F\mathrm{d}t \qquad \Rightarrow \qquad z(t) = \mathrm{e}^{\tau F}\, z(t-\tau), \tag{2.14}$$

where $z(t)$ is either the canonical position or momentum at time t and τ is the timestep.

In practice, it is common to divide the Hamiltonian into two or more components that can be solved analytically in the form of $\mathcal{H} = \mathcal{H}_A + \mathcal{H}_B + \cdots$, where $\mathcal{H}_B$ is a perturbation to $\mathcal{H}_A$. When the Hamiltonian is separable, the respective operator is the sum $F = A + B$ and the solution changes to

$$z(t) = \mathrm{e}^{\tau(A+B)}\, z(t-\tau), \tag{2.15}$$

$$= \mathrm{e}^{\tau A}\mathrm{e}^{\tau B}\, z(t-\tau). \tag{2.16}$$

Numerically, the exponential in Eqs. 2.14 and 2.16 are expanded in Taylor series of τ:

$$\mathrm{e}^{\tau F} = 1 + \tau F + \frac{\tau^2 F^2}{2} + \cdots. \tag{2.17}$$

This approximation is exact to first or second-order depending on the expansion of $\mathrm{e}^{\tau(A+B)}$. Applying each operator sequentially gives a first-order integrator (Eq. 2.16). The integrator can be made second-order by splitting the B operator into a half time-step and applying it before and after the A operator (Eq. 2.18). Because the B operator represents a perturbation, this can be viewed as a form of a kick-drift-kick leapfrog algorithm,[18]

$$z(t) = \mathrm{e}^{\tau B/2}\mathrm{e}^{\tau A}\mathrm{e}^{\tau B/2}\, z(t-\tau). \tag{2.18}$$

The expanded exponential in Eq. 2.15 is the same to first-order in Eq. 2.16 and to second-order in Eq. 2.18. To be explicit,

$$\begin{aligned}
\mathrm{e}^{\tau(A+B)} &= 1 + \tau\,(A+B) + \frac{\tau^2}{2}\,(A+B)^2 + \cdots \\
\mathrm{e}^{\tau A}\mathrm{e}^{\tau B} &= 1 + \tau\,(A+B) + \frac{\tau^2}{2}\,(A^2+2AB+B^2) + \cdots \\
\mathrm{e}^{\tau B/2}\mathrm{e}^{\tau A}\mathrm{e}^{\tau B/2} &= 1 + \tau\,(A+B) + \frac{\tau^2}{2}\,(A+B)^2 + \\
&\qquad \frac{\tau^3}{4}\,[(A+B)(A^2+2AB+B^2) + (B^2+BA-A^2)A] + \cdots
\end{aligned}$$

Recall that the operators A and B are not assumed to commute, i.e., $AB \neq BA$ and that $A^2+AB+BA+B^2 \neq A^2+2AB+B^2$.

For a second-order integrator, the error between $\mathrm{e}^{\tau(A+B)}$ and $\mathrm{e}^{\tau B/2}\mathrm{e}^{\tau A}\mathrm{e}^{\tau B/2}$ is $\mathcal{O}(\tau^3)$. If τ is small, then the difference between the analytic and numerical solutions is also small. The energy error does not build up because the method is symplectic.

The Hamiltonian in the MVS integrator (Chambers, 1999) for an N-body system is $\mathcal{H} = \mathcal{H}_0 + \mathcal{H}_1 + \mathcal{H}_2$, where

$$\mathcal{H}_0 = \sum_{i=0}^{N}\left(\frac{p_i^2}{2m_i} - \frac{Gm_i m_*}{r_{i*}}\right) - G\sum_{i=1}^{N}\sum_{j=i+1}^{N}\frac{m_i m_j}{r_{ij}}\left[1-K(r_{ij})\right], \tag{2.19}$$

$$\mathcal{H}_1 = -G\sum_{i=1}^{N}\sum_{j=i+1}^{N}\frac{m_i m_j}{r_{ij}}K(r_{ij}), \tag{2.20}$$

$$\mathcal{H}_2 = \frac{1}{2m_*}\left(\sum_{i=1}^{N}\vec{p}_i\right)^2. \tag{2.21}$$

Here, $\mathcal{H}_0$ is the unperturbed motion of the secondary bodies around the primary (e.g., planets

[18] This means that the velocity, v_i, and position, x_i, are updated from the time t_i to t_{i+1} by a "leapfrog" method. This involves giving a kick with half timestep to the velocity, drifting the position with this kick by a full step, and then using this drift to update the second derivative of x, i.e., a_i, to a_{i+1}, to finally update the velocity to v_{i+1} using a second half timestep kick. This scheme is thus written as:

$$\begin{aligned}
v_{i+1/2} &= v_i + a_i\,\frac{\Delta t}{2} && \text{(kick)}, \\
x_{i+1} &= x_i + v_{i+1/2}\,\Delta t && \text{(drift)}, \\
v_{i+1} &= v_{i+1/2} + a_{i+1}\,\frac{\Delta t}{2} && \text{(kick)},
\end{aligned}$$

where the subindex $i+1/2$ indicates a half timestep variation.

around a star) if there are no close encounters. Perturbations due planet-planet interactions are given by $\mathcal{H}_1$. Finally, because barycentric velocities are used, an additional Hamiltonian, $\mathcal{H}_2$, is needed to account for the kinetic energy due to the star. In `Mercury6`, $\mathcal{H}_1$ and $\mathcal{H}_2$, are always less than $\mathcal{H}_0$ due to the dependence of $\mathcal{H}_0$ and $\mathcal{H}_1$ on $K(r_{ij})$:

$$K(r_{ij}) = \begin{cases} 0 & y < 0 \\ \frac{y^2}{2y^2-2y+1} & 0 < y < 1 \\ 1 & y > 1 \end{cases} \tag{2.22}$$

and

$$y = \left(\frac{r_{ij} - 0.1\, r_{\rm crit}}{0.9\, r_{\rm crit}}\right), \tag{2.23}$$

which accounts for possible close encounters (see Chambers, 1999, for more details). The third term in $\mathcal{H}_0$ (Eq. 2.19) equals zero if $r_{ij} > r_{\rm crit}$[19]. When $r_{ij} \leq 0.1\, r_{\rm crit}$, $\mathcal{H}_1 \to 0$ and the mutual planetary interaction is included in $\mathcal{H}_0$. At the same time, the integrator changes to the BS so that it can resolve the close encounter and a possible collision.

The second-order integrator for the MVS is

$$z(t) = \mathrm{e}^{\tau B/2}\mathrm{e}^{\tau C/2}\mathrm{e}^{\tau A}\mathrm{e}^{\tau C/2}\mathrm{e}^{\tau B/2}\, z(t-\tau). \tag{2.24}$$

This means that the integration scheme follows these steps: (1) accelerates each body by planet-planet perturbations weighted by the factor $K(r_{ij})$ (the coordinates are fixed) with a step $\tau/2$ (Eq. 2.20); (2) the positions are then modified by a contribution from the momenta (which is fixed at this point) (Eq. 2.21); (3) the bodies are next accelerated by the star for τ and weighted by the term $1 - K(r_{ij})$, which is equal to 0 for a non-encounter or increasing to 1 as $r_{ij} \to r_{\rm crit}$, i.e., when a close encounter is about to happen, as expressed in Eq. 2.19. The scheme finalizes with the repetition of step (2) and then (1).

2.1.4 15th-order Integrator with Adaptive Time-Stepping (`IAS15`)

Unlike `Mercury6`, `IAS15` is a 15th-order implicit predictor-corrector integrator with adaptive time-stepping (Rein and Spiegel, 2015). It is based on the 15th-order Runge-Kutta algorithm[20] of Everhart (1985), which uses Gauss-Radau spacings (Abramowitz and Stegun, 1964) to integrate a second-order derivative that depends on position, velocity and time: $y'' = F(y', y; t)$. The algorithm adjusts the timestep to efficiently resolve the physical scale of the given system and achieve convergence to machine precision.

[19] $r_{\rm crit}$ is given in terms of Hill radii, i.e., $R_{\rm H} = a_{\rm p}(M_{\rm p}/3M_*)^{1/3}$, where $M_{\rm p}$ and $a_{\rm p}$ are the planetary mass and semi-major axis, and M_* the mass of the star.

[20] The Runge-Kutta algorithm better known is that of 4th-order, that is described in several books of numerical methods (e.g. Abramowitz and Stegun, 1964; Hildebrand, 1987a; Press et al., 1992b).

Gauss-Radau quadrature is a scheme for integrating a function $f(y,t)$ by approximating the integral as a weighted sum of the function evaluated at predetermined spacings h_n:

$$\int_0^1 f(x)dx = \frac{2}{n^2}f(0) + \sum_{k=1}^{n-1} W_k f(h_k) + E, \tag{2.25}$$

where

$$E = \frac{2^{2n-1}n[(n-1)!]^4}{[(2n-1)!]^3} f^{(2n-1)}(\xi) \tag{2.26}$$

is the error of the Gauss-Radau quadrature of order $2n-1$ and $f^{(2n-1)}(\xi)$ is the $(2n-1)$th derivative of f evaluated in the range $0 \le \xi \le 1$ (Hildebrand, 1987b). The number of Gauss-Radau spacings and their values depend on the order of the polynomial that is used to approximate the function in the integral in Eq. 2.25. The method requires n points to fit polynomials of degree $2n-1$ or lower, and the number of free abscissas is $n-1$, where the first evaluation is at $h_0 = 0$ for the Radau-like quadratures.

There are different ways to calculate the Gauss-Radau spacings for degree $2n-1$ polynomials. Abramowitz and Stegun (1964) present an analytic equation to find the optimal spacing h_n by treating them as roots of a combination of Legendre polynomials, which are the polynomials used in Gauss-Radau quadrature:

$$\frac{P_n(2h-1) + P_{n-1}(2h-1)}{2h}.$$

In `IAS15`, the degree is $2n-1 = 15$, and therefore $n = 8$. As a consequence, the values of h_n are the roots of

$$\begin{aligned}\frac{P_8(2h-1) + P_7(2h-1)}{2h} &= 6435\,h^7 - 24024\,h^6 + 36036\,h^5 - 27720\,h^4 \\ &\quad + 11550\,h^3 - 2520\,h^2 + 252\,h - 8 = 0.\end{aligned} \tag{2.27}$$

Table 2.1 shows the Gauss-Radau spacings to seven decimal places, and Fig. 2.2 shows the graphical representation of Eq. 2.27.

`IAS15` uses a predictor-corrector scheme to integrate a second-order derivative, $y'' = F(y', y; t)$. It predicts the position, y, and velocity, y', at the next step, t, by first fitting a polynomial to y'' at several computed spacings, h_n, and then integrating the fit. With the predicted y and y', the acceleration is determined at t to correct the values of y and y'. The process is iterated until the values of both y and y' converge to machine precision. Under this scheme, the predictor is given by the polynomial

$$\begin{aligned}y''(h) \approx y''_0 &+ g_0\,h + g_1\,h\,(h-h_1) + g_2\,h\,(h-h_1)(h-h_2) \\ &+ \cdots + g_7\,h\,(h-h_1)\cdots(h-h_7),\end{aligned} \tag{2.28}$$

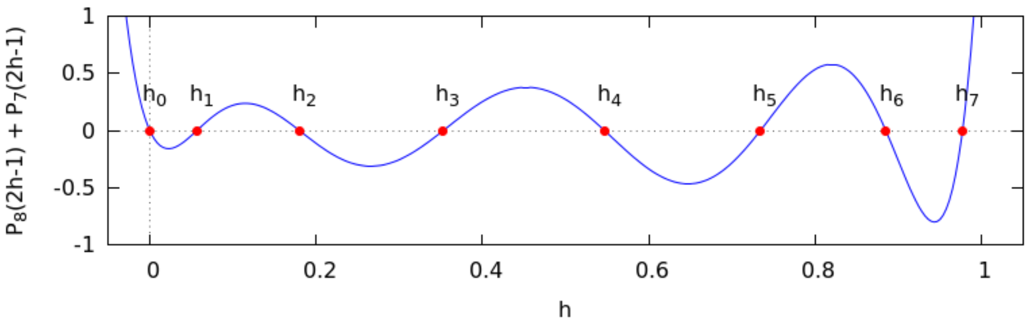

Figure 2.2: Values of the Gauss-Radau spacings (in red) obtained from the roots of Eq. 2.27, which are used to numerically integrate a polynomial of degree 8.

n	h_n
0	0.0
1	0.0562626
2	0.1802407
3	0.3526247
4	0.5471536
5	0.7342102
6	0.8853209
7	0.9775206

Table 2.1: Numerical values of the Gauss-Radau spacings to 7 decimal places. These values are the roots of the Radau polynomial in Eq. 2.27 and represented graphically in Fig. 2.2.

where y_0'' is the acceleration at the start of the step[21], g_k are constants to be determined with units of acceleration, and the h_ns take the values of the Gauss-Radau spacings (Table 2.1). For this approximation, it is assumed that the derivative is smooth and well behaved, and as a consequence, the second-order derivative can also be expressed as a polynomial of t:

$$\begin{aligned} y''(h) &\approx y_0'' + b_0 h + b_1 h^2 + \cdots + b_6 h^7; \\ y''(t) &\approx y_0'' + a_0 t + a_1 t^2 + \cdots + a_6 t^7. \end{aligned} \tag{2.29}$$

Here, $y''(h) = y''(t)$ for timestep dt, $h \equiv t/dt$, and $b_k \equiv a_k\, dt^{k+1}$. The velocity, $y'(h)$, and position, $y(h)$, can be found by integrating Eq. 2.29 once and then twice, with expressions

$$y'(h) \approx y_0' + h\, dt \left(y_0'' + \frac{h}{2} \left(b_0 + \frac{3h}{2} \left(b_1 + \cdots \right) \right) \right), \tag{2.30}$$

$$y(h) \approx y_0 + y_0'\, h\, dt + \frac{h^2\, dt^2}{2} \left(y_0'' + \frac{h}{3} \left(b_0 + \frac{h}{2} \left(b_1 + \cdots \right) \right) \right), \tag{2.31}$$

where y_0' and y_0 are the velocity and position at the beginning of the step. To predict the

[21] When $h = h_0 = 0$.

position and velocity at t, the values of the b_k constants are needed. The constants b_k can be calculated from g_k by equating Eq. 2.28 and 2.29. On the other hand, the estimation of g_k requires that the acceleration, in this case $y'' = GM/r^2$ (for only point-like gravitational forces), is evaluated at each substep h_n. Using the value $y''_n = y''(h_n)$ in conjunction with Eq. 2.28 one finds that

$$\begin{aligned}
h = h_1 \quad &\text{gives} \quad g_0 = \frac{y''_1 - y''_0}{h_1}, \\
h = h_2 \quad &\text{gives} \quad g_1 = \frac{y''_2 - y''_0 - g_0 h_2}{h_2(h_2 - h_1)}, \\
h = h_3 \quad &\text{gives} \quad g_2 = \frac{y''_3 - y''_0 - g_0 h_3 - g_1 h_3(h_3 - h_1)}{h_3(h_3 - h_1)(h_3 - h_2)}
\end{aligned}$$

and so forth. The notation $y''(h_n)$ means that Eqs. 2.31 and 2.30 have been evaluated at the given substep h_n. The values of b_k are either taken to be $b_k = 0$, such as at the start of the simulation, or have been predicted from the previous step. In general,

$$g_k = \frac{y''_{k+1} - y''_0 - \sum\limits_{i=0}^{k-1} g_i \prod\limits_{n=0}^{i} (h_{k+1} - h_n)}{\prod\limits_{n=0}^{k} (h_{k+1} - h_n)} \qquad \text{where} \qquad k = 0, 1, ..., 6. \tag{2.32}$$

It is clear, that the process to find the values g_k is iterative, with a loop over the spacings h_k.

After estimating g_k, those values are used to update the b_ks according to

$$\begin{array}{ccccccccccccccc}
c_{00}\, g_0 & + & c_{10}\, g_1 & + & c_{20}\, g_2 & + & c_{30}\, g_3 & + & c_{40}\, g_4 & + & c_{50}\, g_5 & + & c_{60}\, g_6 & = & b_0 \\
 & & c_{11}\, g_1 & + & c_{21}\, g_2 & + & & & \cdots & & & + & c_{61}\, g_6 & = & b_1 \\
 & & & & c_{22}\, g_2 & + & & & \cdots & & & + & c_{62}\, g_6 & & b_2 \\
 & & & & & & \ddots & & & & & & \vdots & & \vdots \\
 & & & & & & & & & & & & c_{66}\, g_6 & = & b_6
\end{array} \tag{2.33}$$

where the coefficients c_{jk} are constant through all executions of the algorithm and, therefore, calculated just once using the relation

$$c_{jk} = \begin{cases} 1 & \text{for } j = k, \\ -h_j\, c_{j-1,0} & \text{for } j > 0 \text{ and } k = 0, \\ c_{j-1,k-1} - h_j\, c_{j-1,k} & \text{for } k < j. \end{cases} \tag{2.34}$$

The position and velocity can be corrected by substituting the estimated values of b_k into Eqs. 2.31 and 2.30, and using $h = 1$. The procedure from Eq. 2.28 to 2.33 is looped until the convergence criterion is reached. Rein and Spiegel (2015) define this criterion to be

$$\widetilde{\delta b_6} \equiv \frac{\max_i |\delta b_{6,i}|}{\max_i |y_i''|} < 10^{-16}. \tag{2.35}$$

Here, $\delta b_{6,i} = b_{6,i}^{\text{new}} - b_{6,i}^{\text{old}}$ is the difference between the value of b_6 in the previous iteration and that of the present one. The subindex i runs over the three vector components of all particles for both δb_6 and the acceleration y''. Eq. 2.35 takes advantage of the fact that the values of b_k vary slowly and that b_6 is the smallest b_k coefficient. The acceleration is usually dominated by the b_0 coefficient and for this reason, when machine precision is achieved, the value of b_6 is insignificant compared with y''.

The number of iterations for each step can be reduced by predicting the coefficient b_k from the previous values. This is done explicitly using

$$\begin{aligned}
B_0 &= Q\;(7\,b_6 + 6\,b_5 + 5\,b_4 + 4\,b_3 + 3\,b_2 + 2\,b_1 + b_0),\\
B_1 &= Q^2\;(21\,b_6 + 15\,b_5 + 10\,b_4 + 6\,b_3 + 3\,b_2 + b_1),\\
B_2 &= Q^3\;(35\,b_6 + 20\,b_5 + 10\,b_4 + 4\,b_3 + b_2),\\
B_3 &= Q^4\;(35\,b_6 + 15\,b_5 + 5\,b_4 + b_3),\\
B_4 &= Q^5\;(21\,b_6 + 6\,b_5 + b_4),\\
B_5 &= Q^6\;(7\,b_6 + b_5),\\
B_6 &= Q^7\;b_6.
\end{aligned} \tag{2.36}$$

In this case, $Q = dt_{\text{new}}/dt_{\text{old}}$ and B_k denotes the predicted values. This procedure reduces the number of iterations, usually to just two, in the following timestep and accelerates the convergence. With these $B_k \to b_k$, the g_k are recalculated using the reversal of Eqs. 2.33 and 2.34:

$$\begin{array}{ccccccccccccccc}
d_{00}\,b_0 & + & d_{10}\,b_1 & + & d_{20}\,b_2 & + & d_{30}\,b_3 & + & d_{40}\,b_4 & + & d_{50}\,b_5 & + & d_{60}\,b_6 & = & g_0\\
 & & d_{11}\,b_1 & + & d_{21}\,b_2 & + & & & \cdots & & & + & d_{61}\,b_6 & = & g_1\\
 & & & & d_{22}\,b_2 & + & & & \cdots & & & + & d_{62}\,b_6 & = & g_2\\
 & & & & & & \ddots & & & & & & \vdots & & \vdots\\
 & & & & & & & & & & & & d_{66}\,b_6 & = & g_6
\end{array} \tag{2.37}$$

with coefficients given by

$$d_{jk} = \begin{cases} 1 & \text{for } j = k,\\ h_1\, d_{j-1,0} = h_1^{j-1} & \text{for } j > 0 \text{ and } k = 0,\\ d_{j-1,k-1} + h_{k+1}\, d_{j-1,k} & \text{for } k < j. \end{cases} \tag{2.38}$$

The time loop, Eqs. 2.29 to 2.35, continues until the integration time is fulfilled. The time advances by dt when $\widetilde{\delta b_6}$ converges.

A considerable advantage of IAS15 is the adaptive timestep of the algorithm. After y and y' are converged, the current timestep is evaluated and compared with

$$\mathrm{d}t_{\mathrm{need}} = \mathrm{d}t_{\mathrm{used}} \left(\frac{10^{-9}}{\widetilde{b_6}}\right)^{1/7} \qquad \text{where} \qquad \widetilde{b_6} = \frac{\max_i |b_{6,i}|}{\max_i |y_i''|}. \tag{2.39}$$

The subindex i runs in the same way as in Eq. 2.35. If $\mathrm{d}t_{\mathrm{need}} < \mathrm{d}t_{\mathrm{used}}$, then the step is rejected and restarted with $dt = \mathrm{d}t_{\mathrm{need}}$; otherwise, the step, with the estimated values of y and y', are accepted, the time advanced by $\mathrm{d}t_{\mathrm{used}}$, and the timestep changed to $dt \to \mathrm{d}t_{\mathrm{need}}$ in the next step. Rein and Spiegel (2015) chose to update the timestep using Eq. 2.39 to make the step independent of the physical scale of the problem, and therefore the timescales are captured properly without the intervention of the user. The value 10^{-9} was determined to address the possible error sources, mainly the error due to the truncated approximation (Eq. 2.29), which builds-up as $\mathrm{d}t^{15}$ if the timestep is constant. In Figure 2.3, we compare the behavior of the relative energy after 100 orbits of a simulation of the outer Solar System as run by Rein and Spiegel's IAS15. The error, and therefore, the relative energy loss in the Rein and Spiegel implementation and in ours starts to build as $\mathrm{d}t^{15}$ when the timestep is approximately 500 days, and overall, both implementations agree well. When adaptive time-stepping is turned on, most of the additional error sources are random and with values under machine precision. The other strong source of error is the precision lost due to truncation in sums between large and small numbers. Compensated or Kahan summation (Kahan, 1965) is used to track and reduce the build up of random errors, which grow $\propto t^{1/2}$. A complementary graphical summary of the steps in IAS15 is shown in Fig. A.2.

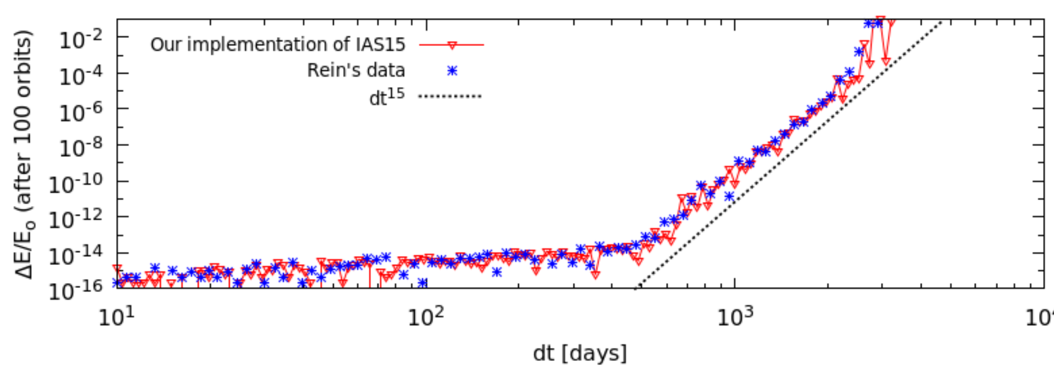

Figure 2.3: Comparison of relative energy after 100 orbits between Rein and Spiegel's IAS15 and our implementation. The timestep was constant, i.e., the adaptive stepping was deactivated. The fractional energy of IAS15 must behave as $\mathrm{d}t^{15}$ when the error term is dominated by the Gauss-Radau quadrature algorithm instead of random round-off error. Our implementation agrees with the previously published implementation.

2.2 Secular code

The equations of motion for a gravitational system with more than two bodies ($N > 2$) are non-integrable. To understand the dynamics of an N-body system, it is necessary to integrate the equations of motion numerically, but this does not elucidate the functional form of the gravitational interaction or highlight how the system evolution depends on different orbital elements. Secular theory is an analytical approximation to the long-term evolution of an N-body system. The approximation takes into account mutual gravitational perturbations from planets or other sources on a given Keplerian orbit and then averages those perturbations over time. These perturbations are modeled as a power series of either Cartesian coordinates or the orbital elements.

We calculate the long-term, or secular, eigenstructure of prototype STIPs by using the Laplace-Lagrange solution as laid out by Murray and Dermott (2000)[22]. The code is available at `https://github.com/norabolig/resmap` and will be described briefly in the following subsections. The code first calculates the characteristic frequencies (eigenfrequencies) of the longitudes of ascending node and pericenter of the secondary masses (e.g., the planets) as described in Sect. 2.2.1. Knowing these eigenfrequencies allows us to evaluate how the system would perturb a test particle. In some cases, an individual, low-mass planet can be treated as a test particle, and if so, we can evaluate the secular forcing on its eccentricity and inclination. However, this must be done with caution, as described below (Sect. 2.2.2). The radial position of the test particle can be varied to explore a range of parameter space and it helps to identify possible eccentricity and inclination resonances.

2.2.1 Secular theory

A secondary body in a hierarchical gravitational system with $N > 2$ masses feels the gravitational effects of the central mass and the other $N-2$ secondary bodies. As an example, consider a three-body system as shown in Fig. 2.4. The equation of motion for the secondaries i and j assuming that the mass i is closer to the star than j (i.e., $r_i < r_j$) is given by

$$\ddot{\mathbf{r}}_i = -\mathcal{G}(m_\mathrm{c} + m_i)\frac{\mathbf{r}_i}{r_i^3} + \mathcal{G}m_j\left(\frac{\mathbf{r}_j - \mathbf{r}_i}{|\mathbf{r}_j - \mathbf{r}_i|^3} - \frac{\mathbf{r}_j}{r_j^3}\right), \tag{2.40}$$

$$\ddot{\mathbf{r}}_j = -\mathcal{G}(m_\mathrm{c} + m_j)\frac{\mathbf{r}_j}{r_j^3} + \mathcal{G}m_i\left(\frac{\mathbf{r}_i - \mathbf{r}_j}{|\mathbf{r}_i - \mathbf{r}_j|^3} - \frac{\mathbf{r}_i}{r_i^3}\right). \tag{2.41}$$

[22]The original development of the Laplace-Lagrange solution was developed by Brouwer and Clemence (1961), but we followed the notation of Murray and Dermott (2000).

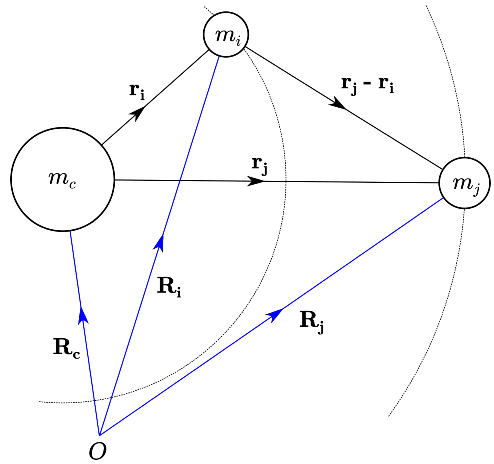

Figure 2.4: Geometry used for the secular theory development. The central body (the most massive) is denoted as m_{c}, and the two companions by m_i and m_j, where m_i is closer to the central body than m_j (i.e., $r_i < r_j$). The dotted arcs represent the orbits of the masses m_i and m_j. Finally, O is the origin of the reference frame.

The right-hand side can be represented by the gradient of two scalar potentials:

$$\ddot{\mathbf{r}}_i = \boldsymbol{\nabla}_i \left(U_i + \mathcal{R}_i\right) = \boldsymbol{\nabla}_i \left[\frac{\mathcal{G}(m_{\mathrm{c}} + m_i)}{r_i} + \mathcal{G}m_j \left(\frac{1}{|\mathbf{r}_j - \mathbf{r}_i|} - \frac{\mathbf{r}_j \cdot \mathbf{r}_i}{r_j^3}\right)\right], \tag{2.42}$$

$$\ddot{\mathbf{r}}_j = \boldsymbol{\nabla}_j \left(U_j + \mathcal{R}_j\right) = \boldsymbol{\nabla}_j \left[\frac{\mathcal{G}(m_{\mathrm{c}} + m_j)}{r_j} + \mathcal{G}m_i \left(\frac{1}{|\mathbf{r}_i - \mathbf{r}_j|} - \frac{\mathbf{r}_i \cdot \mathbf{r}_j}{r_i^3}\right)\right], \tag{2.43}$$

where $U_k = \mathcal{G}(m_{\mathrm{c}} + m_k)/r_k$ is the central potential felt by mass m_k $(k = i, j)$. The potential $\mathcal{R}_k$, given by the second and third terms in Eqs. 2.42 and 2.43, is the *disturbing function*, which is due to the additional secondary masses in the system. This can be explicitly written as

$$\mathcal{R}_i = \mu_j \left(\frac{1}{|\mathbf{r}_j - \mathbf{r}_i|} - \frac{\mathbf{r}_j \cdot \mathbf{r}_i}{r_j^3}\right) \qquad \text{for the inner secondary and} \tag{2.44}$$

$$\mathcal{R}_j = \mu_i \left(\frac{1}{|\mathbf{r}_i - \mathbf{r}_j|} - \frac{\mathbf{r}_i \cdot \mathbf{r}_j}{r_i^3}\right) \qquad \text{for the outer secondary,} \tag{2.45}$$

where $\mu_k = Gm_k$. For simplicity, the disturbing function is divided into direct and indirect terms. The first term in Eqs. 2.44 and 2.45 is the direct part, $\mathcal{R}_{\mathrm{D}}$, while the indirect part, given by the second term in both Eqs. 2.44 and 2.45, is represented by $\mathcal{R}_{\mathrm{E}}$ and $\mathcal{R}_{\mathrm{I}}$. $\mathcal{R}_{\mathrm{E}}$ is the indirect contribution due to an external perturber (in Eq. 2.44), and $\mathcal{R}_{\mathrm{I}}$ is due to an internal perturber (Eq. 2.45). Using the ratio of semi-major axes $\alpha_{ij} = a_i/a_j < 1$ and the dot product $\mathbf{r}_i \cdot \mathbf{r}_j = r_i r_j \cos\psi$, the disturbing function can be expressed as

$$\mathcal{R}_i = \frac{\mu_j}{a_j} \left(\mathcal{R}_{\mathrm{D}} + \alpha_{ij}\mathcal{R}_{\mathrm{E}}\right) \tag{2.46}$$

$$\mathcal{R}_j = \frac{\mu_i}{a_i}\left(\alpha_{ij}\mathcal{R}_{\mathrm{D}} + \frac{\mathcal{R}_{\mathrm{I}}}{\alpha_{ij}}\right). \tag{2.47}$$

Furthermore,

$$\mathcal{R}_{\mathrm{D}} \equiv \frac{a_j}{|\mathbf{r}_j - \mathbf{r}_i|}, \tag{2.48}$$

$$\mathcal{R}_{\mathrm{E}} \equiv -\left(\frac{r_i}{a_i}\right)\left(\frac{a_j}{r_j}\right)^2 \cos\psi, \tag{2.49}$$

$$\mathcal{R}_{\mathrm{I}} \equiv -\left(\frac{r_j}{a_j}\right)\left(\frac{a_i}{r_i}\right)^2 \cos\psi. \tag{2.50}$$

Here, ψ is the angle between r_i and r_j.

The direct and indirect parts of the disturbing function can be represented in a series expansion of the orbital elements that has a general form

$$\mathcal{R}_i = \mu_j \sum S(a_i, a_j, e_i, e_j, I_i, I_j)\cos\varphi, \tag{2.51}$$

where S is a function of the semi-major axes (a), eccentricities (e) and inclinations (I) of masses i and j. The argument, φ, is a linear combination of the mean (λ), apsidal (ϖ) and nodal longitudes (Ω), such that

$$\varphi = k_1\lambda_j + k_2\lambda_i + k_3\varpi_j + k_4\varpi_i + k_5\Omega_j + k_6\Omega_i. \tag{2.52}$$

The coefficients k_i are integers that sum to zero. Whether the disturbing function represents secular and/or resonant interactions depends on the product k_i with the corresponding longitude (λ, ϖ, or Ω). The number of relevant terms can be reduced if some of the cosine terms can be ignored. This is motivated by the *averaging principle*, which assumes that all of the unimportant terms of the disturbing function will have short periods and their effects average to zero over long timescales. In a two-body system, the mean longitude of the secondary mass increases linearly with time because $\dot{\lambda} = n$, but the apsidal and nodal longitudes are constant because $\dot{\varpi} = \dot{\Omega} = 0$. In comparison, when there are two or more secondaries in the system, λ_k varies rapidly, but ϖ_k and Ω_k slowly. This means that the mean longitude has a shorter period than the apsidal and nodal longitudes.

The long-period behavior of the argument in Eq. 2.52 depends as well on the possible commensurabilities between $k_1\lambda_i$ and $k_2\lambda_j$. If $k_1\lambda_i \approx k_2\lambda_j$, then $k_1 n_i - k_2 n_j \approx 0$ and the timescale of the interaction is long. In this case, terms associated with $k_1 = q$ and $k_2 = p - q$, with p and q being integers, must also be considered in both $\mathcal{R}_{\mathrm{D}}$ and $\mathcal{R}_{\mathrm{E,I}}$. The value of p provides the order of the resonant terms and the strength of the resonance is proportional to the eccentricity $S \propto e^{|p|}$ (with $e < 1$). As a consequence, the first-order resonances are typically the strongest (Murray and Dermott, 2000).

To proceed, the disturbing function is often expanded in orbital elements to the desired order and a solution is then found for the simplified equations. In the Laplace-Lagrange solution, only the terms that are second order in e and I and first order in mass are retained. As a consequence of the averaging principle, the secular terms of the disturbing function are those that have long periods, and therefore, do not depend on the mean longitudes, λ. This in turn requires $k_1 = k_2 = 0$ in Eq. 2.52. Murray and Dermott (2000) show that the literal expansion of the direct part of the disturbing function to second order in e and I, assuming that I is small, is:

$$\begin{aligned} \mathcal{R}_{\mathrm{D}}^{(\mathrm{sec})} &= \frac{1}{8}\alpha_{ij}\, b_{3/2}^{(1)}\, \left(e_i^2 + e_j^2\right) - \frac{1}{8}\alpha_{ij}\, b_{3/2}^{(1)}\left(I_i^2 + I_j^2\right) \\ &- \frac{1}{4}\alpha_{ij}\, b_{3/2}^{(2)}\, e_i e_j \cos(\varpi_i - \varpi_j) + \frac{1}{4}\alpha_{ij}\, b_{3/2}^{(1)}\, I_i I_j \cos(\Omega_i - \Omega_j). \end{aligned} \tag{2.53}$$

Here, I represents the inclination and the subindex i denotes a particle, and $b_s^{(k)}(\alpha_{ij})$ are the Laplace coefficients defined as

$$\frac{1}{2}\, b_s^{(k)}(\alpha_{ij}) = \frac{1}{2\pi}\int_0^{2\pi} \frac{\cos k\psi}{\left(1 - 2\alpha_{ij}\cos\psi + \alpha_{ij}^2\right)^s}\, \mathrm{d}\psi. \tag{2.54}$$

Then, from Eq. 2.46 and 2.47, the secular disturbing function for the inner and outer planets are

$$\mathcal{R}_i = \frac{Gm_j}{a_j}\,\mathcal{R}_{\mathrm{D}}^{(\mathrm{sec})} \tag{2.55}$$

$$\mathcal{R}_j = \frac{Gm_i}{a_i}\,\alpha_{ij}\,\mathcal{R}_{\mathrm{D}}^{(\mathrm{sec})} = \frac{Gm_i}{a_j}\,\mathcal{R}_{\mathrm{D}}^{(\mathrm{sec})} \tag{2.56}$$

given that all terms in $\mathcal{R}_{\mathrm{E}}$ and $\mathcal{R}_{\mathrm{I}}$ depend of the mean longitude (see Eqs. 6.110 and 6.111 Murray and Dermott, 2000). Expression 2.53 is only valid whenever mean motion commensurabilities are absent. Otherwise, additional terms should be considered in $\mathcal{R}_{\mathrm{D}}^{(\mathrm{sec})}$ and the indirect part should be included.

Substituting Eq. 2.53 into Eqs. 2.55 and 2.56, and using $G = n_i^2 a_i^3/(m_{\mathrm{c}} + m_i) = {n_j}^2 {a_j}^3/(m_{\mathrm{c}} + m_j)$, where n is the mean motion, we can represent both $\mathcal{R}_i$ and $\mathcal{R}_j$ as

$$\begin{aligned} \mathcal{R}_i = n_i a_i^2 \Bigg[&\frac{1}{2} A_{ii}\, e_i^2 + A_{ij}\, e_i e_j \cos(\varpi_i - \varpi_j) \\ &+ \frac{1}{2} B_{ii}\, I_i^2 + B_{ij}\, I_i I_j \cos(\Omega_i - \Omega_j) \Bigg], \end{aligned} \tag{2.57}$$

for $i = 1, 2$ and $j = 2, 1$, and

$$A_{ii} = +\frac{1}{4}\frac{m_j}{m_{\mathrm{c}} + m_i}\, n_i\, \alpha_{ij}\, \bar{\alpha}_{ij}\, b_{3/2}^{(1)}(\alpha_{ij}) \tag{2.58}$$

$$A_{ij} = -\frac{1}{4}\frac{m_j}{m_c + m_i}\, n_i\, \alpha_{ij}\, \bar{\alpha}_{ij}\, b^{(2)}_{3/2}(\alpha_{ij}) \tag{2.59}$$

$$B_{ii} = -\frac{1}{4}\frac{m_j}{m_c + m_i}\, n_i\, \alpha_{ij}\, \bar{\alpha}_{ij}\, b^{(1)}_{3/2}(\alpha_{ij}) \tag{2.60}$$

$$B_{ij} = +\frac{1}{4}\frac{m_j}{m_c + m_i}\, n_i\, \alpha_{ij}\, \bar{\alpha}_{ij}\, b^{(1)}_{3/2}(\alpha_{ij}) \tag{2.61}$$

where

$$\bar{\alpha}_{ij} = \begin{cases} \alpha_{ij} & \text{external perturber, if } i < j \\ 1 & \text{internal perturber, if } i > j. \end{cases} \tag{2.62}$$

In this way, Eq. 2.57 can be represented in matrix form after recognizing that the terms A_{ij} and B_{ij} are the elements of the matrices

$$\mathbf{A} = \begin{pmatrix} A_{11} & A_{12} \\ A_{21} & A_{22} \end{pmatrix} \qquad \text{and} \qquad \mathbf{B} = \begin{pmatrix} B_{11} & B_{12} \\ B_{21} & B_{22} \end{pmatrix}.$$

The Laplace-Lagrange secular solution makes use of the eccentricity and inclination vectors, as shown in Fig. 2.5, and defined as

$$h_i = e_i\, \sin\varpi_i, \qquad k_i = e_i\, \cos\varpi_i, \tag{2.63}$$

$$p_i = I_i\, \sin\Omega_i, \qquad q_i = I_i\, \cos\Omega_i, \tag{2.64}$$

to substitute the corresponding terms in Eq. 2.57. Using trigonometric identities, the result can be expressed as

$$\mathcal{R}_i = n_i a_i^2 \left[\frac{1}{2} A_{ii}\,(h_i^2 + k_i^2) + A_{ij}\,(h_i h_j + k_i k_j) + \frac{1}{2} B_{ii}\,(p_i^2 + q_i^2) + B_{ij}\,(p_i p_j + q_i q_j) \right]. \tag{2.65}$$

Now, we seek to use Eq. 2.65 to find the time evolution of the system, namely $\dot{h}_i$, $\dot{k}_i$, $\dot{p}_i$, and

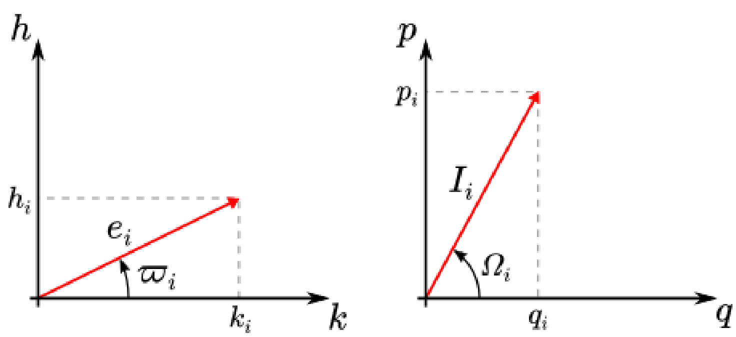

Figure 2.5: Graphical depiction of the eccentricity (left) and inclination (right) vectors described in Eqs. 2.63 and 2.64, and used throughout Sect. 2.2.1.

$\dot{q}_i$. The corresponding relationships between the disturbing function and the derivatives of the inclination and eccentricity vectors are (Murray and Dermott, 2000, p. 278)

$$\dot{h}_i = \frac{1}{n_i a_i^2} \frac{\partial \mathcal{R}_i}{\partial k_i}, \qquad \dot{k}_i = -\frac{1}{n_i a_i^2} \frac{\partial \mathcal{R}_i}{\partial k_i}, \tag{2.66}$$

$$\dot{p}_i = \frac{1}{n_i a_i^2} \frac{\partial \mathcal{R}_i}{\partial q_i}, \qquad \dot{q}_i = -\frac{1}{n_i a_i^2} \frac{\partial \mathcal{R}_i}{\partial p_i}. \tag{2.67}$$

For two secondaries ($i = 1, 2$), this results in a system of equations

$$\dot{h}_1 = A_{11}k_1 + A_{12}k_2, \qquad \dot{h}_2 = A_{21}k_1 + A_{22}k_2, \tag{2.68}$$

$$\dot{p}_1 = B_{11}q_1 + B_{12}q_2, \qquad \dot{p}_2 = B_{21}q_1 + B_{22}q_2, \tag{2.69}$$

for which the corresponding solutions have the form, recalling the expressions for the eccentricity and inclination vectors (Eqs. 2.63 and 2.64):

$$h_i = e_i \sin(g\,t + \beta), \qquad k_i = e_i \cos(g\,t + \beta), \tag{2.70}$$

$$p_i = I_i \sin(f\,t + \gamma), \qquad q_i = I_i \cos(f\,t + \gamma). \tag{2.71}$$

By substituting Eq. 2.70 in Eq. 2.68, the problem is reduced to finding the eigenvalues of the matrix **A** and **B**, denoted by g and f, respectively. For example, if the system of equations in Eq. 2.68 is expressed in matrix form after taking the derivative of h_i (Eq. 2.70), then

$$\begin{pmatrix} \dot{h}_1 \\ \dot{h}_2 \end{pmatrix} = g \begin{pmatrix} e_1 \\ e_2 \end{pmatrix} = \begin{pmatrix} A_{11} & A_{12} \\ A_{21} & A_{22} \end{pmatrix} \begin{pmatrix} e_1 \\ e_2 \end{pmatrix},$$

which is an eigenvalue problem. The same is applicable for **B** in terms of p and q (Eq. 2.71). The number of eigenvalues depends on the number of secondaries (N) considered in the calculation. Thus, the coefficients e_i and I_i are the eigenvectors[23] of the matrices **A** and **B**, whose values need to be determined together with the phases β_i and γ_i. The eigenvectors can be found by replacing each eigenvalue in the corresponding set of equations and solving for the vector, but the resulting eigenvector is unscaled. The boundary conditions are necessary to scale the eigenvectors and to calculate the phases (see Sect 7.3 of Murray and Dermott, 2000, for more details).

Once the eigenvalues and the eigenvectors are known, the time dependence of the components of the eccentricity and inclination vector are expressed as

$$h_i = \sum_l^N e_{il} \sin(g_l\,t + \beta_l), \qquad k_i = \sum_l^N e_{il} \cos(g_l\,t + \beta_l),$$

[23] Here, $e_i \to e_{il}$ and $I_i \to I_{il}$, where l denotes the mode number associated with the eigenvalue g_l or f_l.

$$p_i = \sum_{l}^{N} I_{il} \sin(f_l\, t + \gamma_l), \qquad\qquad q_i = \sum_{l}^{N} I_{il} \cos(f_l\, t + \gamma_l).$$

The eccentricity and inclination value at any time is given by the magnitude of the analogous vector.

Physically, the eigenvalues found in the Laplace-Lagrange secular solution represent the theoretical characteristic precession rates of the longitudes of pericenter and ascending node of the system. Throughout this work, we will refer to the eigenvalues as eigenfrequencies of a given system due to their association with the precession rates. The g_i eigenfrequencies are associated with the precession rate of ϖ_i, while f_i are associated with Ω_i, where i indicates the mode number and not a mass. The comparison of the theoretical secular eigenfrequencies and synthetic precession frequencies (described in detail Sect. 2.3) provide insight into the dynamics of a system, particularly if the number or values of the fundamental frequencies (or both) mismatch. The discrepancy can be due to neglected resonant interactions in the theoretical calculation. For a case study presented in Ch. 4, we compare the eigenfrequencies from secular theory with the numerically-derived principal frequencies for two different systems that have high planet multiplicity. The same principles laid out here can be applied to a system with more than two secondaries, in which Eqs. 2.57, 2.65, 2.68, 2.69, 2.70 and 2.71 change to the corresponding equations in Appendix A.2.

2.2.2 Forced eccentricity and inclination

After the eigenfrequencies have been estimated, a test particle can be included in the secular theory to map the gravitational influence of the secondary masses on the particle's location. The number of eigenfrequencies in this new system increases by one without modifying the value of the eigenfrequencies found in Sect. 2.2.1 because the extra body has zero mass. Our secular code exploits this feature to map the system's secular behavior by placing many test particles (one a time) over a range of semi-major axes. Thus, for a test particle with orbital elements n, a, e, I, ϖ and Ω in a system with N secondaries, the particle's secular disturbing function (analogous to Eq. 2.65) is

$$\begin{aligned}\mathcal{R} = na^2 \Bigg[&\frac{1}{2} A\,(h^2 + k^2) + \frac{1}{2} B\,(p^2 + q^2) \\ &+ \sum_{j=1}^{N} A_j\,(h\,h_j + k\,k_j) + \sum_{j=1}^{N} B_j\,(p\,p_j + q\,q_j) \Bigg].\end{aligned} \tag{2.72}$$

The solutions to this equation have the form of a forced harmonic oscillator:

$$h = e_{\text{free}} \sin(A\,t + \beta) + h_0(t), \qquad\qquad k = e_{\text{free}} \cos(A\,t + \beta) + k_0(t), \tag{2.73}$$

$$p = I_{\rm free}\sin(B\,t+\gamma)+p_0(t), \qquad\qquad q = I_{\rm free}\cos(B\,t+\gamma)+q_0(t), \tag{2.74}$$

where

$$\begin{aligned} h_0(t) &= -\sum_i^N\sum_l^N \frac{A_i e_{il}}{A-g_l}\sin(g_l\,t+\beta_l), \\ k_0(t) &= -\sum_i^N\sum_l^N \frac{A_i e_{il}}{A-g_l}\cos(g_l\,t+\beta_l), \end{aligned} \tag{2.75}$$

$$\begin{aligned} p_0(t) &= -\sum_i^N\sum_l^N \frac{B_i I_{il}}{B-f_l}\sin(f_l\,t+\gamma_l), \\ q_0(t) &= -\sum_i^N\sum_l^N \frac{B_i I_{il}}{B-f_l}\cos(f_l\,t+\gamma_l), \end{aligned} \tag{2.76}$$

and

$$A = \frac{1}{4}\frac{n}{m_{\rm c}}\sum_{j=1}^N m_j\,\alpha_j\,\bar{\alpha}_j\,b_{3/2}^{(1)}(\alpha_j) \tag{2.77}$$

$$B = -\frac{1}{4}\frac{n}{m_{\rm c}}\sum_{j=1}^N m_j\,\alpha_j\,\bar{\alpha}_j\,b_{3/2}^{(1)}(\alpha_j). \tag{2.78}$$

In Eqs. 2.73 and 2.74, the first terms are the free (proper) eccentricity and inclination vectors of the test particle, while the second terms are the forced eccentricity and inclination vectors. The forced eccentricity and inclination values are obtained from the normalization of vectors (k_0, h_0) (Eq. 2.75) and (p_0, q_0) (Eq. 2.76), respectively.

Secular resonances originate when the denominators $A - g_l$ and $B - f_l$ in Eqs. 2.75 and 2.76 are close to zero. This occurs when the particle's semi-major axis generates an A or B value that matches one of the system's eigenfrequencies. This situation, for either a secular eccentricity or inclination resonance, is of particular interest for the STIPs case study.

2.3 Synthetic secular theory

The synthetic secular theory comes from analyzing the frequency components of the orbital precession rates among planets in a given system. A system is evolved in an N-body integrator for a set period of time. Then, the osculating orbital elements are calculated and transformed to Fourier space to obtain the principal frequency components of the eccentricity and inclination vectors

$$\mathbf{e}(t) = (h,k)(t) = (e\,\sin\varpi,\ e\,\cos\varpi) \tag{2.79}$$

$$\mathbf{I}(t) = (p, q)(t) = (\sin I\, \sin\Omega,\, \sin I\, \cos\Omega), \tag{2.80}$$

where e is the eccentricity, I the inclination, ϖ the longitude of pericenter and Ω the longitude of ascending node. Finally, the value of the principal frequencies of the synthetic secular theory are compared to the eigenfrequencies of secular theory. We emphasize that both synthetic and theoretical secular frequencies represent the precession of the eccentricity or inclination vector, $\dot{\varpi}$ or $\dot{\Omega}$, respectively. When a system with N masses is characterized well by the Laplace-Lagrange theory, the synthetic and theoretical precession rates should match; otherwise, the disagreement indicates that strong-gravitational or long-term interactions were neglected in the secular theory calculation.

The Fourier transform (FT) converts a time series into the frequency domain. The transformation is implemented by using either the orthogonality of $\sin(2\pi\nu t)$ and $\cos(2\pi\nu t)$, or by using $\exp(-j2\pi\nu t)$ functions. For the same reason, different normalizations can be found in the literature. The FT used throughout this work is

$$F(\nu) = \mathcal{F}_t[f(t)](\nu) = \int_{-\infty}^{\infty} f(t)\, \mathrm{e}^{-j2\pi\nu t}\, \mathrm{d}t, \tag{2.81}$$

where ν is the linear frequency, $f(t)$ is a time-dependent function and $F(\nu)$ is the FT of $f(t)$, which is a function only on ν. Because we will examine discrete times and frequencies, the corresponding discrete Fourier transform (DFT) is used:

$$F_n = \mathcal{F}_k[\{f_k\}_{k=0}^{N-1}](n) \equiv \sum_{k=0}^{N-1} f_k\, \mathrm{e}^{-j2\pi nk/N}. \tag{2.82}$$

The kernels in Eqs. 2.81 and 2.82 are related through the k-time $t \to t_k = k\Delta t$, and the n-frequency $\nu \to \nu_n = \frac{n}{N\Delta t}$, where N is the total number of time samplings and Δt is the time sampling interval. In Eq. 2.82, f_k is the discrete time series to be transformed to Fourier space, which is $\mathbf{e}(t_k)$ and $\mathbf{I}(t_k)$ in our case. We use the Python predefined function `np.fft.rfft` to perform the DFT, which implements a fast Fourier transform (FFT) for real f_k data.

The outcome of the DFT is the complex precession spectrum of $\mathbf{e}(j\nu_n)$ and $\mathbf{I}(j\nu_n)$. The amplitude and phase of the spectra are of interest because the former indicates which frequencies dominate the data and the latter shows how the sinusoids are aligned. The amplitude is given by

$$A_n = \begin{cases} |F_n|/N & \text{for } n = 0, \\ 2|F_n|/N & \text{for } n > 0, \end{cases} \tag{2.83}$$

where $|F_n|$ is the modulus of the complex spectrum, which is the magnitude of the corresponding eccentricity and inclination vectors as functions of the precession frequency ν_n. The frequencies that correspond to the highest amplitude values are the principal components of the spectrum.

The phase is given by the complex argument

$$\phi = \tan^{-1}\left(\frac{\mathrm{Im}(F_n)}{\mathrm{Re}(F_n)}\right). \tag{2.84}$$

Here, Im() and Re() denote the imaginary and real parts of the complex number, respectively.

In the following two chapters, we will use the methods and codes described throughout this chapter. We point out that `Mercury6` was just slightly modified to include the GR correction using Eq. 2.1. On the other hand, the `IAS15` implementation was completely written by me following Rein and Spiegel (2015) algorithm. In `IAS15`, we included, besides the planet-star and planet-planet gravitational forces, the GR correction used in `Mercury6`, and a prescription for gaseous tidal damping of eccentricity and inclination (see Sect. 2.1.1, particularly Eq. 2.2).

Chapter 3

Close-in giant planets as an extreme outcome of planet-planet scattering.

Volk and Gladman (2015) showed that the observed extrasolar planetary systems are metastable, i.e., in statistical realizations with slightly perturbed initial conditions, these systems tend toward instability in various timescales, especially those at short orbital periods. As a consequence, the multiplicity of STIPs tends to decay with time due to planet-planet scattering, collisions and consolidation. Thus, the high-multiplicity STIPs observed today are the longest-lived variants and could be representative of typical formation configurations. We suggest that the intrinsic metastability of STIPs leads to a variety of planetary types that form *in situ* at short orbital periods. The properties of the planets produced in this scenario depend of the details of the consolidation, including the relative timing of instability compared with gaseous lifetimes. The formation of a HJ could be an extreme dynamical outcome of a STIP, should a large core form through consolidation and enable runaway gas accretion. Here, we consider a gas giant to be any planet that has at least half of its mass in captured nebular gas.

The critical mass needed to initiate runaway accretion depends on different parameters, e.g., the distance from the star, gas density profile, planetesimal accretion rate, etc. (Lee et al., 2014; Piso et al., 2015). In this study, we use a simple parametrization and define a critical mass to be $m_{\rm c} = 10M_{\oplus}$, independent of the distance from the star. We also assume that the formation of short orbital period planets, with masses between 1 and 4 $M_{\oplus}$, occurs within a Myr of the disk lifetime (Dawson et al., 2015) and therefore, the gaseous disk is still present. Observations of circumstellar disks around young stars in clusters show that the fraction of stars with detectable disks decays exponentially with time, $\propto \exp(-t/\lambda)$, with an average timescale $\lambda = 2.5$ Myr (Mamajek, 2009). If we consider this to represent, on average, the decay timescale for gas in a disk, then the disk's density would decrease to 50% of the initial value by $t = 1.7$ Myr. Hence, any considerable accretion of gas by a planetary embryo should take place within the first 2 Myr. While the zero point for the time is ill-defined, we take t to be the time from STIP formation, which is envisaged to occur essentially along with disk formation.

Fig. 3.1 shows different planet formation outcomes that could occur in the *in situ* formation framework. The successful *in situ* formation of a gas short-period giant (gSPG), with $M > 10M_{\oplus}$ and 50% of its mass in gas requires: (1) the ubiquitous formation of a high-multiplicity

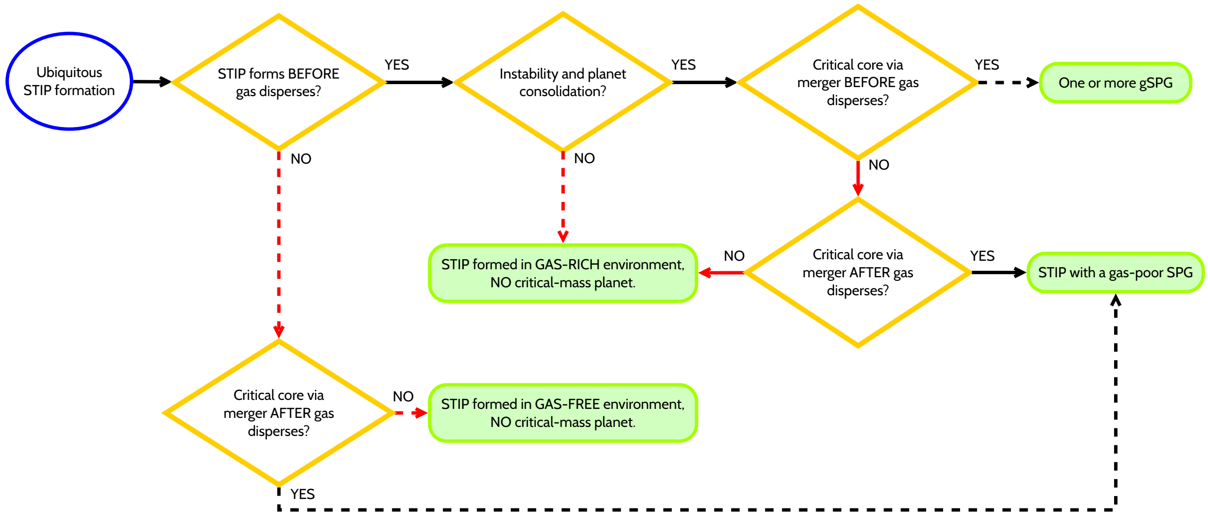

Figure 3.1: *In situ* formation pathways of short-orbital period planets (adapted from Boley et al., 2016). Timing between consolidation and gas dissipation/availability is key in this paradigm, with the formation of a gSPG representing an extreme outcome. Dashed-lines represent evolution pathways that we conceive uncommon.

STIP within 1 Myr, and thus, before the gas disperses from the disk; (2) instability of the primordial STIP in the presence of a gaseous disk, which leads to the collision and consolidation of planetary cores; (3) the subsequent consolidation of a critical core to start runaway accretion of gas, and; (4) a consolidation occurring within the first 2 Myr of the disk lifetime.

Among the confirmed exoplanets, there is a large population with sizes between 1 $R_\oplus$ and 4 $R_\oplus$ (Howard et al., 2010; Batalha et al., 2013; Petigura et al., 2013; Dong and Zhu, 2013; Fressin et al., 2013; Rowe et al., 2014), also known as super-Earths, with measured masses within $2 \leq M_\mathrm{p}/M_\oplus \leq 20$ (Wu and Lithwick, 2013; Weiss and Marcy, 2014). Close-in super-Earths are puzzling due to their upper mass range and current separation from the host star, for which the upper masses could have underwent runaway accretion. Nonetheless, the estimated gas content by mass of these objects is $\lesssim 10\%$ (Lopez and Fortney, 2014; Rogers and Seager, 2010b,a), which suggests forestalled runaway gas accretion. In the paradigm suggested in this work, massive super-Earths originate from a different pathway than gSPGs. Super-Earths are critical cores consolidated after 2 Myr, when the gas has significantly dissipated. Depending on the accreted gas mass, the planet resembles either a mini-Neptune or a super-Earth. Unlike gSPGs, short-period giants (SPGs) are planets at or above the critical mass but that failed to accrete a significant gaseous envelope. Examples of such a planet include K2-66 b (Sinukoff et al., 2017) and Kepler-62 d (Borucki et al., 2013). As shown in Fig. 3.1, other pathways are also possible, e.g., rocky planets can form through accretion of solid material after the gaseous disk disperses.

Using numerical simulations, we determine whether it is plausible for critical cores to consolidate from metastable STIPs, and if so, whether such consolidation occurs at times during which gas may still be present.

3.1 Simulations and prototype STIPs.

We evaluate the outcomes of STIP metastability and planet consolidation by running two sets of N-body simulations. The first set of simulations includes, for simplicity, only planet-planet and planet-star gravitational interactions, i.e., we neglect interactions between the planets and the gaseous disk. This part of the study serves as a proof of concept, exploring whether metastability can drive the consolidation of critical cores within a few million years (Sect. 3.1.1).

For the second part of the study (Sect. 3.1.2), we explore how planet-disk interactions can alter the dynamics of STIPs. While this could be studied directly using hydrodynamics simulations, such simulations are very expensive, even for short integration timescales. An alternative is to include prescriptions for planet-disk interactions in an N-body integrator. This is the approach we take, using a gaseous tidal damping algorithm based on the results of hydrodynamics simulations with embedded planets (Cresswell et al., 2007; Tanaka and Ward, 2004). Gaseous tidal damping is an outcome of the interaction between the spiral density waves within a disk and the planets that excite those waves. These spiral waves, in turn, reduce the orbital eccentricity and inclination of planets within a disk and can drastically affect planet orbital stability.

Due to the different physics required for each of these parts, we use different N-body integrators for each study. In the simulations without gas drag, we ran 1000 realizations of K11 (see Table 3.1) in Mercury6. For the simulations with gas damping, we used our implementation of `IAS15` to include non-conservative forces. We also generated synthetic six-planet STIPs, as we found

Planet	P (days)	$R_{\rm p}$ ($R_\oplus$)	$M_{\rm p}$ ($M_\oplus$)	a (au)	e	I (°)	ω (°)
b	$10.3039^{+0.0006}_{-0.0010}$	$1.80^{+0.03}_{-0.05}$	$1.9^{+1.4}_{-1.0}$	0.09	$0.045^{+0.068}_{-0.042}$	0.12	45.0
c	$13.0241^{+0.0013}_{-0.0008}$	$2.87^{+0.05}_{-0.06}$	$2.9^{+2.9}_{-1.6}$	0.11	$0.026^{+0.063}_{-0.013}$	0.07	51.3
d	$22.6845^{+0.0009}_{-0.0009}$	$3.12^{+0.06}_{-0.07}$	$7.3^{+0.8}_{-1.5}$	0.15	$0.004^{+0.007}_{-0.002}$	0.15	146.3
e	$31.9996^{+0.0008}_{-0.0012}$	$4.19^{+0.07}_{-0.09}$	$8.0^{+1.5}_{-2.1}$	0.19	$0.012^{+0.006}_{-0.006}$	0.63	90.0
f	$46.6888^{+0.0027}_{-0.0032}$	$2.49^{+0.04}_{-0.07}$	$2.0^{+0.8}_{-0.9}$	0.25	$0.013^{+0.011}_{-0.009}$	0.05	90.0
g	$118.3807^{+0.0010}_{-0.0006}$	$3.33^{+0.06}_{-0.08}$	< 25.0	0.47	< 0.15	0.35	90.0
$M_* = 0.961 \pm 0.025\, M_\odot$	$R_* = 1.065^{+0.017}_{-0.022}\, R_\odot$						

Table 3.1: Nominal orbital elements of the known planets of Kepler-11 (K11) (Lissauer et al., 2011a, 2013). These values are a product of observational measurements and dynamical modeling. The nominal values provided by (Lissauer et al., 2013) for K11 are within 1σ confidence intervals, except for the mass and eccentricity of K11g with 2σ upper bounds.

the K11 configuration to show no signs of instability in the presence of gas. All the simulation suites with more than 300 members were run on the Orcinus computing cluster, provided by WestGrid (`www.westgrid.ca`) and Compute Canada Calcul Canada (`www.computecanada.ca`).

3.1.1 Gas-free gravitational interactions

The masses and spatial distributions of STIPs shortly after formation is unknown. However, due to their metastability, we argue that the high multiplicity STIPs observed today are among the longest-lived configurations of "initial" conditions after the main phases of planet building. Following this line of thought, we concentrated on using a well-characterized STIP, with more than five detected planets, as a template for our first study.

The number of systems detected to date with more than five planets is small. Nine of the 2816 confirmed systems harbor more than five planets, and only Kepler-90 (K90) (with eight planets now known) resembles the multiplicity of the Solar System (Schneider et al., 2011). At the start of this work, before the detection of TRAPPIST-1 (Gillon et al., 2016), the STIPs with the highest multiplicities included Kepler-11 (K11) (Lissauer et al., 2011a, 2013) and Kepler-90 (K90) (Cabrera et al., 2014; Lissauer et al., 2014b; Schmitt et al., 2014), with six and seven planets[24], respectively. K11 was chosen to serve as a prototype because the planetary masses and semi-major axes are well characterized. In addition, constraints on the orbital eccentricities, inclinations and arguments of pericenter (Table 3.1) were also available due to a combination of transit observations, TTVs, and dynamical modeling (Lissauer et al., 2013). The exception is K11g, the outermost planet, which only has an upper mass and eccentricity limit of $M < 25.0\,M_\oplus$ and $e < 0.15$ provided by stability tests (Lissauer et al., 2013). Details of the K11 system are given in Table 3.1.

We performed a suite of 1000 numerical simulations based on the nominal masses and semi-major axes of the K11 planets. We set the mass of K11g to be $8\,M_\oplus$, which is well under the upper limit constrained by stability analyses and reduces the possibility that this planet dominates the dynamics of the STIP. Thus, the total planetary mass of the K11 analogues is $M_T = 30.1\,M_\oplus$. The orbital eccentricity, e, longitude of the node, Ω, argument of pericenter, ω, and mean anomaly, $\mathcal{M}$, are uniformly randomized within the ranges shown in Table 3.2. The inclination, I, is also randomized but with a Rayleigh distribution with mode $\sigma_{\mathrm{I}} = 1.8°$, consistent with the observed inclination distribution of exoplanets (Fabrycky et al., 2014). Each realization is integrated for 20 Myr with a timestep of 0.1 days. Collisions are allowed to occur in the simulations.

[24] In December 2017, an eighth planet was discovered in Kepler-90, Kepler-90 i, using deep machine learning (Shallue and Vanderburg, 2018)

Parameter	Distribution	Value range	σ
I	Rayleigh	$0° - 6°$	$1.8°$
ω, Ω, $\mathcal{M}$	Uniform	$0° - 360°$	$\cdots$
e	Uniform	$0 - 0.05$	$\cdots$

Table 3.2: Summary of randomized orbital elements of K11 analogues. Here, σ is the characteristic parameter of the corresponding probability distribution.

3.1.2 Planet-disk interaction: gaseous tidal damping

To explore the effects of eccentricity and inclination damping on the stability of STIPs, we produce 1000 random six-planet configurations. The systems were designed to be compact, more so than the observed typical mutual separation of neighboring exoplanets, i.e., $18-30\,R_{\rm mH}$ (Lissauer et al., 2014b), so that instability could be driven even in the gaseous disk, as complete circularization of planets in a system greatly increases the timescales for metastability. For example, many of the known multiplanet systems can exhibit instability on short timescales when their orbital elements are given small perturbations, but are stable on very long timescales if all the planets are given zero eccentricities (Fabrycky et al., 2014). The compact configurations used in this study seek to explore potential initial states of planetary systems during their formation in the presence of gas.

The masses, eccentricities, and inclinations for the planets in the synthetic systems are randomly drawn form a Rayleigh distribution with mode $\sigma_m = 2M_\oplus$ for the mass, $\sigma_{\rm I} = 1.8°$ for the inclination and $\sigma_{\rm e} = 0.025$ for the eccentricity (as shown in Table 3.3). The initial planetary masses are constrained to be in the range $0.1 \leq M_{\rm p}/M_\oplus \leq 8.0$; if a mass is either smaller or bigger than this range, the generating script redraws the mass until all six planets have been assigned a value. Fig. 3.2, shows the cumulative distribution of the resulting total planetary masses for the systems. If instabilities occur during the dynamical evolution of these systems in the disk, 90% of the systems have enough mass to form one critical core under the most ideal situations. However, in practice a much smaller fraction of systems could actually form critical cores through collisions because typically only two to a few planets are consolidated. Using more

Parameter	Distribution	Value range	σ
$M_{\rm p}$	Rayleigh	$0.1 - 8.0\,M_\oplus$	$2.0\ M_\oplus$
I	Rayleigh	$0° - 6°$	$1.8°$
ω, Ω, $\mathcal{M}$	Uniform	$0° - 360°$	$\cdots$
e	Rayleigh	$0 - 0.1$	0.025
$M_* = 1\,M_\odot$	$R_* = 1\,R_\odot$		

Table 3.3: Summary of orbital elements of synthetic STIPs. Here, σ is the characteristic parameter of the corresponding probability distribution.

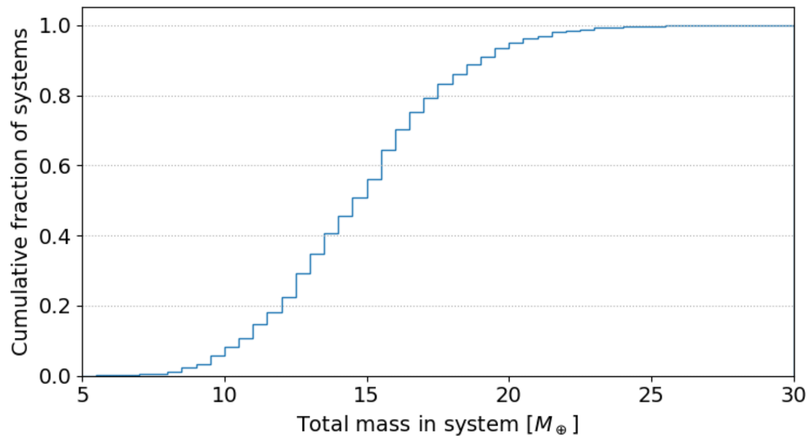

Figure 3.2: Cumulative total mass distribution in synthetic systems. From the synthetic STIPs generated, 90% have a total mass of $> 10M_\oplus$. The average total mass is $15 \pm 3M_\oplus$, and a small fraction of systems ($\sim$ 10%) having less than $10M_\oplus$ or more than 20 $M_\oplus$ in total. From this plot, at least 90% of the systems have enough mass to form one critical core under the most ideal situations.

massive systems is an area of future study. It should be noted that the K11 realizations have twice the mass of a typical synthetic system (Fig. 3.2). This was due in part because we were overly cautious about setting up near-critical cores in the initial conditions. As a consequence, we unfortunately cannot directly compare the critical core formation rate in K11 with this part of the study, which will instead be the focus of future work. The initial eccentricity and inclination distributions are based on results from the Kepler sample (Fabrycky et al., 2014). Once again, ω, Ω and $\mathcal{M}$ are uniformly randomized between 0° to 360°. The mass of the star is set to $M_* = 1M_\odot$.

Following the discussion in Sect. 2.1.2, the planet densities are estimated from their mass using Eq. 2.11, which uses the Valencia et al. (2006) power law ($\nu = 0.272$).

The compactness of the synthetic systems is determined by the free parameter $f = \Delta a/R_{\rm mH}$, which is the number of mutual Hill radii between the planets. The mutual Hill radius of a planet j and its inner neighbor, $j-1$, is given by

$$\begin{aligned} R_{mH}^{(j)} &= \frac{a_{j-1}+a_j}{2}\left(\frac{m_{j-1}+m_j}{3\,M_*}\right)^{1/3} \\ &= \frac{\Delta a_j + 2a_{j-1}}{2}\,K_j, \end{aligned} \tag{3.1}$$

where

$$K_j \equiv \left(\frac{m_j+m_{j-1}}{3M_*}\right)^{1/3}. \tag{3.2}$$

Here, M_* and m are the stellar and planetary masses, respectively, and $\Delta a_j = a_j - a_{j-1}$ is the difference of planetary semi-major axes. The semi-major axes are iteratively calculated from the allocated masses and a constant value of f, using the expression

$$a_j = a_{j-1}\left(\frac{2 + f\,K_j}{2 - f\,K_j}\right) \qquad \text{for } j > 1. \tag{3.3}$$

The innermost planet semi-major axis is always set to $a_0 = 0.09$ au.

In addition to the initial conditions of the planets, the gaseous disk must be parametrized. In Sect. 2.1.1, we described how the gaseous tidal damping is included in `IAS15` and that the strength of the damping depends of the local damping timescale (Eq. 2.5). We use that prescription here, such that

$$\tau_{\mathrm{local}}(\rho, z, \lambda, M_{\mathrm{p}}; t) = 0.078 \text{ days}\left(\frac{M_{\mathrm{p}}}{M_*}\right)^{-1}\left(\frac{\rho}{1 \text{ au}}\right)^{1.9} \mathrm{e}^{z^2/2H^2}\,\mathrm{e}^{t/\lambda}, \tag{3.4}$$

which is evaluated at each timestep, t, for a planet-to-star mass ratio M_{p}/M_*, and vertical and radial components, z and ρ. The only free parameter in Eq. 3.4 is the surface density decay timescale λ (recall the disk density and temperature profiles are fixed power laws for this study). In preliminary simulations, we used a $\lambda = 3$ Myr and a mutual Hill radius parameter $f = 9.5$. For these parameters, the gaseous disk can still affect the dynamics after 20 Myr. The corresponding simulations required ~ 30 days of computing time, in part because the tidal damping decreased the semi-major axis of the innermost planet, and in response, `IAS15` shortened the timestep to resolve the new orbit. To reduce the integration wall-clock time, we instead used $\lambda = 1$ Myr. With this timescale, the system is practically gas-free at 10 Myr. Qualitatively, the change of decay timescale does not affect the dynamics of the STIP. The preliminary simulations also showed that with a mutual Hill separation $f = 9.5$, the number of collisions was small. Therefore, we used $f = 5$ in the final suite of simulations to explore stability under more compact conditions. For reference, the mutual Hill spacings $f = 5$ and 9.5 are, respectively, about 1.5 and 3.0 times the separation threshold for the stability of planet pairs (Sect. 1.1.4), i.e., $f \approx 3.46$ (Gladman, 1993).

3.2 Gas-free outcomes.

In contrast to the nominal K11 system, which is stable for billions of years, the 1000 realizations become unstable after short timescales. Within 20 Myr, the resulting fraction of unstable realizations was 66.2%, producing consolidated masses between 5 and 17 $M_\oplus$. Most of the mergers involved the two innermost planets, K11b and K11c, consolidating into a mass of 5 $M_\oplus$.

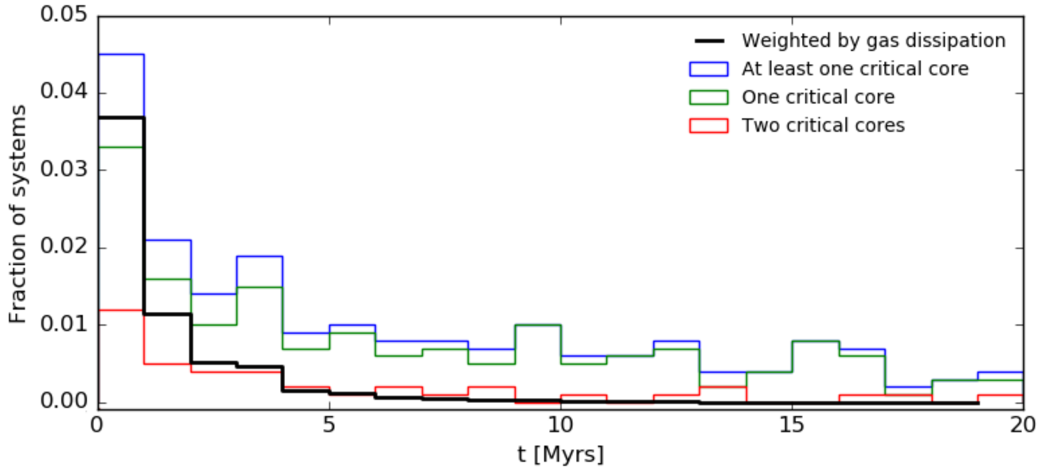

Figure 3.3: Fraction of critical cores per interval using K11 as a prototype STIP. The different colors indicate the number of critical cores produced during that time interval. In black, we show a proxy for gSPG formation after critical core consolidation. This is approximated by weighting each blue bin by $\exp(-t/2.5\ \mathrm{Myr})$, which is intended to capture the decay of the gaseous disk. Adapted from Boley et al. (2016).

In Fig. 3.3, we show the fraction of realizations that produced critical cores per time interval. In total, 20% of the realizations resulted in the consolidation of at least one critical core. The different histograms represent the number of critical cores in the indicated time interval. Two critical cores form from consolidation in some cases, but we concentrate here on the fraction of systems that produce at least one critical core (blue histogram in Fig. 3.3). The highest fraction per interval corresponds to the first million years and it decreases with increasing time.

In order to estimate whether the formation of a gSPG is possible after critical core consolidation, we introduce a gas disk mass decay timescale. With this in mind, we weight the core production per time interval with an exponential decay

$$\exp\left(-\frac{\bar{t}}{2.5\,\mathrm{Myr}}\right),$$

where $\bar{t}$ is the bin's midpoint. The proxy for gSPG formation is shown in black in Fig. 3.3. Cumulatively, 6.3% of gSPGs are generated within 10 Myr, with a minimal increase from 10 to 20 Myr.

3.2.1 Before moving through clouds: comparing the outcomes of Mercury6 and `IAS15`

The next stage of this study includes the implementation of gaseous tidal damping in `IAS15`. Before moving forward, we confirmed that Mercury6 and `IAS15` give consistent results when

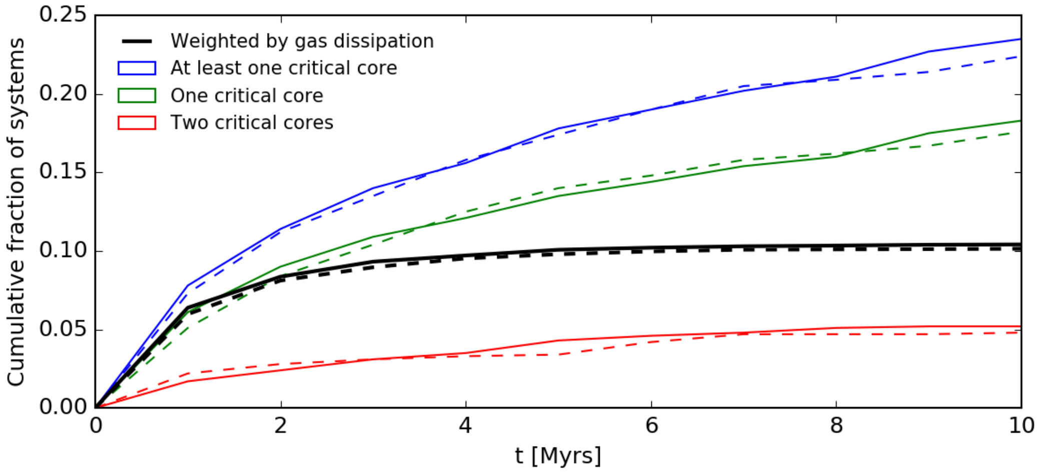

Figure 3.4: Comparison of critical core formation through consolidation between Mercury6 (dashed lines) and IAS15 (solid lines).

the simulations with identical initial conditions are run in the different codes without tidal damping. To this end, we ran a suite of 1000 simulations in Mercury6 and `IAS15`. The initial conditions are similar to those described in Sect. 3.1.1, but with an eccentricity distribution drawn from a Rayleigh distribution with $\sigma_{\mathrm{e}} = 0.025$.

Each simulation was run for 10 Myr. As before, the fraction of unstable K11 analogues is high. Using Mercury6, we found 80.2% of the systems to be unstable during the integration period, compared with 79.8% using `IAS15`. These unstable systems generated a range of planetary masses through consolidation. Most of these unstable realizations originated from the consolidation of planetary masses $M_{\mathrm{p}} < 10\,M_{\oplus}$. Furthermore, of the total population, 22.4% and 23.5% produced at least one critical core in Mercury6 and `IAS15`, respectively. The results of this comparison are shown in Fig. 3.4 and Table 3.4.

The dynamical outcomes of both N-body integrators are consistent. The differences could be due to numerical chaos or to the timestep management and collision detection algorithms. For example, identical simulations can diverge if the timestep, which would normally sample the orbit of a single planet well, is too large to properly sample the dynamical interactions between multiple planets (Dones et al., 2018; Lissauer, 2018). We note that the `IAS15` integrator iterates

	Mercury6 (%)	`IAS15` (%)
Unstable systems	80.2	79.8
At least one critical core produced	22.4	23.5
Two critical cores produced	4.8	5.3

Table 3.4: Summary of results comparing outcomes of Mercury6 and `IAS15`.

on the solution for each step, and may better capture some of these dynamics. Regardless of the small differences, we found there to be reasonable agreement between Mercury6 and `IAS15`.

3.3 Outcomes with tidal damping

Gaseous tidal damping stabilized our synthetic systems, even though they were compact. The resulting unstable fraction is small and depends on the parameter values for the initial conditions. A summary is shown in Table 3.5. No critical cores were produced and the consolidated masses ranged from 0.64 to 7 $M_\oplus$, well below the critical core threshold. For the decay timescale $\lambda = 3.0$ Myr and Hill mutual spacing $f = 9.5$, we only found 2 unstable realizations out of 465. A limited number (31) of realization were run with $\lambda = 1$ Myr and $f = 9.5$, of which none went unstable within 10 Myr. Only a few tens of realizations were run because we noticed that the change of λ does not modify the overall behavior of the systems; it only changes the evolution timescale. This effect is due to the tidal damping timescale being much shorter than the gas dissipation timescale, as planets are damping within a few thousand years, depending on the

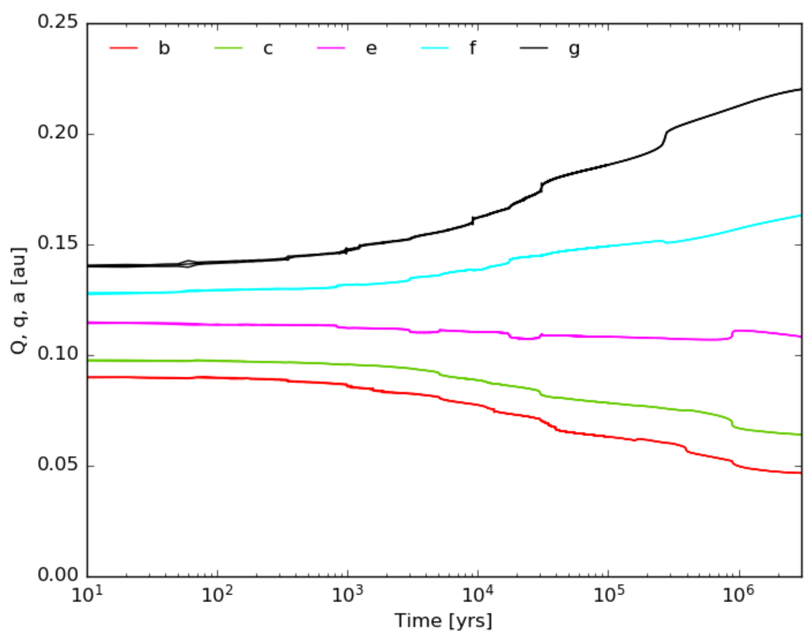

Figure 3.5: Example of the dynamical evolution of a synthetic STIP embedded in a gaseous disk. The semi-major axis, a, pericenter, q, and apocenter, Q, vs. time are shown for each planet (delineated by color). Because the planets typically have very low eccentricities, the a, q and Q curves appear as one thick curve for most times. In general, the systems spread in semi-major axis, with the inner planets moving to lower a and the outer planets moving to higher a. The jumps in semi-major axis correspond to the location of first-order MMRs. In this plot, $f = 5.0$ and one of the planets is not shown for reasons that will be discussed in Sect. 3.4.

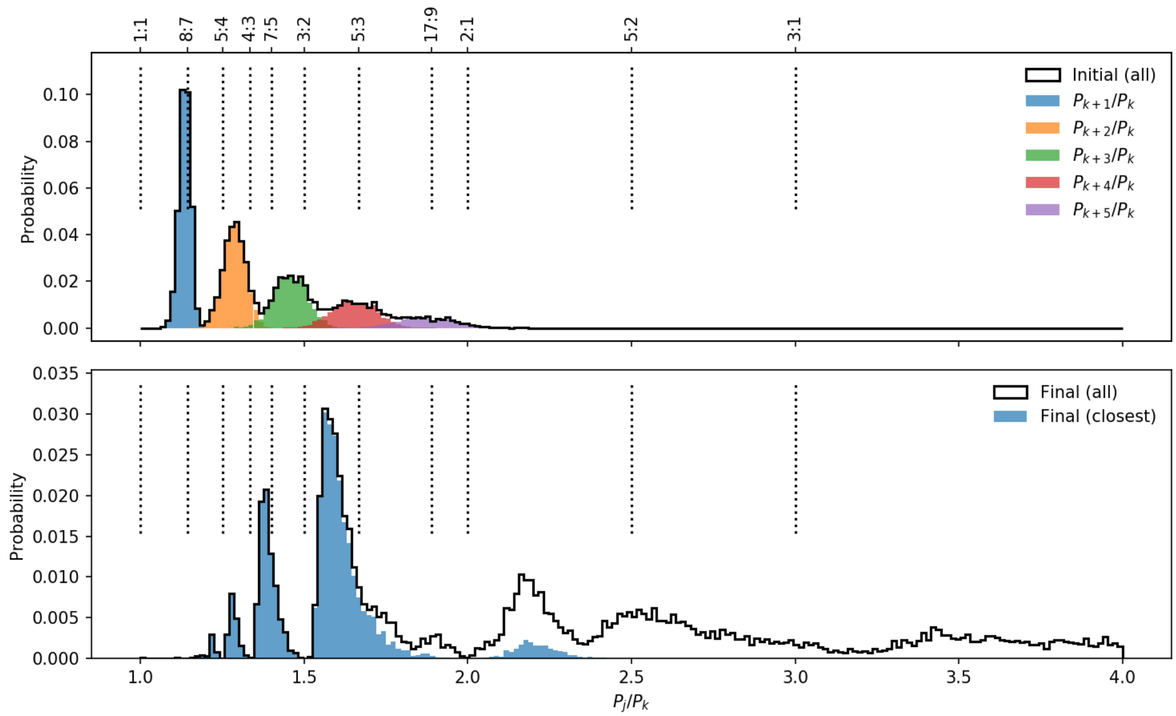

Figure 3.6: Distribution of all possible combinations of period ratios for systems with $f = 5.0$. The vertical dotted-lines indicate the location of MMRs. The initial (top) and final (bottom) distribution are displayed in black. *Top:* the colored filled histograms represent different initial closeness ratios, i.e., the closest neighbor is denoted as P_{k+1}/P_k, while the third closest as P_{k+3}/P_k, et cetera. The width of these peaks is due to the initial planetary mass distribution chosen. *Bottom:* the period ratio of the closest planets (in blue) at the end of simulation show that the planets cluster between MMRs. This clustering is different from that seen in the initial conditions, the planets spread significantly from their initial configurations.

actual gas density. However, the gas damping timescale increases with decreasing gas density, allowing planet-planet interactions to have stronger perturbations. This increases the rate that the planetary spacing diffuses due to excitation followed by gaseous damping. In the last set, with $\lambda = 1$ Myr and $f = 5.0$, the number of unstable systems was the highest with 45/1000. We attribute this to the reduced Hill separation.

The general dynamical behavior of the synthetic systems is highlighted in Fig. 3.5[25]. The plot shows the semi-major axis, a, pericenter, q, and apocenter, Q, for the planets in a synthetic system as a function of time. The planetary semi-major axes slowly spread out, as a consequence of having their eccentricities damped. Jumps in evolution also occur over $\Delta t < 1 \times 10^4$ yr whenever planets cross first-order MMRs.

In Fig. 3.6 and 3.7, we compare the initial and final period ratio distributions of the synthetic

[25]We highlight that, even though only five planets are shown, the system is stable. For reasons that will become evident in Sect. 3.4, we neglected a planet in this plot. Regardless, the figure illustrates the general behavior of the systems well.

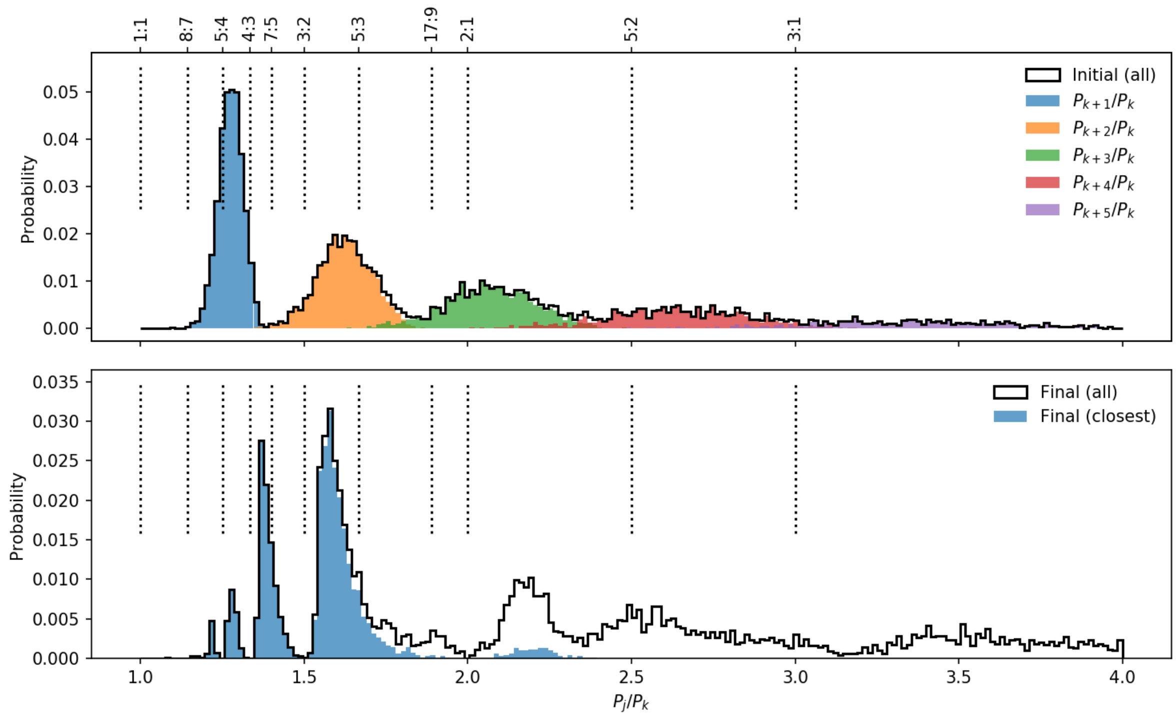

Figure 3.7: Distribution of all possible combinations of period ratios for systems with $f = 9.5$. The same notation and colors used in Fig. 3.6 are used here. Both, initial and final period ratio distributions are similar to those in Fig. 3.6, except the initial distribution extends to larger period ratios due to the value of f.

systems. All possible unique planet combinations are considered. The planet period ratio is color coded by the proximity of the pairs. For example, adjacent pairs are denoted $k+1$, pairs separated by one planet are denoted $k+2$, etc. The chosen Hill radius spacing causes the periods to be grouped into distinct peaks, with widths ultimately reflecting the mass distribution. For $f = 5.0$, the period ratio of the closest neighbor peaks near the 8:7 MMR in the initial conditions, while, for $f = 9.5$, this occurs near the 5:4 MMR. This initial period ratio distribution close to an MMR is a fortuitous result of the chosen initial mutual spacing and mass distribution. By construction the initial period ratio distributions are different between systems with $f = 5.0$ and $f = 9.5$, the latter being spread to higher values.

The final period ratio distribution indicates that the planets avoid the first-order MMRs. This is due to an eccentricity kick followed by gaseous tidal damping whenever the planet is near one of these commensurabilities. The combined effect is to cause a small change in the semi-major axis, and subsequently remove the planet from the MMR. The excursions into first-order MMRs are short-lived and the width of the excursion is wider for the 2:1 MMR and narrower for the 8:7. This behavior is present in the final distributions of $f = 5.0$ and $f = 9.5$ systems. The similarity between the final period distributions for the $f = 5.0$ and $f = 9.5$ simulations leads us to suggest that in presence of a gaseous disk, the initial planet distribution is unimportant. This

λ (Myr)	f ($R_{\rm mH}$)	$\bar{t}_{\rm uns}$ (yrs)	$N_{\rm sim}$	$N_{\rm uns}$	$M > 10M_\oplus$	Effective integration time (Myr)
3	9.5	1600, 30000	465	2	No	0.8-2.2
1	9.5	$\cdots$	31	0	No	10.0
1	5.0	200	1000	45	No	2.37-6.21

Table 3.5: Summary of gaseous tidal evolution results. The mean instability time, $\bar{t}_{\rm uns}$, is on the 3rd column. The 4th and 5th columns are the total number of run and unstable realizations, respectively, in a given set. Ideally, each suite would have the same number of realizations and integrated the same number of e-folding time relative to λ. The first and third set were run in the Orcinus computing cluster (provided by WestGrid and Compute Canada Calcul Canada).

mechanism might be a byproduct of the assumptions made for the disk, although the combined effects of dynamical excitation followed by gaseous dissipation should be general. Interestingly, the 5:2 MMR appears to have a local maximum (although this is not a distinct peak).

From Table 3.5, it can be seen that the number of realizations and the effective integration time is different between the simulations suites (e.g., those with different λs and fs). Ideally, each suite would have the same number of realizations and would be integrated for the same number of e-folding times (relative to λ). However, due to the computing resources involved, we focused on $\lambda = 1$ Myr and $f = 5.0$ suite because it evolved faster and captured the essential behavior.

3.3.1 Stability test after complete gas dissipation.

We finally explore the stability of the final configurations of the synthetic systems in the simulations with gaseous tidal damping. First, we use the orbital elements at the end of each simulation for the $f = 9.5$, $\lambda = 1$ Myr suite. We used this suite for three reasons: (1) systems with $f = 5.0$ and $f = 9.5$ have similar end states, with a two-peak mutual spacing distribution at $f = 14$ and 17.2, the latter being the highest peak (see Fig. 3.8); (2) all the realizations in this suite were evolved for the same amount of time (10 Myr) and none became unstable; and (3) this suite has a more tractable number of simulations. We integrate the final configurations for 100 Myr using Mercury6. Due to the small eccentricities and inclinations, none of the realizations went unstable within 100 Myr. This means that the gas removal does not affect the eccentricity and inclination of the planets.

Next, we repeated the experiment, but assigned each planet in each system a random eccentricity and inclination drawn from a Rayleigh distribution with mode $\sigma_{\rm e} = 0.01$ and $\sigma_{\rm I} = 1.8°$, respectively. After 100 Myr, 12 of the 31 realizations became unstable, from which 50% of the remaining planets have an eccentricity $e > 0.018$, with a maximum of $e = 0.1$.

The results of these tests seem to suggest that: (1) the final configurations are stable if both

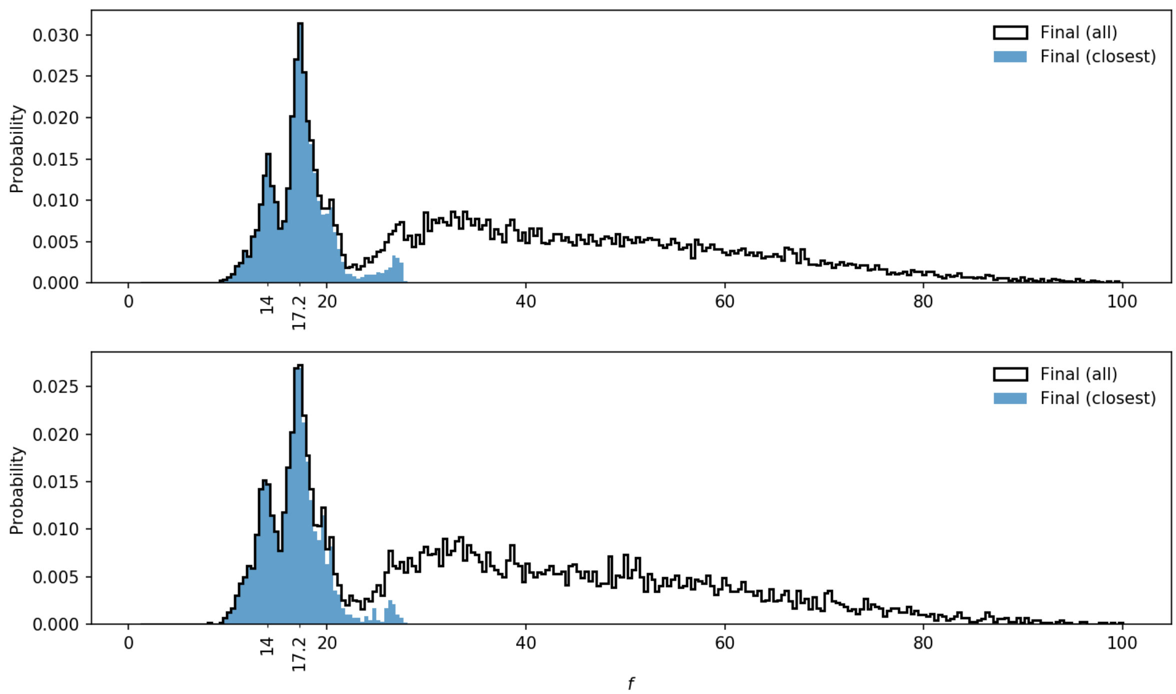

Figure 3.8: Final mutual Hill spacing distribution, f, for systems with initial separations $f = 5.0$ (top panel) and $f = 9.5$ (bottom panel). The black line shows all possible combinations of mutual Hill spacings within a system, while the blue highlight shows only the separations between adjacent planets. The end states of both sets of simulations peak at mutual Hill separations of $f = 14.0$ and 17.2, particularly if only the nearest neighbor is considered. The separation between planets within a system, as shown in black, can span up to 100 mutual Hill spacing.

inclination and eccentricity are close to zero; and (2) the instabilities can still occur if there is a mechanism that can perturb e and i among the planets, either within the gaseous disk or after its dispersal.

We should point out that only gaseous damping is considered in this work. The physics of a planet interacting with the surrounding disk is rich, and there are mechanisms that compete with the gaseous tidal damping that can excite the planetary eccentricity and inclination. Benítez-Llambay et al. (2015) and Eklund and Masset (2017) showed that as a planet heats up due to planetesimal accretion, it re-radiates the thermal energy and changes the local conditions of the disk, which prevents the inward migration of the planet. This mechanism can also excite the eccentricity and inclination of the planet.

3.3.2 Very compact STIPs in the presence of gas.

Two additional sets, with 200 realizations each, were run to further test the instability of very compact STIPs in the presence of gas. We used the same disk properties, planetary mass

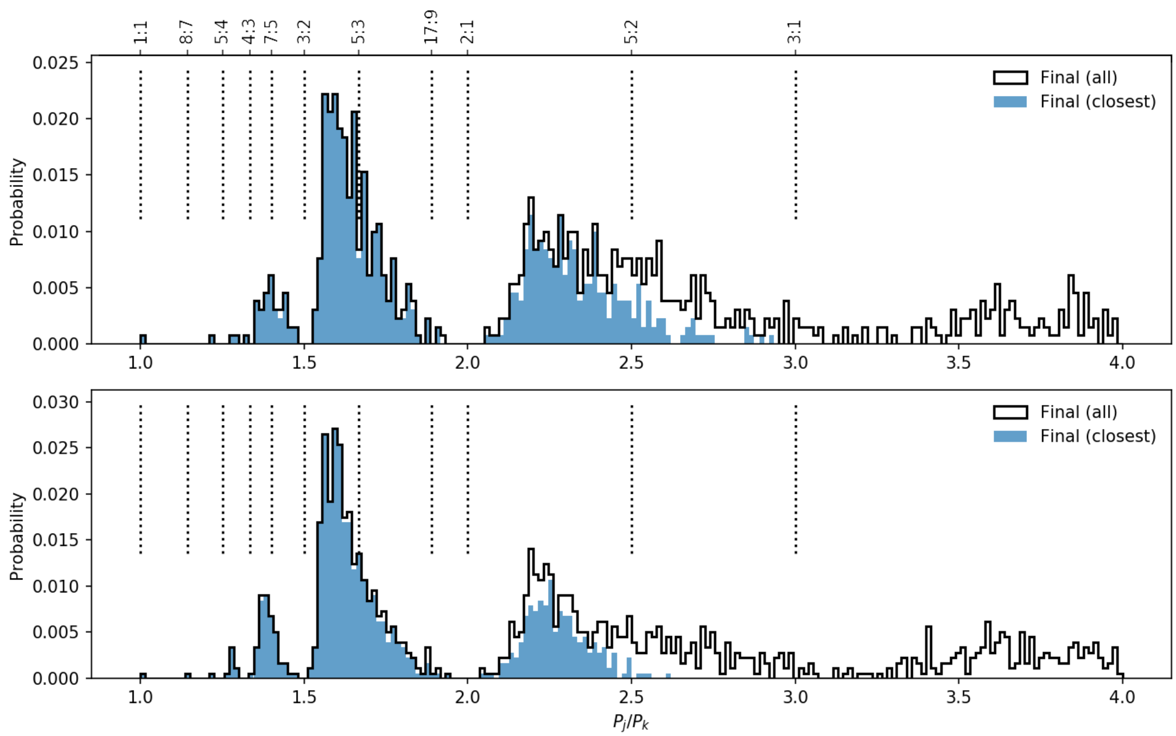

Figure 3.9: Final distribution of period ratios for systems with initial $f = 1.5$ (top panel) and $f = 3.0$ (bottom panel). Similarly to Fig. 3.8, the black line indicates all possible combinations of period ratios within a system, while in blue only the nearest neighbors were considered. The period ratio distribution from these simulations also shows an avoidance of the first-order MMRs (as in Fig. 3.6 and 3.7) and the main peak (between the 3:2 and 5:3 MMRs) is still present but with a broader width towards the 2:1 MMR. The period ratios shorter than 1.5 are not as populated as in the $f = 5.0$ and $f = 9.5$. Also, there is a populated region between the 2:1 and 5:2 MMRs, absent in Fig. 3.6 and 3.7.

distribution and integration time as that used in the $f = 5.0$ experiment, but with initial mutual spacings of $f = 1.5$ and 3.0, respectively. Due to the initial compactness of these systems, the instability and subsequent consolidations were more efficient than in the other mutual separation experiments. The instability occurred early in the evolution of the systems, usually within a couple of years and occasionally after a few thousand years. The fraction of unstable systems in the $f = 1.5$ and $f = 3.0$ sets were 96% and 86%, respectively. These extremely unstable and compact systems, unlike the more widely spaced realizations, produced consolidated masses $M_{\rm p} \geq 10 M_{\oplus}$. In the $f = 1.5$ set, 13% of the realizations produced at least one critical core, and even a smaller fraction of systems (2.5%) consolidated two critical cores. On the other hand, in the $f = 3.0$ set only 1.5% of the systems formed only one critical core. While the setup is itself ad hoc, it does allow us to further explore instabilities in the presence of gas and how such instabilities might shape, for example, the period distribution.

The final period ratio distribution of these sets have a similar distribution to Fig. 3.6 and 3.7. As shown in Fig. 3.9, the remaining planets avoid the first-order MMRs and have a very

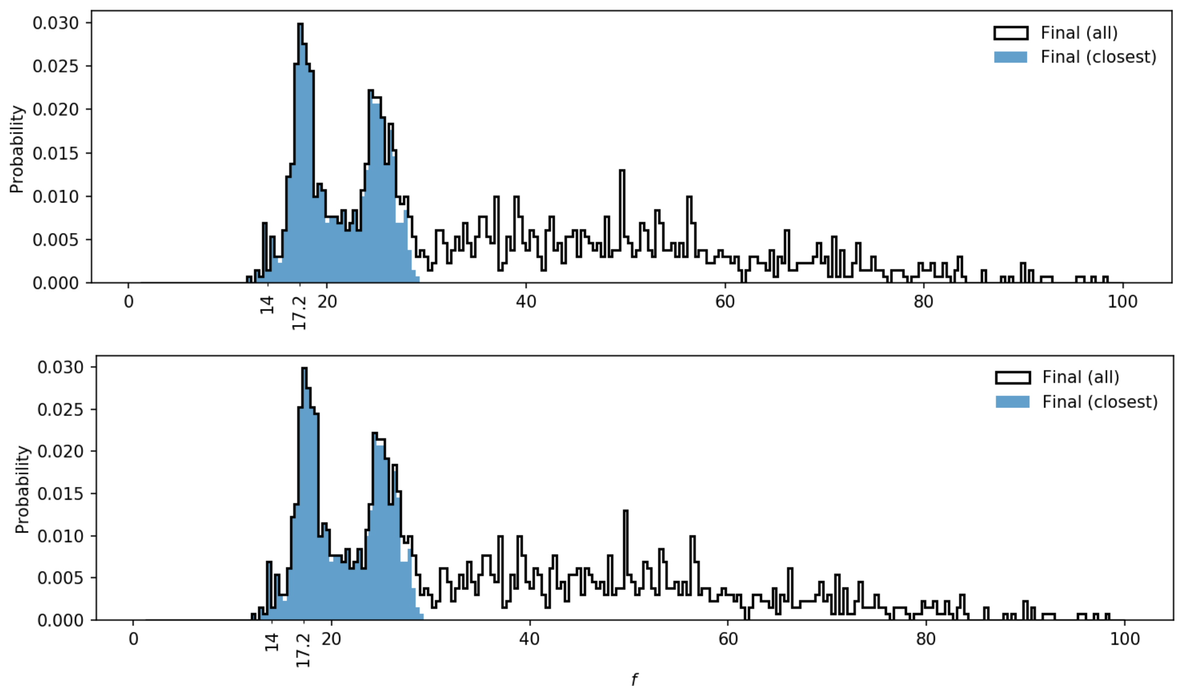

Figure 3.10: Final mutual Hill spacing distribution, f, for systems with initial separations $f = 1.5$ (top panel) and $f = 3.0$ (bottom panel). The same notation and colors used in Fig. 3.8 are used here. Compared to Fig. 3.8, the peak at $f = 14$ is not significant in the distribution. Instead, a feature at $f = 25$ has emerged almost as prominent as the peak at $f = 17.2$.

significant peak between the 3:2 and 5:3 MMRs. The main difference is that due to the initial mutual spacing, which causes strong instabilities, the peaks between first-order MMRs shorter than 3:2 are not as populated as in the $f = 5$ or $f = 9.5$. This indicates that the planets that consolidated were preferentially those with period ratios shorter than 1.5. The surviving planets then evolved like the more relaxed configurations.

The final mutual spacing distributions of both sets, shown in Fig. 3.10, look very similar among them and also have similarities with those correspondent to $f = 5.0$ and $f = 9.5$ sets. The principal peak is still located at $f = 17.2$, but the peak at $f = 14.0$ has almost disappeared. Instead, a peak at $f \approx 25$ has emerged in both $f = 1.5$ and $f = 3.0$ initial mutual spacing distributions. This new peak is almost as significant as the $f = 17.2$ peak in the $f = 1.5$ final distribution. The $f = 25$ peak seems to indicate the high instability occurrence in these sets and the subsequent clearing of some of the closest neighboring planets in the early evolution of the systems. In many of the simulations, the planets that collide are those with intermediate semi-major axes, which results in the survival of the planets of the more distant planets. As the planets are tidally damped by the gas, their mutual spacing also increases. This new feature is a consequence of both instability and tidal damping.

3.4 Coorbital planets and their detection

While we did not observe the formation of critical cores through the consolidation of planets in the $\lambda = 1$ Myr and $f = 5.0$ simulation suite, we did find 23 realizations in which planets evolved into crossing orbits but did not collide. In most of those cases, only one orbit was crossed, but in three realizations, a planet crossed the orbit of another two planets. In one particular case, the second innermost became the outermost planet within 10 years (about 200 orbits), crossing the orbits of four planets. Although such sudden instability at the start of the simulation reflects very unstable initial conditions, the resulting dynamics are of potential interest, as highlighted here.

In two of the simulations, neighboring planets apparently became locked in a 1:1 resonance during orbit crossing. The evolution of the semi-major axes of the planets in two realizations, noted as r-054 and r-628, are shown in Fig. 3.11. This behavior suggest that either the least massive planet was captured as a satellite/binary planet or the planets did indeed enter a 1:1 coorbital resonance.

We looked at the offset angle between the planets near the 1:1 MMR (Fig. 3.12), as well as their orbits in a frame corotating with the most massive planet of the pair (Fig. A.1)[26], to determine the nature of the interaction. The offset angle of a satellite orbiting a planet has a maximum angle that is equal to the ratio of the satellite-planet and the planet-star distances[27] ($\simeq 0.15°$ in Earth-Moon case). In contrast, coorbital planets are identified by their libration near the Lagrange points, and can be either in a tadpole or horseshoe configuration. The offset angle between coorbital planets is associated with three of the equilibrium points of the restricted three body problem, i.e., $\phi = \pm 60°$ (marked in green in Fig. 3.12 and A.1) and $\phi = 180°$ for the Lagrange points L4, L5 and L3, respectively. If in a tadpole orbit, the offset angle librates close to either L4 or L5. On the other hand, if a planet is in a horseshoe orbit, the planet encloses L4, L5 and L3, which means that the libration is centered at 180° and the amplitude of libration $\Delta\phi < 180°$.

As shown in Fig. 3.12 (bottom panels), in both of the simulations, the smaller planet becomes trapped in the 1:1 MMR after about 75 years. The offset angle between the planets first librates as a tadpole orbit, followed by changes in and out of a horseshoe orbit as the planets migrate inward (Fig. 3.11(a)) or outward (Fig. 3.11(b)). For r-054, this only last 3% of the total integration time, after which the 0.25 $M_\oplus$ planet breaks out of the resonance and migrates to a smaller orbital distance. In the case of r-628, the coorbital configuration changes from a tadpole

[26] Fig. 3.12 succinctly shows the dynamics of the coorbital realizations. The face-on plot of the corotating frame represents the spatial evolution of these realizations, and for completeness, the corresponding plot is included in Appendix A.3.

[27] The offset angle in this case is calculated from $\tan\phi_{\max} = \phi_{\max} \approx a_m/a_p$, where a_m is the semi-major axis of the satellite in the planet's reference frame and a_p is the planetary semi-major axis respect to the star. Here, we used the small-angle approximation.

(a) r-054

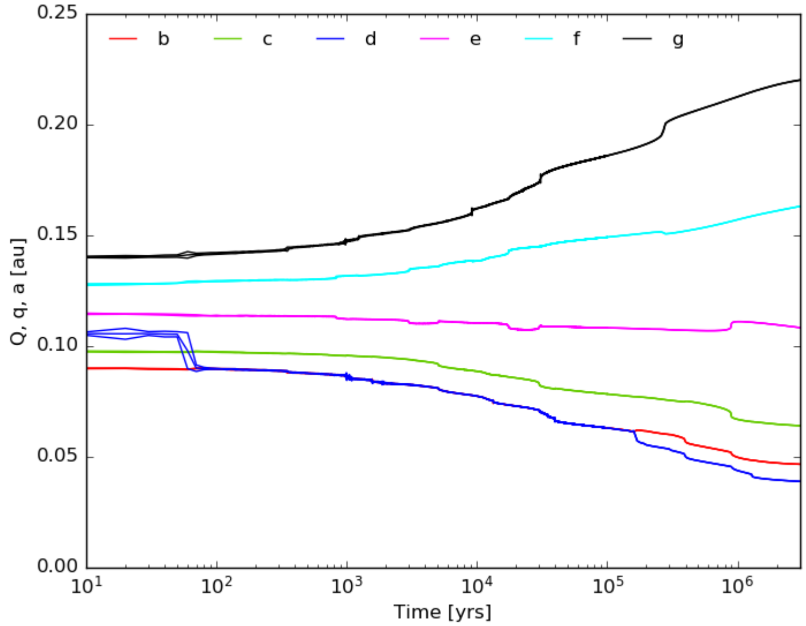

(b) r-628

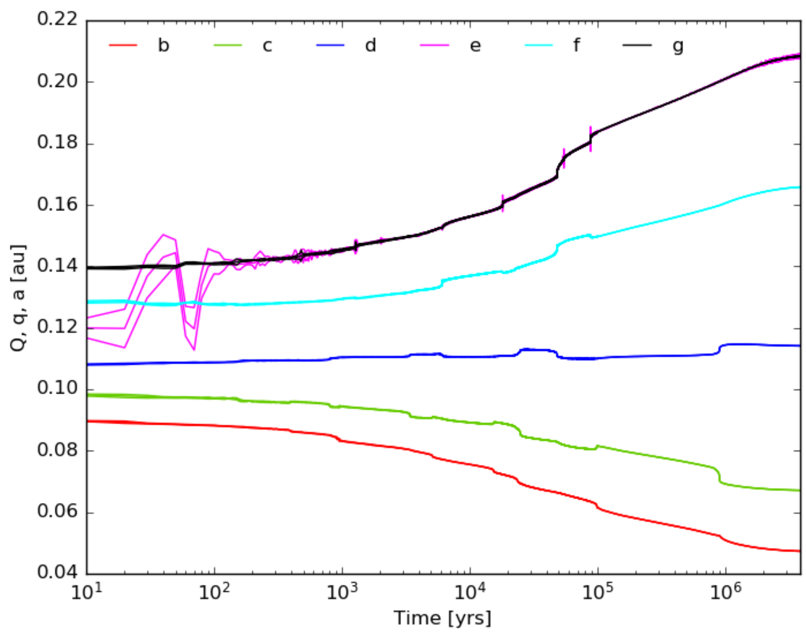

Figure 3.11: Semi-major axes, a, pericenter, q, and apocenter, Q, as a function of time for two realizations with planet orbit crossings. Each system is identified by its run number. In both realizations, there is a planet that within the first million years crosses the orbits of another two planets, and is then captured into a 1:1 MMR with either (a) the innermost or (b) outermost planet.

(a) r-054 (b) r-628

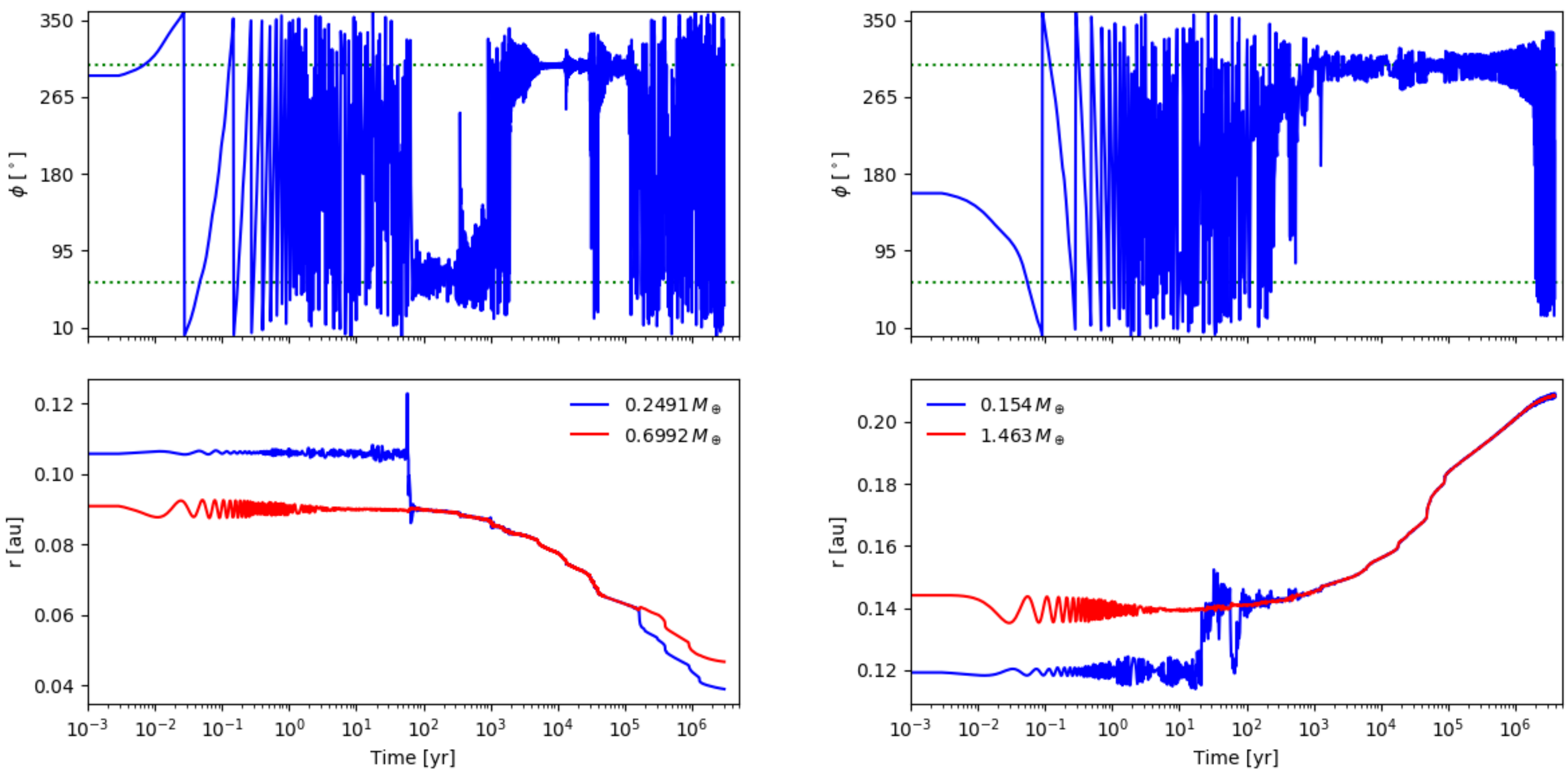

Figure 3.12: Offset angle, ϕ, between the planets near the 1:1 MMR (top) and a detailed radial evolution as a function of time (bottom). The first column represents r-054 and the second r-628. The planetary masses are displayed in the legend. The offset of the L4 ($\phi = 60^\circ$) and L5 Lagrange ($\phi = 300^\circ$) points are indicated with a green horizontal dotted-line. (a) In this realization the smaller planet is trapped in a coorbital configuration for about 1000 years, after which it breaks free from the resonance due to the gaseous tidal damping. For the system in panel (b), in contrast, the smaller planet is captured into the 1:1 MMR by the first hundred years, starting in a tadpole orbit which then evolves to a horseshoe orbit until the end of the simulation.

to a horseshoe orbit at 1 Myr and remains in this configuration until the end of the integration.

Because the integration with gas is limited in time, we further test the stability of r-628 by taking the final orbital elements and integrating them forward for 10 Myr using Mercury6, assuming the gaseous disk has dissipated. We run two different versions of this final state. In the first one, all the orbital elements are used at face value, which implies co-planarity and near circular orbits. For the other, the eccentricity and inclination of each planet in the system are slightly perturbed using a Rayleigh distribution with a mode of 0.01 and 1.8°, respectively.

Only the excited system becomes unstable. Within the first 250 kyr, the coorbital planets break the 1:1 MMR and the least massive planet collides with one of the inner planets. The planetary eccentricities for the unperturbed and perturbed simulations are shown in Table 3.6. The planets e and g, those in the 1:1 MMR, have an increased eccentricity of about 2 orders of magnitude in the perturbed case. These results suggest that if a coorbital configuration forms from a dissipative interaction with the gaseous disk, it can be long-lived should other additional perturbations be absent. Long timescale stability studies for equal-mass planets in the 1:1 MMR, with $e_1 = e_2 = 0.01$, found that the mass threshold for horseshoe configurations is $\mu = 2m_{\rm p}/(m_{\rm p} + m_*) < 4 \times 10^{-4}$ for long-lived pairs (Laughlin and Chambers, 2002). This suggests that the coorbital pair, with $\mu \approx 5 \times 10^{-6}$ in r-628, will be stable for longer than 10 Myr. The eccentricities of the coorbital planets in our perturbed case are a factor of 2 higher than Laughlin and Chambers (2002) study, but they only considered the two coorbital planets in their simulations. It is likely that the presence of the other four planets in our simulations have a big impact on the stability of the perturbed realization.

Fig. 3.13 shows the semi-major axis of each coorbital planet as a function of time for 100 years of integration of simulation r-628. In the horseshoe orbit, energy is exchanged periodically between the two planets, which causes the semi-major axes and the orbital periods to vary

Planet	a (au)	$e_{\rm u}$	$e_{\rm p}$
b	0.04732	7.3×10^{-5}	1.7×10^{-2}
c	0.06713	7.6×10^{-5}	6.5×10^{-4}
d	0.11410	8.9×10^{-5}	1.0×10^{-2}
e	0.20910	2.2×10^{-4}	1.6×10^{-2}
f	0.16577	1.5×10^{-4}	7.2×10^{-3}
g	0.20825	2.4×10^{-4}	2.4×10^{-2}

Table 3.6: Eccentricity of planets in r-628. Here, $e_{\rm text}$, represents the eccentricity values of the unperturbed system, where the initial conditions where taken directly from the final state of the tidally damped simulations. $e_{\rm p}$, on the other hand, are the values for the perturbed system, drawn from a Rayleigh distribution with $\sigma_{\rm e} = 0.01$.

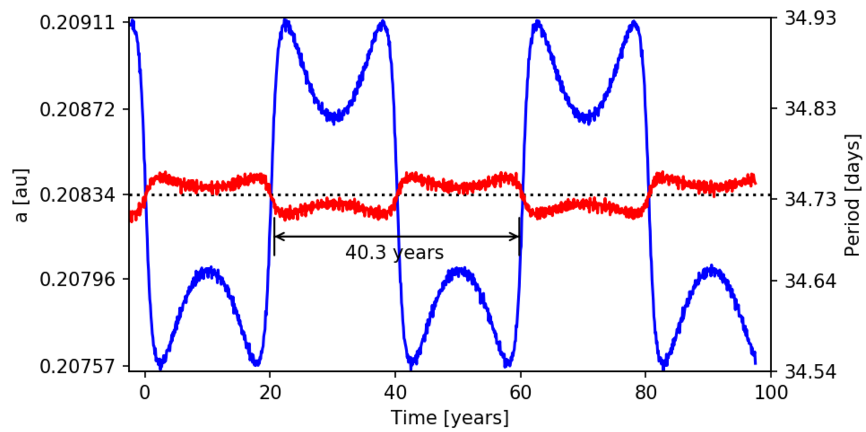

Figure 3.13: Semi-major axes of coorbital planets as a function of time. This realization was run for 100 years, and it shows that the semi-major axis of each planet varies periodically in a well-constrained range. An additional horseshoe period of 40.3 years is present (indicated with arrows).

with time. This orbital period has two components: the azimuthal period[28] and a radial, P_r, horseshoe period. In this case, the horseshoe period is $P_r = 40.3$ years, 421 times longer than the azimuthal component. The mean azimuthal period for the planets is $P = 34.733$ days, about which the more massive planet varies $\Delta P_{\rm l} = \pm 0.028$ days and the less massive planet with $\Delta P_{\rm s} = \pm 0.198$ days. The functional form for the radial period of tadpole planets is known (Laughlin and Chambers, 2002), which is a function of the planets-to-star mass ratio and the Keplerian orbital period. That relation, however, does not strictly apply for horseshoe orbits. Our simulations suggest that the radial period of a horseshoe orbit is ≈ 2.5 times longer than that of a tadpole.

The 1:1 corotational MMR can provide additional information about the planets, other than just the orbital periods. If the difference between the semi-major axes, $s = a_2 - a_1$, is measured at two different times, i, j, and the corresponding offset angle, ϕ, can be inferred, then the planetary masses can be determined using the following relations (Murray and Dermott, 2000):

$$\left(\frac{s_i}{a}\right)^2 - \left(\frac{s_j}{a}\right)^2 = -\frac{4}{3}\frac{m_1 + m_2}{m_{\rm c}}\left[\mathrm{H}(\phi_i) - \mathrm{H}(\phi_j)\right], \tag{3.5}$$

$$m_1 W_1 = m_2 W_2, \tag{3.6}$$

and

$$\mathrm{H}(\phi) \equiv \left(\sin\frac{\phi}{2}\right)^{-1} - 2\cos\phi - 2. \tag{3.7}$$

Here, a is the semi-major axis of the Keplerian orbit; $m_{\rm c}$, m_1, and m_2 are the masses of the star and planets, respectively, such that $0 < m_2 < m_1$ and $m_{\rm c} \gg m_1, m_2$; and W is the average

[28] This is the period that either of the two planets would have on a circular orbit at $a = 0.2083$ au.

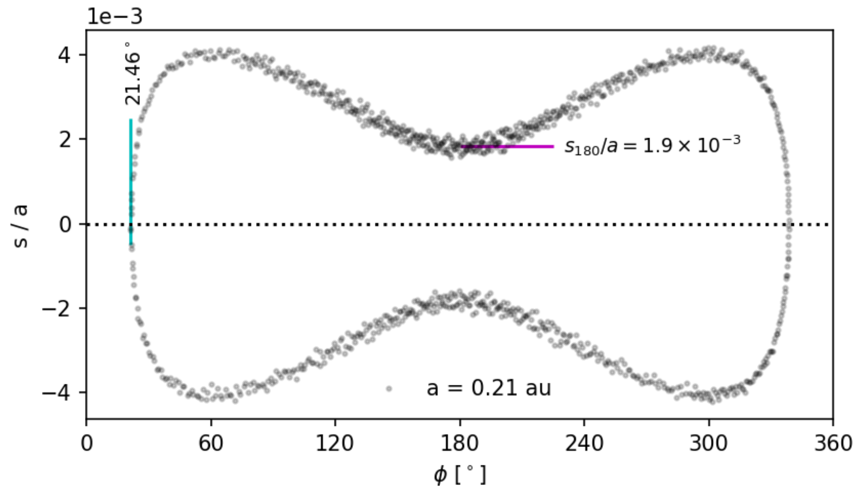

Figure 3.14: Normalized deviation from a Keplerian orbit, $s/a = (a_l - a_s)/a$, as a function of offset angle, ϕ, for r-628. The shape of this plot is typical for horseshoe orbits, which highlights the orbital evolution (100 years) of both coorbital planets and provides information such as s_{180} and $\phi_{\rm min}$ (magenta and green lines, respectively) needed to infer orbital properties. The mean semi-major axis of the planets is $a = 0.21$ au, as indicated.

length of the arc, i.e., the angular spread in the corotating mean frame of each planet's orbit when observed for a prolonged time. Eq. 3.5 can be simplified to

$$\left(\frac{s_{180}}{a}\right)^2 = \frac{4}{3}\frac{m_1 + m_2}{m_{\rm c}}\left[{\rm H}(\phi_{\rm min}) - 1\right], \tag{3.8}$$

where s_{180} is the difference in semi-major axes of the two planets when separated by $\phi = 180°$, and $\phi_{\rm min}$ is the minimum phase difference between the planets. For r-628, we show in Fig. 3.14 the semi-major axis deviation from a Keplerian orbit for the two coorbital planets as a function of their offset angle. Using Eqs. 3.8 and 3.7, and the values $s_{180}/a = (1.852 \pm 0.133) \times 10^{-3}$ and ${\rm H}(\phi_{\rm min} = 21.46°) = 1.509$, we estimate a total planetary mass $m_1 + m_2 = (1.005 \pm 0.141) \times 10^{25}$ kg $= 1.68 \pm 0.24\, M_\oplus$, which agrees with the known total mass, i.e., $1.617 M_\oplus$. The uncertainty in the total mass calculation comes from the uncertainty in the measurement of s_{180} within $170° \leq \phi \leq 190°$. Should coorbital planets exist and be detected, their densities could be estimated with a single observation method, in the same spirit as using TTVs (Agol et al., 2005).

Similar coorbital configurations have been found in studies of planetary systems embedded in dissipative gaseous disks (Beaugé et al., 2007; Cresswell and Nelson, 2006, 2008). Currently, it is uncertain whether coorbital planets exist, but their detection can provide a constraint on primordial formation mechanisms. For this reason, several detection methods have been proposed based on TTVs (Schwarz et al., 2015; Ford and Holman, 2007; Vokrouhlický and Nesvorný, 2014; Haghighipour et al., 2013), transits (Janson, 2013; Hippke and Angerhausen, 2015) and RV (Ford and Gaudi, 2006; Leleu et al., 2015). Using some of these techniques, several archival surveys have been carried out (Lillo-Box et al., 2018; Hippke and Angerhausen, 2015; Janson, 2013; Ford and Holman, 2007; Madhusudhan and Winn, 2009), with no coorbital planets detected.

Upon reviewing detection methods for coorbital planets, we realized there is not an explicit representation of a horseshoe transit lightcurve, only ones for tadpole orbits (Hippke and Angerhausen, 2015). For this reason, and to further efforts to detect trojan planets, we tested the feasibility of detecting the coorbital pair in a horseshoe configuration with the transit method. We produce observational transit lightcurves from N-body simulations and then put those curves through the Kepler Transit Planet Search pipeline (TPS) to determine whether coorbital planets could be detected with current transit detection methods.

For producing the transit lightcurves, we ran a short N-body simulation that mimicked Kepler's long cadence observations by integrating for 4 years and using an output of 30 minutes. The initial conditions were those used in the stability test of the coplanar, circular r-628 simulation (see above). Synthetic lightcurves were then produced from the position vectors of both coorbital planets by choosing an arbitrary line of sight aligned with the mean orbital plane and reducing the normalized flux each time one of the planets crossed the projected surface of the star. The radii of the planets, $R_\mathrm{l} = 1.11\,R_\oplus$ and $R_\mathrm{s} = 0.6\,R_\oplus$, were obtained from the mass-radius relationship in Eq. 2.9 and $\nu = 0.272$, while the stellar size was set to $1R_\odot$. In this approach, stellar limb darkening was neglected while producing the transit shape. To make the lightcurve more realistic, we included a Gaussian random noise of $\sigma = 5 \times 10^{-6}$. One important variant to consider is the initial time of integration, which observationally, corresponds to observing epochs, as a particular lightcurve will be produced for different starting times due to the changing relative positions of the planets.

We synthesized three different transit lightcurves (Fig. 3.15), each showing distinct behavior depending on the relative location of the planets when the integration begins. On the left side of Fig. 3.15, we show the orbital period of each planet (top) and the relative period as a function of time. The colored regions represent the different times during which lightcurves are produced. In the blue region, the planets just had their closest approach and the relative period has a change in direction, which yields a lightcurve with transits for the two planets that first decreases in relative phase and then increases. We call this signature non-linear behavior. In orange, the relative period changes linearly, which is shown in the middle lightcurve. On the third lightcurve, highlighted in green on the left panels, the relative timing of the transits seems to be constant with time, which occurs when the planets are 180° apart.

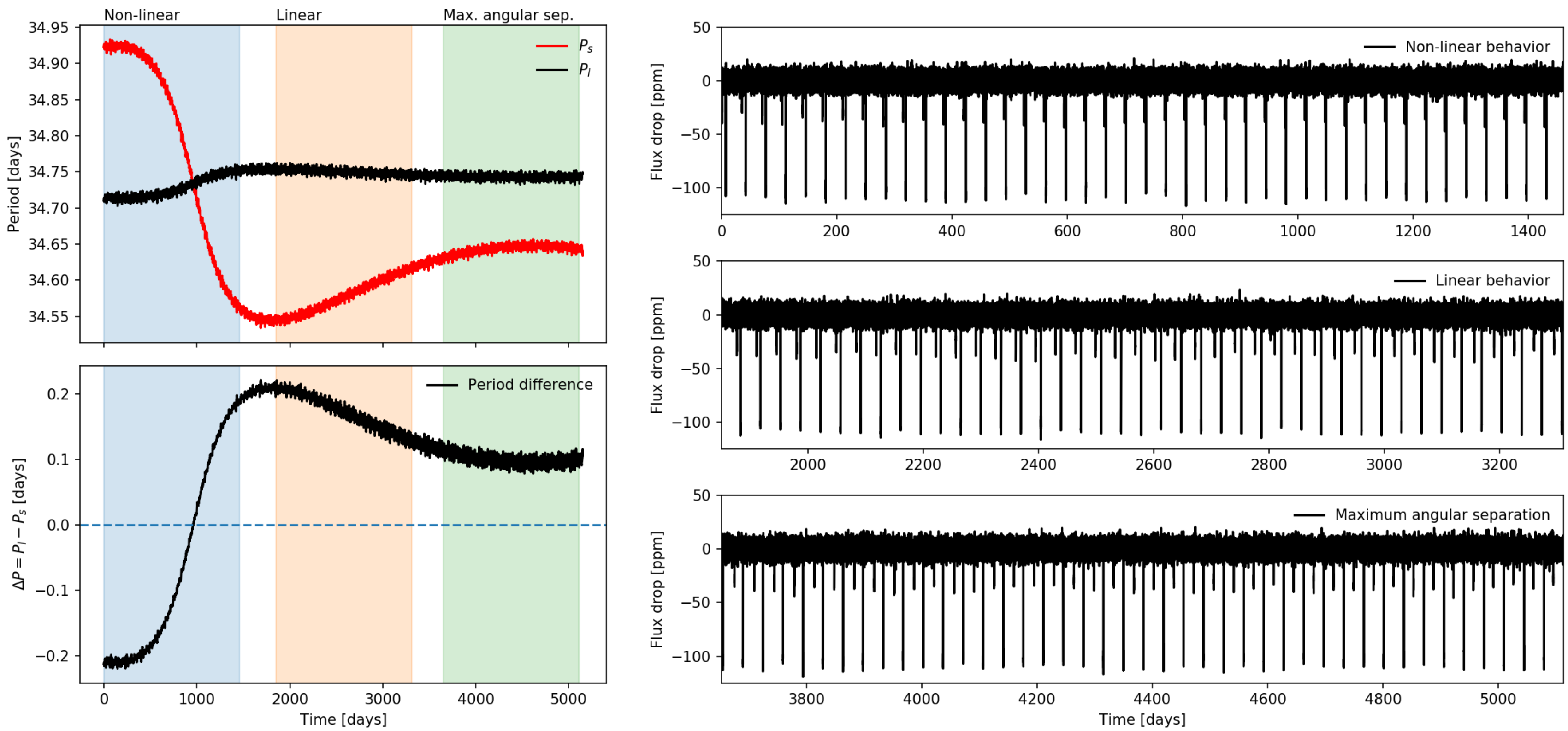

Figure 3.15: Transit lightcurves of a coorbital pair in a horseshoe orbit at two different epochs (left), and corresponding period change as a function of time (right). The color highlights in the left panels identify each of the lightcurves on the right. Here, P_l and P_s are the orbital period of the large and small planet, respectively. We show that there is a linear and non-linear change of periodicity of the smaller planet, which correspond to the orange and blue highlighting on the left, respectively. The third lightcurve (green highlight) corresponds to an offset angle between the two planets of about 180°.

The synthetic linear and non-linear transit lightcurves were then given to collaborator Michelle Kunimoto to run through the TPS. In both cases, the pipeline easily recovered the larger planet, in part because the flux drop $R_\mathrm{p}/R_* = 0.01$ is well above Kepler's detection limit of 30 ppm for solar type stars (Gilliland et al., 2011). For this planet, the pipeline recovered a period $P_\mathrm{l} = 34.8$ days in both lightcurves. Using the standard pipeline, the smaller planet ($R_\mathrm{p}/R_* = 5\times10^{-3}$) was not recovered from the lightcurves. However, the planet's period could be recovered upon forcing the pipeline to look for a signal that is within 10% of the larger planet's period. In this case, the TPS could retrieve the second planet, with an observed period of $P_\mathrm{s} = 34.6$ days, but only for the linear lightcurve. The smaller planet evaded detection in the non-linear case.

A common way to determine the transit profiles, amplitudes and period variations is to phase-fold the lightcurve. Folding a time series, like a lightcurve, involves identifying a periodic signal and the corresponding period, P_0; then the phase is calculated by dividing the time series by P_0, such as $\psi = (t - t_0)/P_0$, where t_0 is the center of the first transit. At this point the phase varies from 0 to a given integer number of the period. The folding is finalized when the phase is normalized to a range $-0.5 \leq \psi \leq 0.5$. With this phase-folding, the first transit in the data is centered at a phase 0, and the following transits should align on top if P_0 represents the real period of the data. In the case of small deviations from exact periodicity, the feature at phase 0 looks smeared or shifted from the center. Although the period of both coorbital planets changes with time, the relative period variation of the larger planet is shorter than that of the smaller planet. Therefore the transit lightcurve can be folded using the period of the larger planet ($P_\mathrm{l} = 34.8$ days). By phase-folding the lightcurves with P_l, the transit of the smaller planet will appear smeared, showing an arc (see Fig. 3.16). In the folded lightcurve, the larger planet is the reference and the phase difference behaves much like observing the corotating reference frame in phase values rather than relative positions. A phase difference provides a direct estimation of the angular separation between the two planets, related by $\phi = 360^\circ\,\psi$. This is why, that even if the second planet cannot be detected, the transit signatures of the larger planet in the folded lightcurve could still provide additional information about the system. For example, the dispersion in the transit signature could constrain W and ϕ (Eqs. 3.6 and 3.7).

Fig. 3.16 shows the folded lightcurve for the three epochs, corresponding to the non-linear, linear and maximum separation regimes. In the non-linear case, when the planets go from a larger to a smaller semi-major axis, or vice versa, the transit of the larger planet is broadened and the extent of the arc of the smaller planet is relatively small. Roughly, from this lightcurve, we can estimate $m_\mathrm{l}/m_\mathrm{s} \approx 8.5$ and $\phi \approx 19^\circ$ by measuring the lengths of the arcs in the phase plot and by taking the difference of the left edge of the deeper transit to the right edge of the shallower dip. In the linear case, at phase of zero, there is no smearing and the length of the second transit is larger than in the previous case. The mass fraction could also be obtained from this lightcurve. On the last lightcurve, when the planets are separated by 180°, the important

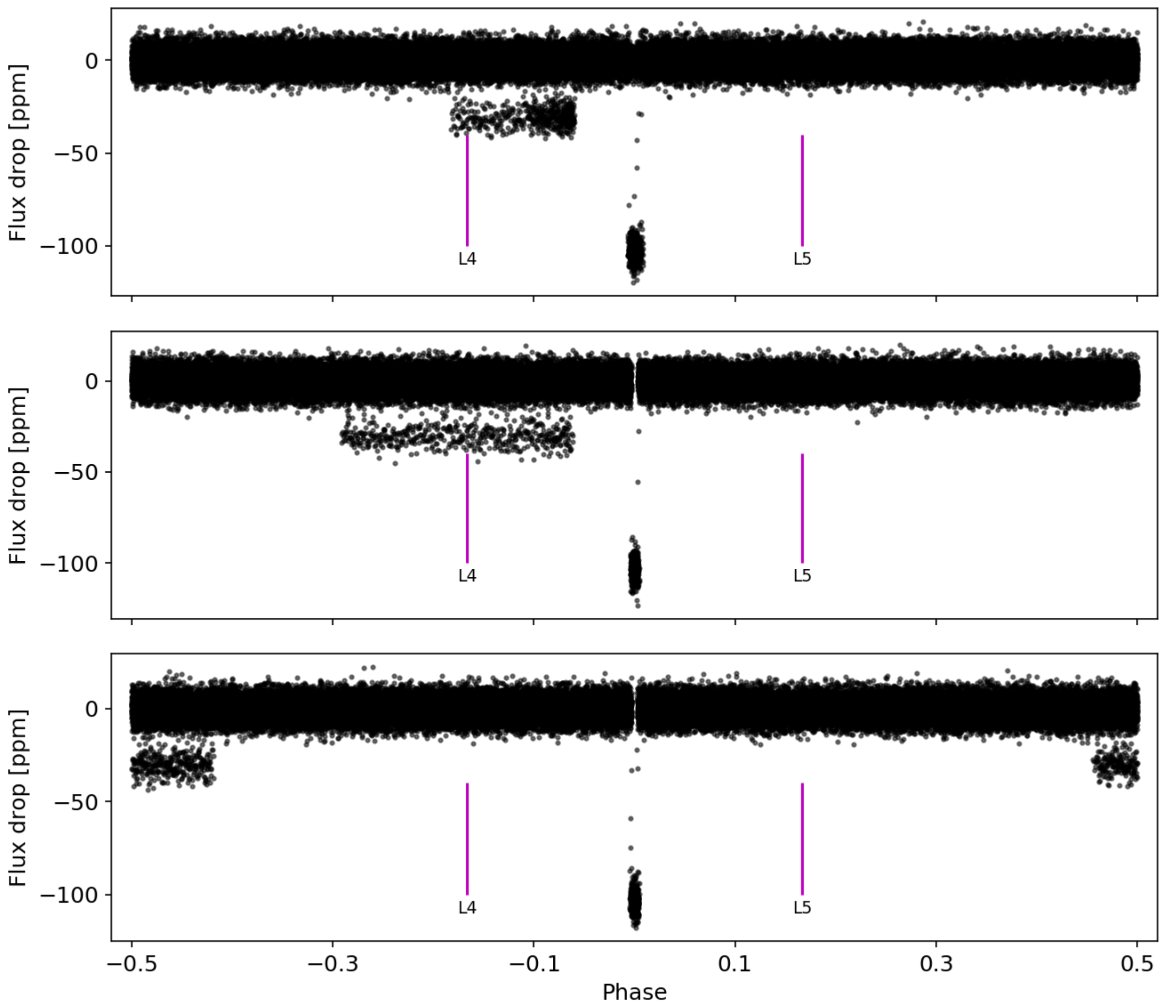

Figure 3.16: The non-linear, linear and maximum angular separation lightcurves from Fig. 3.15, but phase folded to the period of the larger planet. The smaller planet produces the shallow transit arcs. The position of the arcs depend on the relative angular separation between the two planets in the corotating frame. The length of the arcs, and particularly the ratio between them, provides information on the mass ratio of the two planets (Eq. 3.7). From the non-linear lightcurve (at the top), in principle, we can also obtain the minimum angular separation of the planets. The locations of L4 and L5 for the given period are shown for reference.

parameter to estimate would be s_{180}/a. It may be possible to relate this parameter to the observed period, but this connection has not yet been explored here.

These preliminary tests show that the transit method is promising for detecting coorbital planets and should be explored further in future work. This could include, for example, using systems that produce a more realistic signal-to-noise value, provided the synthetic systems are within the stability limit $\mu = (m_1 + m_2)/m_c < 4 \times 10^{-4}$ (Laughlin and Chambers, 2002). In principle, we could use planets 100 times more massive for the coorbital configuration than those explored here. Updating the present transit lightcurve pipeline to search within 10% of a just found period will improve the likelihood of recovering a coorbiting planet. Furthermore, if two planets in a coorbital configuration are large enough to produce a transit above the survey observational limit, and these are coplanar as well, they will produce a transit lightcurve with characteristics similar to those in Fig. 3.15. The phase folded lightcurve could be used to find m_2/m_1 and μ, but a relationship between s_{180} and P is still needed.

Chapter 4

STIPs and external planetary perturbers: effects on observability and stability.

Due to the selection effects of the different planet detection techniques, it is uncertain whether outer companions exist in the observed STIPs, particularly between semi-major axes of 5 and 10 au (or $1000 < P < 1 \times 10^4$ d). In other words, STIPs could be the inner region of a more complex planetary system, with an outer system perhaps similar to the outer Solar System. Because the dynamics of a planet is not only affected by the host star, but also by the gravitational interactions with other planets in the system, deviations from expected orbits of known planets could reveal the presence of additional unknown planets. As an example, Neptune's existence was predicted mathematically by John Adams and Urbain Le Verrier due to the discrepancy between the predicted and the observed position of Uranus. Observations went on to confirm the predictions. Nowadays, due to the increase in computing power, we can make use of numerical simulations to explore a wide range of possibilities and to investigate the dynamics of planetary systems more generally.

In this chapter, we investigate the observability and stability of STIPs in the presence of a planetary outer perturber by using direct numerical integration along with secular theory. We present case studies of two systems that have high multiplicity ($N_{\rm p} > 5$), namely Kepler-11 (K11) and Kepler-90 (K90)[29] (Lissauer et al., 2014b; Cabrera et al., 2014; Schmitt et al., 2014). For each system, we first examine the planetary dynamical behavior using just the known planets, and then that of the known planets with an additional perturbing Jupiter-like planet. When the perturber is included, it is placed exterior to the last known planet in each system, initially at 5.2 au. The location of the Jupiter analogue respect to the STIP is expected to modify the secular frequencies of the system, to explore a broader range of secular interactions we "migrate" the planet inwards in our numerical simulations. Looking at the dynamical evolution of the STIPs with a migrating perturber, we identify the perturber location that might be affecting the inner system through secular resonances, reflected in instability of the inner system or selective inclination changes on the inner planets. Both instability and selective

[29] K90 is also known as KIC 11442793 and KOI-351.

inclination changes affect the observability of STIPs, the former reduces the total multiplicity and the latter can strongly affect the number of detectable transiting planets in a system (depending on the inclination change), both explainable by the existence of unknown planet companions. We verify the secular interaction, by following up each tentative configuration, i.e., STIP plus perturber location, with analytical and synthetic secular theory, as laid out in Sect. 2.2 and 2.3.

The work presented in this chapter has been published as Granados Contreras and Boley (2018). The original article has been adapted to the structure of this thesis, with a few modifications and additions. In particular, the methodology is described in Sections 2.2 throughout 2.3. In addition, we include the phases of the synthetic secular theory instead of the sole precession spectra.

4.1 STIPs studied and simulations setup.

The values used for K11 are those used in Sect. 3.1.1 (Table 3.1). The only difference is that we use $M_{\rm p} = 20.0\,M_{\oplus}$ for K11g, instead of $8.0\,M_{\oplus}$, because this value is closer to the upper mass limit found dynamically by Lissauer et al. (2013) and in this way the system resembles K90 by having the outermost planet as the most massive in the STIP. The other system, K90 (Lissauer et al., 2014b; Cabrera et al., 2014; Schmitt et al., 2014), has seven planets orbiting an $M_* = 1.2 \pm 0.1\,M_{\odot}$ star. K90 (along with TRAPPIST-1) has the largest number of confirmed planets thus far, making it one of the closest in planet multiplicity to the Solar System. However, unlike the Solar System, all of K90's known planets are confined within 1 au. The masses of K90's planets have not been measured directly, and as a result, the masses used here are estimated from the mass-radius relation described by Wright et al. (2011), which is based on the size distribution reported by Lissauer et al. (2011b). Table 4.1 summarizes the measured or estimated properties for K90. The values in Tables 3.1 and 4.1 are adopted for the present study, unless otherwise noted.

Published eccentricities and inclinations are used when available; for the K90 planets the orbital eccentricities are set to zero ($e = 0$). The inclination values given in Table 3.1 and 4.1 are relative to a reference plane that was determined by averaging the published orbital inclinations relative to a perpendicular to the system's line of sight, which is $\langle i_{\rm K11} \rangle = 89.52°$ and $\langle i_{\rm K90} \rangle = 89.68°$. We create 100 realizations of each system, in which the longitudes and anomalies (Ω, ϖ and $\mathcal{M}$) for each planet are drawn from a uniform random distribution between 0 and 2π. These realizations are first run without the external perturber to establish the stability of the systems over 10 Myr. We further test the stability of K11 and K90 in the presence of a Jupiter analogue and run the same initial conditions with an additional planet, also for 10 Myrs. The results of these simulations are discussed in detail in Sect. 4.2. Unless otherwise noted, the perturber has a mass $M_{\mathrm{p}} = 1\,M_{\mathrm{J}}$ and initial orbital elements $a_{\mathrm{p}} = 5.2$ au, $e_{\mathrm{p}} = 0.05$, $i_{\mathrm{p}} = 1.3°$, $\omega_{\mathrm{p}} = 273.8°$, $\Omega_{\mathrm{p}} = 100.5°$ and $\mathcal{M}_{\mathrm{p}} = 93.8°$, where the subindex P denotes parameters for the perturber. The realizations that include the perturber will be denoted as K11+ and K90+ throughout this chapter.

The stability of the STIP is expected to be sensitive to the semi-major axis of the perturber (due to the secular frequencies), and as such, we systematically explore the semi-major axis parameter space of the perturber by forcing it to migrate inwards. The simulations that include the inward migration of the perturber are performed using the initial conditions that resulted in stable configurations for K11+ and K90+ after 10 Myrs. For K11+ we used the full set of stable realizations, but chose only one of the K90+ stable systems. This choice was based on the analysis of the K11+ simulations, which all showed consistent behavior.

N-body integrations were run using a modified version of the `Mercury6` code (Chambers, 1999), which includes a general relativity correction as described in Sect. 2.1.1, which is appropriate for low-eccentricity orbits (Nobili and Roxburgh, 1986). Because we want to resolve close encounters should they occur, we use the hybrid integrator of `Mercury6`. When in MVS mode, the time step is set to 10^{-2} of the initial period of the innermost planet. Again, the total integration time, if not otherwise stated, is 10 Myrs.

The inward migration of the Jupiter analogue is achieved by applying an acceleration term to

Planet	P (days)	R_{p} ($R_\oplus$)	M_{p} ($M_\oplus$)	a (au)	I (°)
b	7.0082 ± 0.000019	1.31 ± 0.17	2.4	0.076	0.28
c	8.7193 ± 0.000027	1.19 ± 0.14	1.7	0.088	0.00
d	59.7367 ± 0.00038	2.87 ± 0.3	7.9	0.307	0.03
e	91.9391 ± 0.00073	2.66 ± 0.29	6.9	0.424	0.11
f	124.9144 ± 0.00190	2.88 ± 0.52	8.1	0.520	0.09
g	210.6069 ± 0.00043	8.10 ± 0.8	69.1	0.736	0.12
h	331.6006 ± 0.00037	11.30 ± 1.0	297.9	0.996	0.08
$M_* = 1.2 \pm 0.1\,M_\odot$	$R_* = 1.2 \pm 0.1\,R_\odot$				

Table 4.1: Nominal orbital elements of the known planets of Kepler-90 (K90) (Lissauer et al., 2014b; Cabrera et al., 2014; Schmitt et al., 2014). The uncertainties provided by Cabrera et al. (2014) for the orbital periods and planetary sizes are the 1σ error of their transit model optimization for each planet and their stellar parameter estimation from synthetic spectra fitting. Compared to Table 3.1, this table is missing the columns for e and ω because these orbital elements have not been estimated from observations.

the planet of the form

$$\mathbf{a}_{\rm mig} = -\frac{2\pi}{\tau_{\rm mig}}\left(\frac{1{\rm au}}{a}\right)[3(\hat{\mathbf{r}}\cdot\dot{\mathbf{r}})\hat{\mathbf{r}} + (\mathbf{r}\times\dot{\mathbf{r}})\times\hat{\mathbf{r}}]$$
$$= -\frac{2\pi}{\tau_{\rm mig}}\left(\frac{1{\rm au}}{a}\right)[2\,(\hat{\mathbf{r}}\cdot\dot{\mathbf{r}})\,\hat{\mathbf{r}} + \dot{\mathbf{r}}]\,, \tag{4.1}$$

where $\mathbf{r}$ is the perturber's position vector from the star, $\dot{\mathbf{r}}$ its velocity vector, a its semi-major axis, and $\tau_{\rm mig}$ is the timescale for migration at 1 au. Over the region of interest, migration is nearly constant. For these simulations, we set $\tau_{\rm mig} = 30$ Myr[30], which is equivalent to $\dot{a} \approx 0.42$ au Myr^{-1}. During the 10 Myr migration, the orbital precession of the perturber increases by 1 to 2 orders of magnitude. The perturber's eccentricity also changes, decreasing among the stable systems from 0.05 to 0.035 at $a_{\rm J} = 3$ au and to 0.02 at $a_{\rm J} = 1$ au, corresponding to $t = 6$ and 10 Myrs, respectively.

We complement the numerical simulations with secular theory as laid out by Murray and Dermott (2000) and described in Sect. 2.2. For systems in which the planets have small e and i, the theory can identify locations at which a test particle would be in an eccentricity or inclination secular resonance, although higher-order methods (e.g., Laskar, 1985, 1986) or direct N-body calculations are needed to determine the dynamical effects of a given resonance. As mentioned in Sect. 2.2.1, if planets have strong interactions, such as might be expected near mean motion resonances (MMRs), then additional frequencies can become important and/or the predicted frequencies can become shifted with respect to the second-order theory. Because K11 and K90 exhibit TTVs, we expect deviations from second-order theory, as is the case in the Solar System with Jupiter and Saturn (Brouwer and van Woerkom, 1950). Nevertheless, such effects are excluded in our calculations. We also exclude the effects of GR on the secular frequencies. Regardless, as will be shown, secular theory seems to identify the locations of resonances with reasonable accuracy.

Using a given system configuration (e.g., the current STIP and perturber's orbital elements) and the secular code, we highlight the resonant structure in the system. First, we calculate the forced eccentricities and inclinations. Resonances will correspond to distances at which the forced eccentricity or inclination show very large increases, resulting from a singularity introduced when a precession frequency matches a system eigenfrequency. Using this approach, we can compare the resonant structure from secular theory with the behavior of the N-body simulations. For example, if a given planet becomes orbit crossing or develops large inclination variations, we build the secular theory for the system, but exclude the highly perturbed planet(s). As shown below, in K90(+), the two innermost planets are the most easily excited, so we examine the resonance structure by removing these planets from the secular theory, allowing us to see if the forced eccentricity and inclination at their semi-major axes suggest a resonance, at least for a

[30]It will be shown that this migration timescale is about 800 times longer than the longest secular timescale in either K11 or K90 without the perturber.

test particle. This is only reasonable whenever the removed planets have low masses compared with the other planets. K90b and K90c are tightly coupled, so this must be done with some caution. Nevertheless, as we will show, this approach is reasonable enough to be useful for the present situation. As with K90(+), we examine the secular resonant structure in K11(+) by removing K11b, which is often the first planet to become orbit crossing, or by removing both K11b and K11c due to their coupling.

We also calculate synthetic frequency spectra for select realizations of K11(+) and K90(+) to further explore the secular dynamics of the systems and to examine the effects of strong planet interactions. This is done by rerunning a given simulation for 0.3 Myr with output every 60 years. The synthetic secular spectrum provides the principal apsidal and nodal precession frequencies and amplitudes.

4.2 Unperturbed vs. perturbed STIPs: dynamical outcomes

The N-body simulations of K11 and K90 (without the perturber) allow us to examine the dynamical stability of these systems generally and to provide a point of comparison for the simulations with the Jovian perturber. We find that the stability of K11 is very sensitive to perturbations to the nominal argument of pericenter for non-zero eccentricities. In particular, 44% of the simulations become unstable using the nominal eccentricities, but random longitudes. This is qualitatively consistent with Mahajan and Wu (2014), who found that K11 is preferentially unstable if any of the eccentricities $e > 0.04$, using the same planetary masses used here. In contrast, 100% of the realizations in this study are stable if the initial eccentricities are zero, which agrees with the zero-eccentricity stability tests of Lissauer et al. (2011a, 2013). For K90, 20% of the our realizations present instability despite having initial orbital eccentricities set to zero for all planets. This result is unexpected at face value, as we might anticipate the system to be stable (as with K11) under such conditions. This agrees with the stability test presented in K90's discovery paper (Cabrera et al., 2014). The system's secular perturbations could be the origin of the noted instability and/or mean motion resonances, as will be discussed later.

The simulations of K11 and K90 are now used as a reference for exploring additional dynamical perturbations. Using the same realizations for K11 and K90, we now include a Jupiter analogue in each system, the stability of the STIPs is not affected by the presence of the single perturber when it is placed at 5.2 au. The same 44% and 20% analogues become unstable in less than 10 Myrs for K11+ and K90+, respectively, which suggests that the inner system instability is not affected, at least for this short time period and for the initial placement of the Jupiter analogue.

While the stability of the STIPs is unaffected, the systems do respond to the presence of the outer perturber. This is highlighted in Figures 4.1 and 4.2, which show the inclination evolution

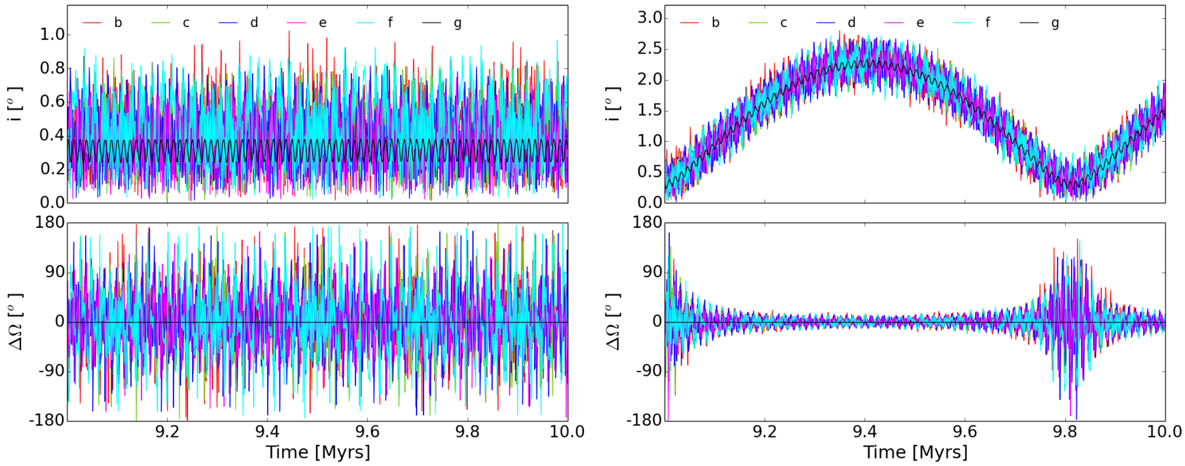

Figure 4.1: Evolution of the orbital parameters of a stable K11 analogue (left) and K11+ (right) system. The top panel shows the inclinations for all of the nominal planets in the system, while the bottom panel shows the longitude of ascending node relative to K11g, the outermost planet.

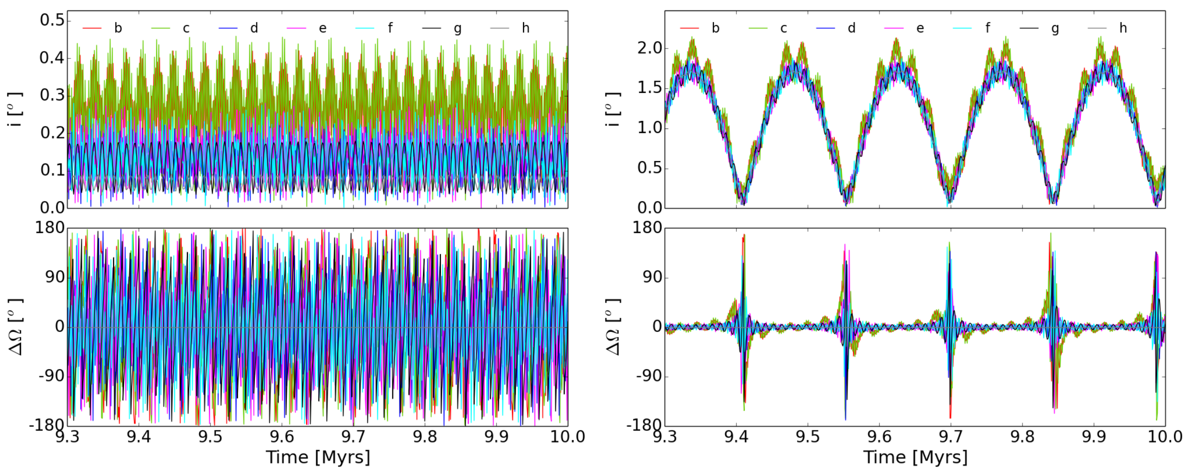

Figure 4.2: The same orbital parameters in Figure 4.1 are shown for K90 (left) and K90+ (right). Dynamical rigidity is also observed in this system, i.e., all the longitudes of ascending node precess at the same rate. K90b and c (magenta and blue lines) are more tightly coupled to each other than to the rest of the planets.

for the planets in stable realizations of K11 and K90, respectively, with and without the presence of the Jupiter analogue. In each case, the planets exhibit variation among their inclinations with time. However, when the perturber is included there is an additional large-scale variation in all of the orbital inclinations, i.e., each planet's inclination oscillates with respect to a common orbital plane, while the orientation of the shared orbital plane changes. The presence of the perturber precesses the longitudes of ascending node of all the inner planets at the same rate, which is also shown in Figures 4.1 and 4.2 (with $\Delta\Omega$). Such "dynamical rigidity" has been seen in simulations of other systems when perturbers are introduced (Kaib et al., 2011) at high inclination, and has been further explored analytically by Boué and Fabrycky (2014a,b).

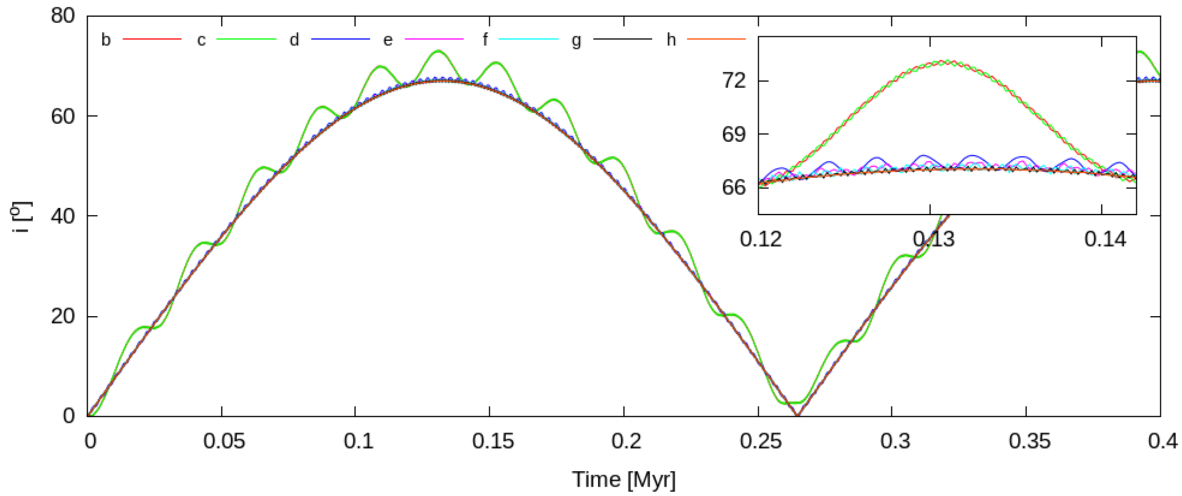

Figure 4.3: K90+ system with a highly inclined perturber with an $I = 50°$ and with $a = 5.2$ au. The dynamical rigidity is evident in the coherent variation of the inclinations. The subpanel is a close up of the inclination within 0.12 to 0.14 Myrs to show that the mutual inclination evolution of the planets remains small due to the synchronous nodal precession of the planets, even though the common orbital plane oscillates.

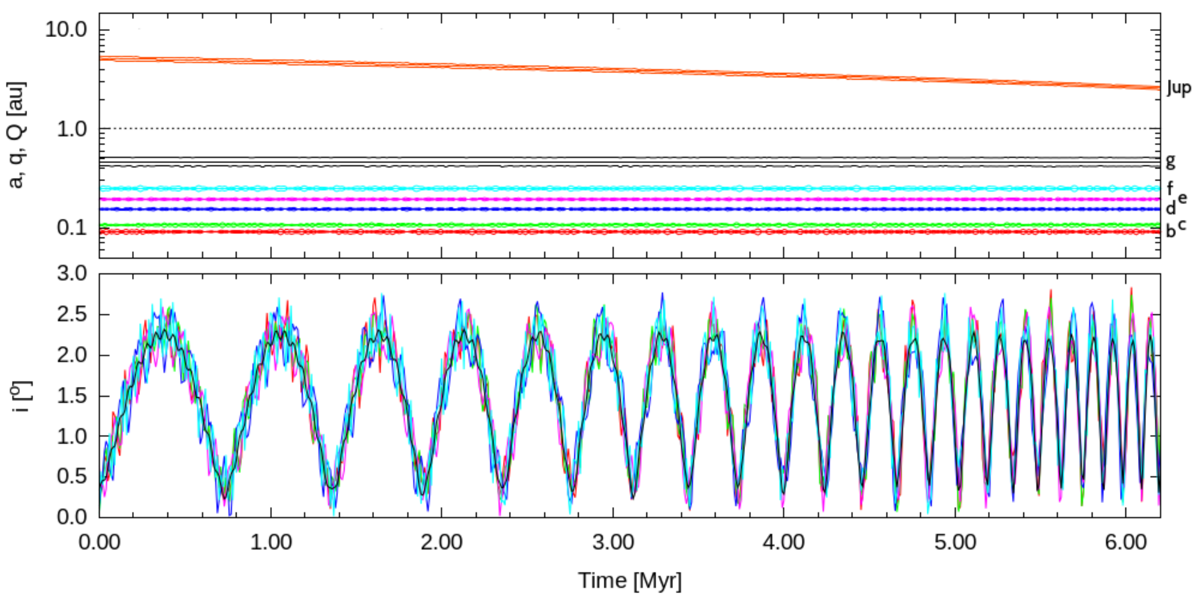

Figure 4.4: Orbital evolution of K11+ in the presence of a migrating outer perturber. *Top panel:* each planet displays 3 curves: pericenter, q; apocenter, Q; and semi-major axis, a. Only the first 6.2 Myrs of the simulation are shown. The forced migration of the perturber, labeled as "Jup", can be observed in orange. The dashed line indicates the perturber's location $a_J = 0.98$ au (at $t \approx 10$ Myrs) at which the system becomes unstable, possibly due to secular perturbations prompted by the perturber. *Bottom panel:* the orbital inclination, I, is shown. While the system is stable, the precession rate of the common orbital plane increases as a function of the proximity of the perturber.

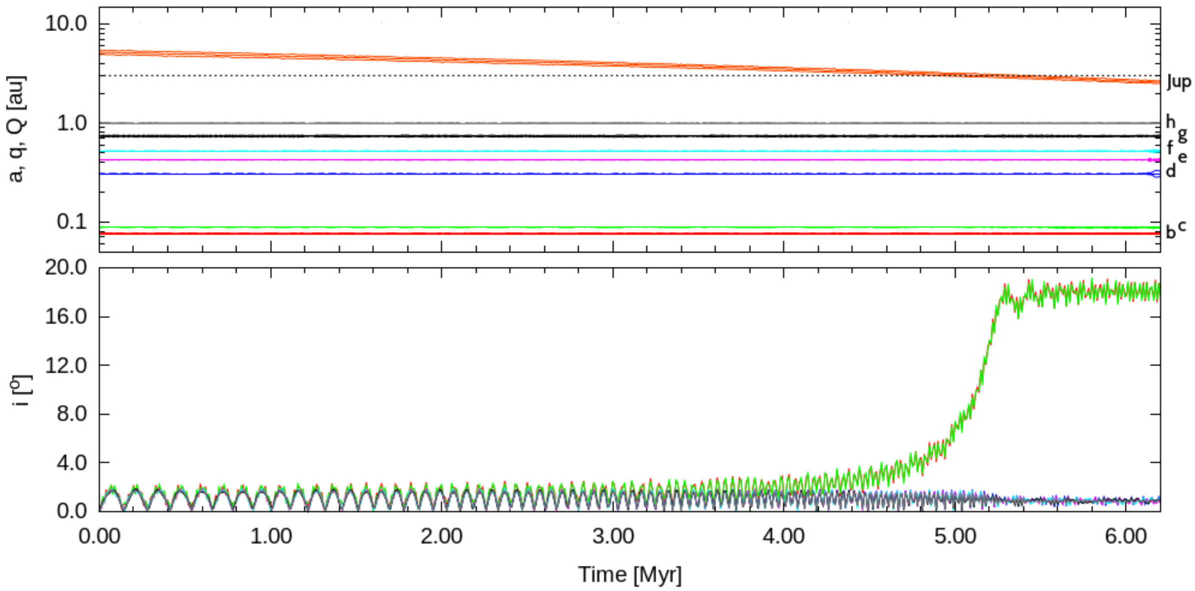

Figure 4.5: Orbital evolution of K90+ in the presence of a migrating outer perturber. The orbital elements are the same as those in Figure 4.4. The precession behavior of K90+ is similar to K11+, with K90+ becoming unstable when $a_{\mathrm{J}} = 2.5$ au (at $t \approx 6.3$ Myrs). However, between perturber orbital distances of approximately $a_{\mathrm{J}} = 2.5$ au and 3.2 au, K90b and c become excited together onto a second plane of higher inclination relative to their original orbits. The dotted line in the top panel indicates the perturber's position at which K90b and K90c inclinations become about 10° larger than the other planets.

Test simulations of K11+ and K90+ with the Jupiter analogue at high inclination (50°), which showed that the longitudes of ascending node remained locked, with the STIP undergoing large and coherent inclination variations (Fig. 4.3), the eccentricities remain small throughout the length of the simulation. We note that the amplitude of the i oscillation is approximately twice the perturber's inclination, although these amplitude is smaller in K90+ which has a larger total planetary mass than K11+, as shown in Figures 4.1 and 4.2.

We have thus far only considered one location for the perturber, arbitrarily introduced at 5.2 au. We now explore a wider range of semi-major axes by forcing the perturber to migrate inwards from 5.2 au to about 1 au (Eq. 4.1). First, the overall behavior of the STIPs is unchanged by simply moving the Jupiter analogue inwards. Figures 4.4 and 4.5, for example, show that the systems continue to exhibit coherent changes in the orbital plane, but with an increasing precession rate of the plane as the Jupiter analogue approaches the inner system. However, for certain system configurations, the outcomes can be very different. In most cases, this appears to be due to shifts in the secular frequencies. For example, eccentricity resonances can drive the STIP towards instability, causing planetary collisions (as occurs for K11). An inclination resonance can force a planet (or planets) out of the original common orbital plane, effectively creating multiple orbital planes in a stable system (as occurs in K90). Specifically, runs with an initially stable K11+ develop an instability if the perturber reaches a semi-major axis of 1.0 au, which places the perturber in a 3:1 near-MMR with K11g. This commensurability could be causing the instability in K11+, but the secular resonances could also have a strong contribution to the destabilization of K11+, as will be discussed shortly. At this time, 59% of the unstable K11+ realizations result in either K11b crossing the orbit of K11c followed by K11f crossing K11e's orbit or vice versa.[31] In K90+, when $a_{\rm J} \lesssim 3.2$ au, K90b and K90c evolve together away from the rest of the planets by about 16° in inclination, with the system remaining stable.

4.3 Secular theory vs. synthetic secular theory

The behavior of both K11+ and K90+, observed in Figures 4.4 and 4.5, can be understood by looking at their forced eccentricities and inclinations. Figures 4.6 to 4.8 show the forced inclination (red solid line) and eccentricity (black dashed line) of K11+ and K90+ at selected locations of the perturber. As the Jupiter analogue moves inwards, the locations of the innermost inclination and eccentricity resonances move outwards in the STIP, eventually crossing the innermost planets. For K11+, an inclination and eccentricity resonance overlap the semi-major axis of K11b when $a_{\rm J} = 0.98$ au (Fig. 4.6), which is when instability occurs in the corresponding simulations. For this analysis, K11b and K11c were removed from the secular theory calculation, effectively treating them as test particles.

In the case of K90+, when the perturber is at $a_{\rm J} \approx 3.3$ au the two innermost planets appear to be trapped in an inclination secular resonance, as determined by secular theory with planets K90b and K90c removed (Fig. 4.8). Together, Figs. 4.5 and 4.8 suggest that the separation of the K90+ system into two distinct orbital planes (for $a_{\rm J} \lesssim 3.2$ au) is due to an inclination resonance overlapping the K90b and K90c positions. This secular resonance excites the inclination of both planets, which are strongly coupled, and its strength increases as the perturbing planet's distance to K90 decreases. This second orbital plane for K90b and K90c can acquire a maximum inclination $i_{bc} = 18^o$ if $a_{\rm J} \approx 3.0$ au. While there is also an inclination resonance overlapping the location of K11b in K11+ (when $a_{\rm J} \approx 0.98$ au), an eccentricity resonance is also present (Fig. 4.6), possibly leading to instability before large inclination changes can occur.

Removing planets b and c from both K11+ and K90+ for the secular calculations assumes that the planets are massless, which is not true. As such, the method is not guaranteed to highlight resonances, although the agreement with the N-body simulations suggest that the approximation is valid in this case. Removing the planets nonetheless reduces the complexity of the frequency structure in the analytic theory. To highlight this, we show in Fig. 4.7 a secular map in which we only remove K11b, allowing K11c to contribute to the secular model. An inclination and eccentricity resonance is present at $r \approx 0.09$ au, just inside K11b. The position

[31] K11f crossing the orbit of K11e first and then K11b crossing K11c's orbit.

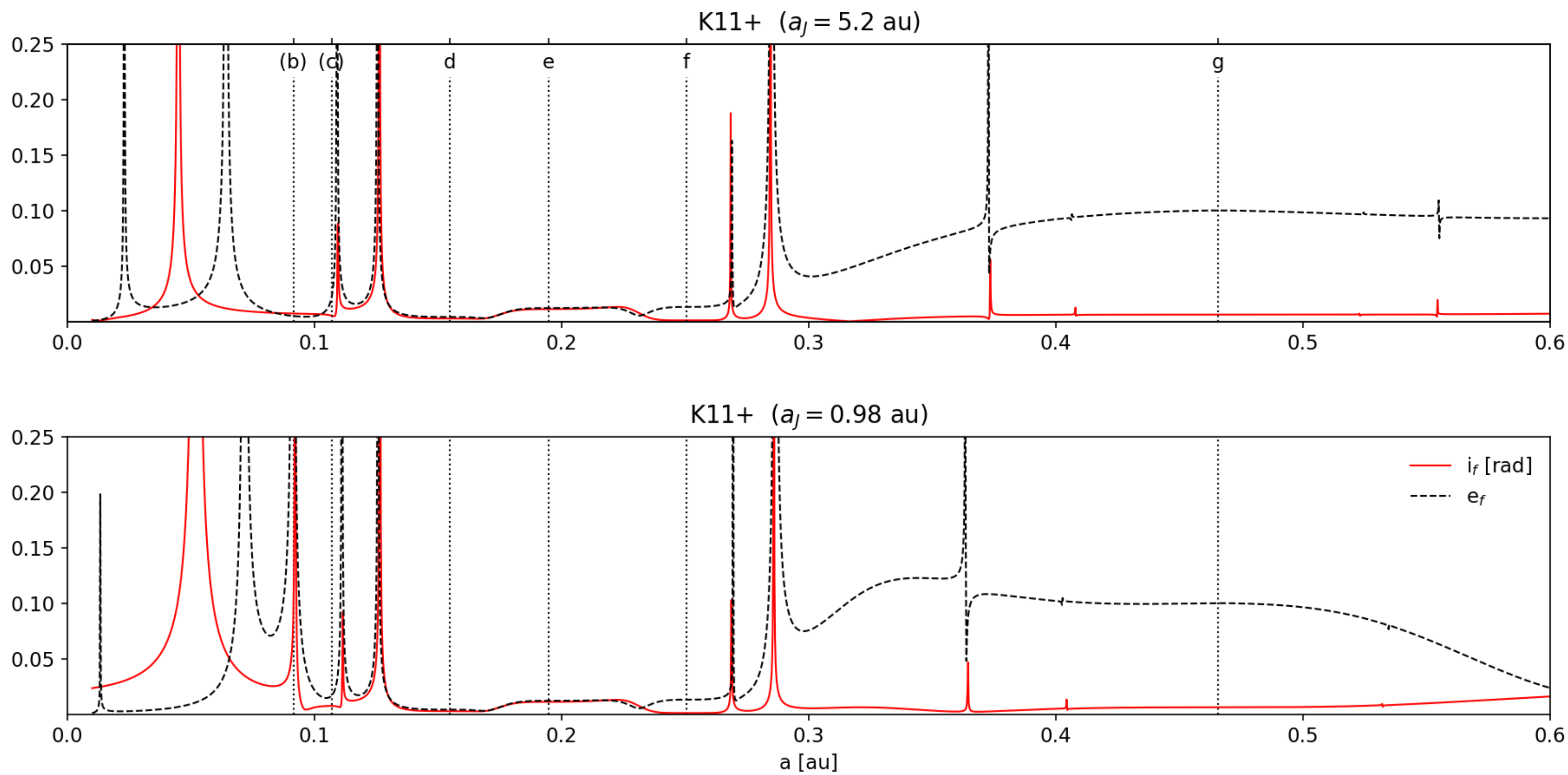

Figure 4.6: Secular map of the forced inclination (red solid line) and eccentricity (black dashed line) of K11 in the presence of a Jupiter-like perturber and excluding the planets in parenthesis of the calculations, i.e., K11b and K11c. Two different semi-major axes of the perturber are shown in the top and bottom panels. The locations of the inner planets are shown by vertical dotted lines. *Top panel:* the gas giant is at $a_{\mathrm{J}} = 5.2$ au, and none of the resonances coincides with the location of the inner planets. In contrast, when $a_{\mathrm{J}} = 0.98$ au (bottom panel), inclination and eccentricity resonances are located at the position of K11b. In this case the eccentric resonance appears to contribute to destabilizing the system.

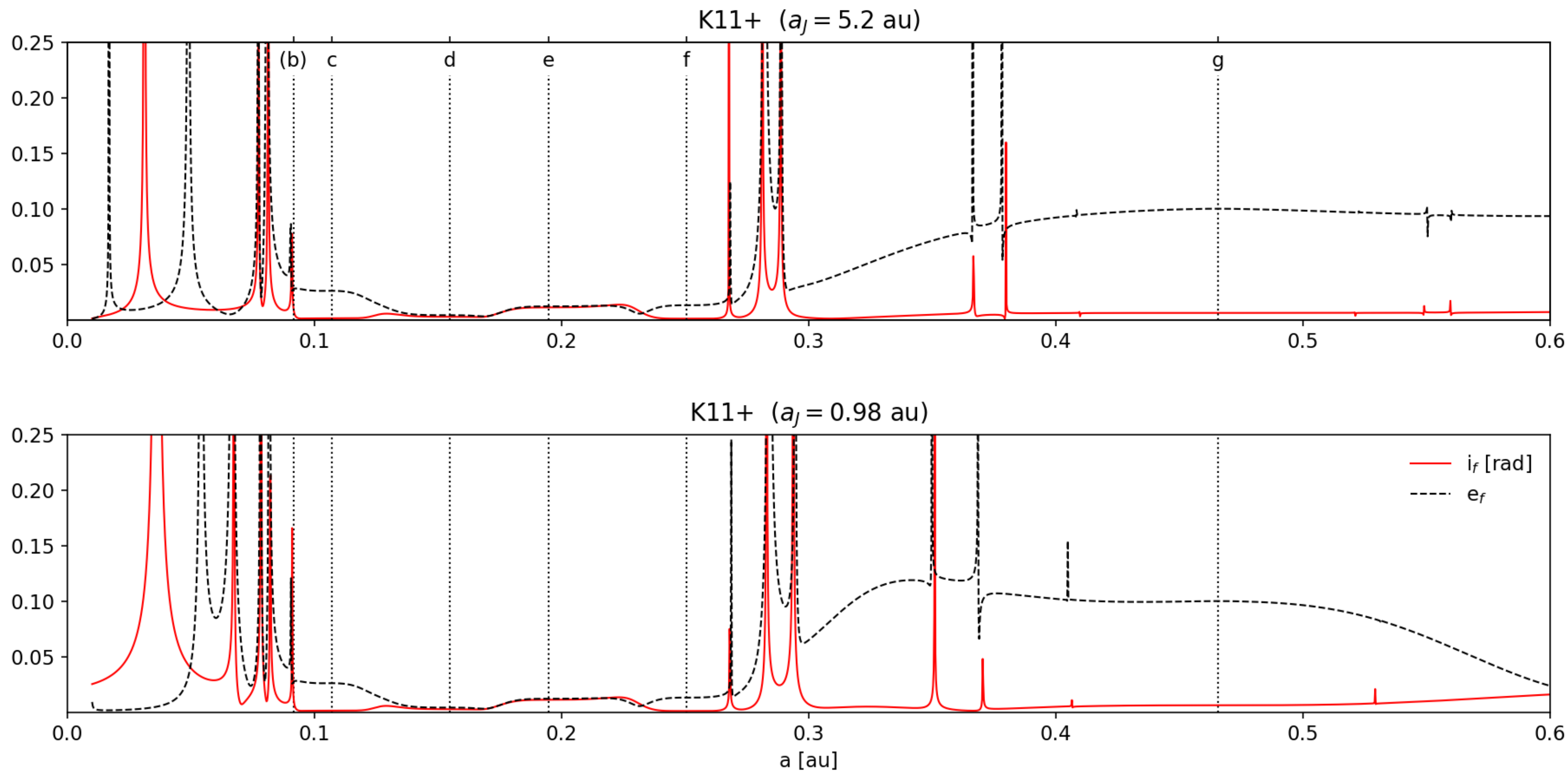

Figure 4.7: Similar to Fig. 4.6, but excluding only K11b (as indicated in the plot). As before, the panels show the results for two different perturber locations. There are multiple inclination and eccentricity resonances just interior to K11b's position. Due to the tight coupling between K11b and K11c, Fig. 4.6 might better reflect the onset of instability. Nevertheless, these panels highlight the richness of the secular structure of the inner system.

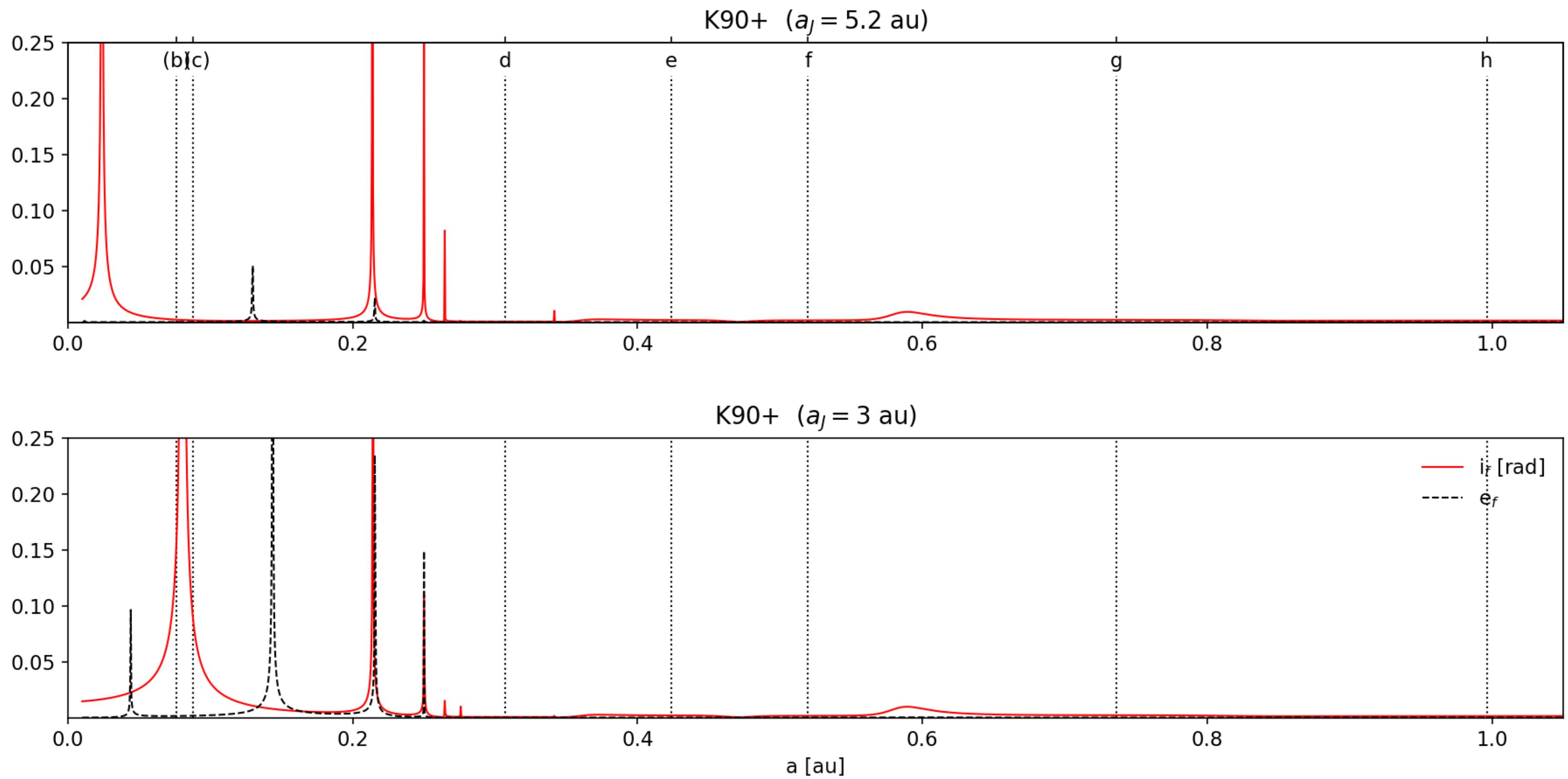

Figure 4.8: Secular map of the forced inclination and eccentricity of K90 in the presence of a Jupiter-like perturber. *Top panel:* the perturber is at $a_{\rm J} = 5.2$ au, and none of the resonances coincides with the location of the inner planets. When we consider $a_{\rm J} = 3.0$ au (bottom panel), a wide inclination resonance is located at the position of K90b and K90c. This resonance increases the inclination of both K90b and K90c, without affecting the stability of the system.

of this resonance is fixed regardless of the perturber's proximity to the inner system, suggesting that the location of this resonance is due to the K11+ inner planets. There are additional resonances that are at even smaller semi-major axes, which are affected by the perturber's location. As the perturber moves inwards, this inner resonance structure moves outwards and the resonance wings overlap. At face value, Fig. 4.7 suggests that K11b might not enter a secular resonance because the resonance just inside K11b's semi-major axis does not change location when different semi-major axes are explored for the perturber, not even when $a_{\rm J} = 0.98$ au. We will later show that K11b and K11c are strongly coupled and Fig. 4.6 might better reflect the outer system's influence on K11b and K11c. Nevertheless, Fig. 4.7 shows the proximity of these resonances to K11b, which could explain the observed instability of the system and its apparent *fine tuning* even when the perturber is absent, because this particular feature seems to be an intrinsic property of the inner system. A small perturbation in the configuration of planets could cause K11b to enter a secular eccentricity resonance and collide with K11c, the most common outcome in our unstable simulations.

We investigate the secular structure of the systems further by calculating the synthetic secular frequencies (precession spectra) with and without the perturber. The precession spectra are determined directly from the N-body calculations, using 0.3 Myr of output with a sample time of 60 years. The total integration time limits the resolution of the lowest frequency, in this case the lowest frequency is 0.0012° yr^{-1} or $4.3''$ yr^{-1}. In K11+ and K90+, the perturber is set to $a_{\rm J} = 0.98$ au and $a_{\rm J} = 3.0$ au, respectively. The synthetic precession spectra and phase angles are compared with the apsidal and nodal secular eigenfrequencies in Figures 4.9 through 4.12. We note that in these four figures, the scaling of the x-axis is divided in two. For frequencies shorter than 1° yr^{-1}, we use a logarithmic scale, and linear otherwise. As expected, the value and number of eigenfrequencies change from K11 to K11+ and K90 to K90+, respectively, due to the additional planet in the perturbed systems, with a greater displacement for the apsidal eigenfrequencies. The amplitude of the global Fourier spectra, in both eccentricity and inclination, for K11+ and K90+, is higher than in the unperturbed analogues; there is about one order of magnitude difference in K11+ and two to three in K90+. The nodal eigenfrequencies show very good agreement with the synthetic spectra for both K11(+) and K90(+), although there are some deviations. The apsidal precession frequencies of both systems exhibit stronger disagreement between the synthetic spectra and the secular theory, but the features in the Fourier spectra remain recognizable, particularly for K11(+). The misalignment of the principal apsidal frequencies relative to the estimated secular eigenfrequencies might indicate that there are strong interactions among the planets, which are neglected in the secular calculation. This could include non-linear secular resonances and near-mean motion resonance (MMR). Malhotra et al. (1989) showed that the $e-\varpi$ eigenfrequencies are significantly shifted if a near first order MMR is present in the system because the averaged effect of the term $e\,\cos(j\lambda-(j+1)\lambda'+\varpi)$ in the secular expansion is non-zero. There is a weaker effect of such a near-resonant term on

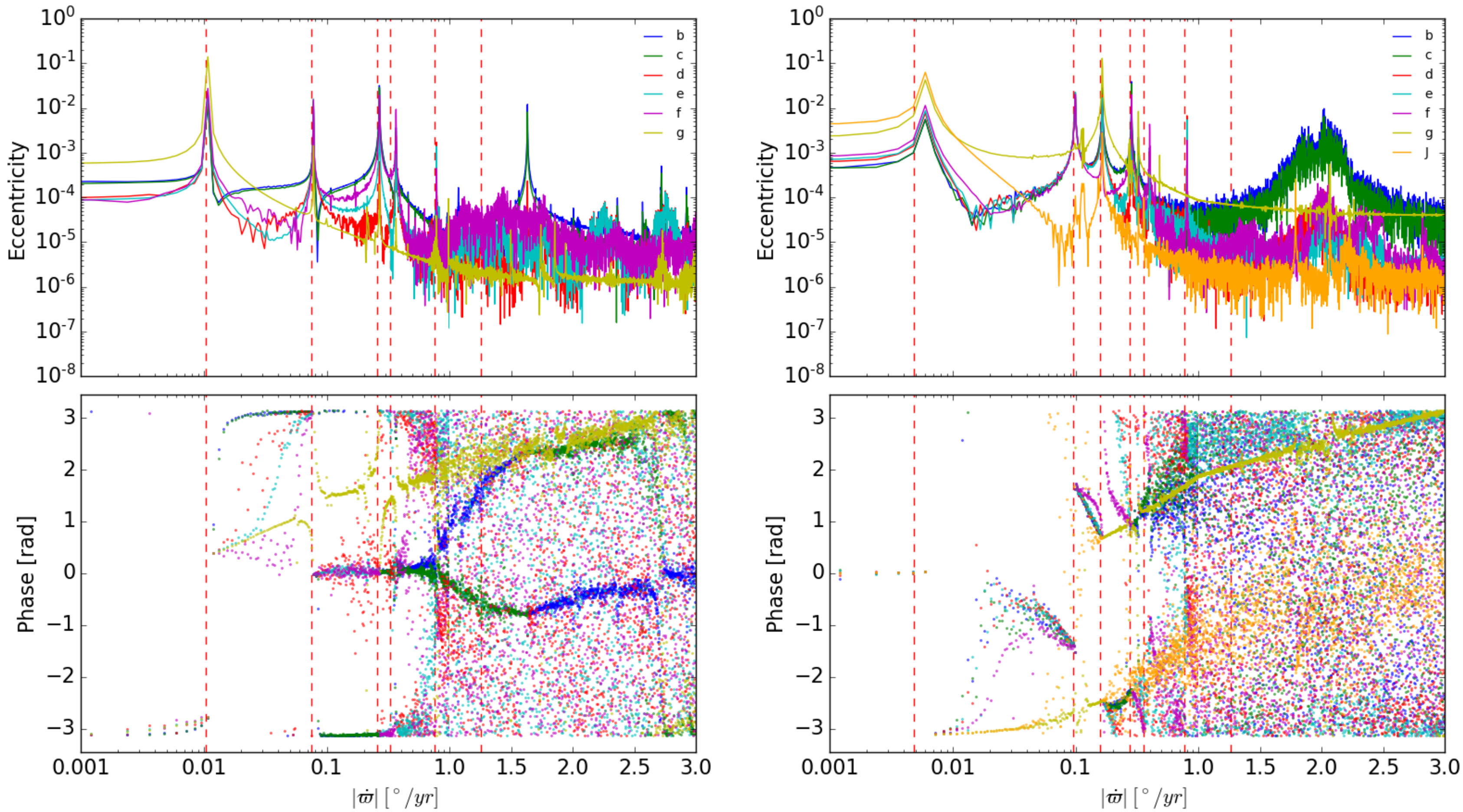

Figure 4.9: Comparison of the theoretical and synthetic apsidal precession frequencies and phases of K11 (left) and K11+ (right). Note that the frequency axis is divided in two different scales; the frequencies $< 1^\circ$ yr^{-1} are scaled logarithmically, and linearly otherwise. *Top panels:* Apsidal precession spectra, where at least two of the principal frequencies are offset from the nearest eigenfrequency. The discrepancy between the theoretical and synthetic principal frequencies indicates that an unaccounted eccentricity secular non-linear resonance is present in K11+. *Bottom panels:* Phase angle of the periapses of K11 and K11+ planets. The periapses of both systems are preferentially out of phase and circulating for high precession frequencies, except for K11b, K11c and K11g (on the left). K11b and K11c exchange phases at shorter precession periods.

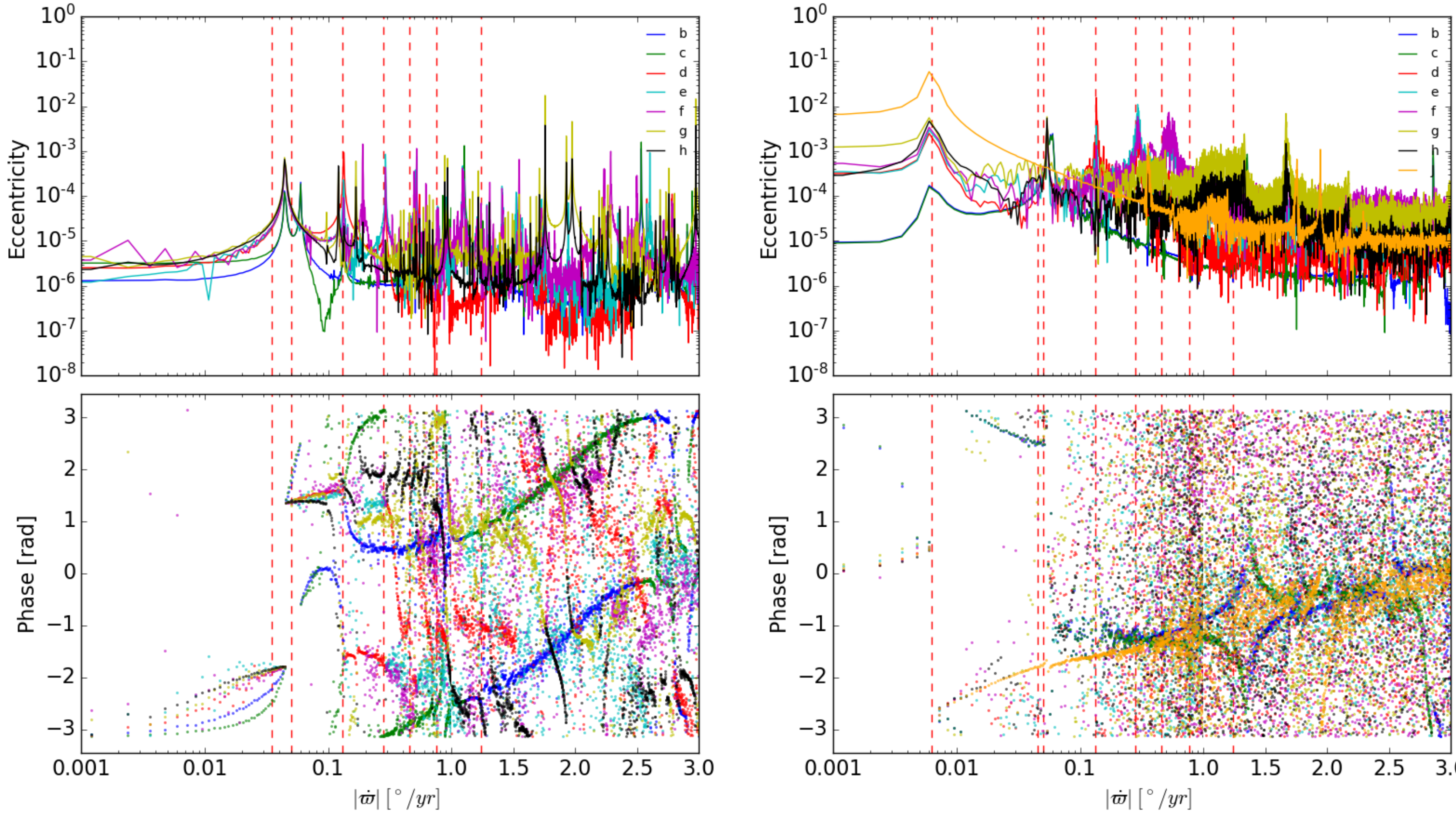

Figure 4.10: Comparison of the theoretical and synthetic apsidal precession frequencies and phases of K90 (left) and K90+ (right). The notation used in Fig. 4.9 is adopted here. For these configurations, there is aliasing at higher $\dot{\varpi}$ (short periods) and the characteristic precession frequencies miss most of the estimated eigenfrequencies. The aliasing reflects in the phase of the periapses, for both K90 and K90+ systems. In K90, K90b and K90c exchange pericenters at different timescales. In K90+, for most planets and timescales, the pericenters circulate, with the exception of K90b, K90c and the perturber.

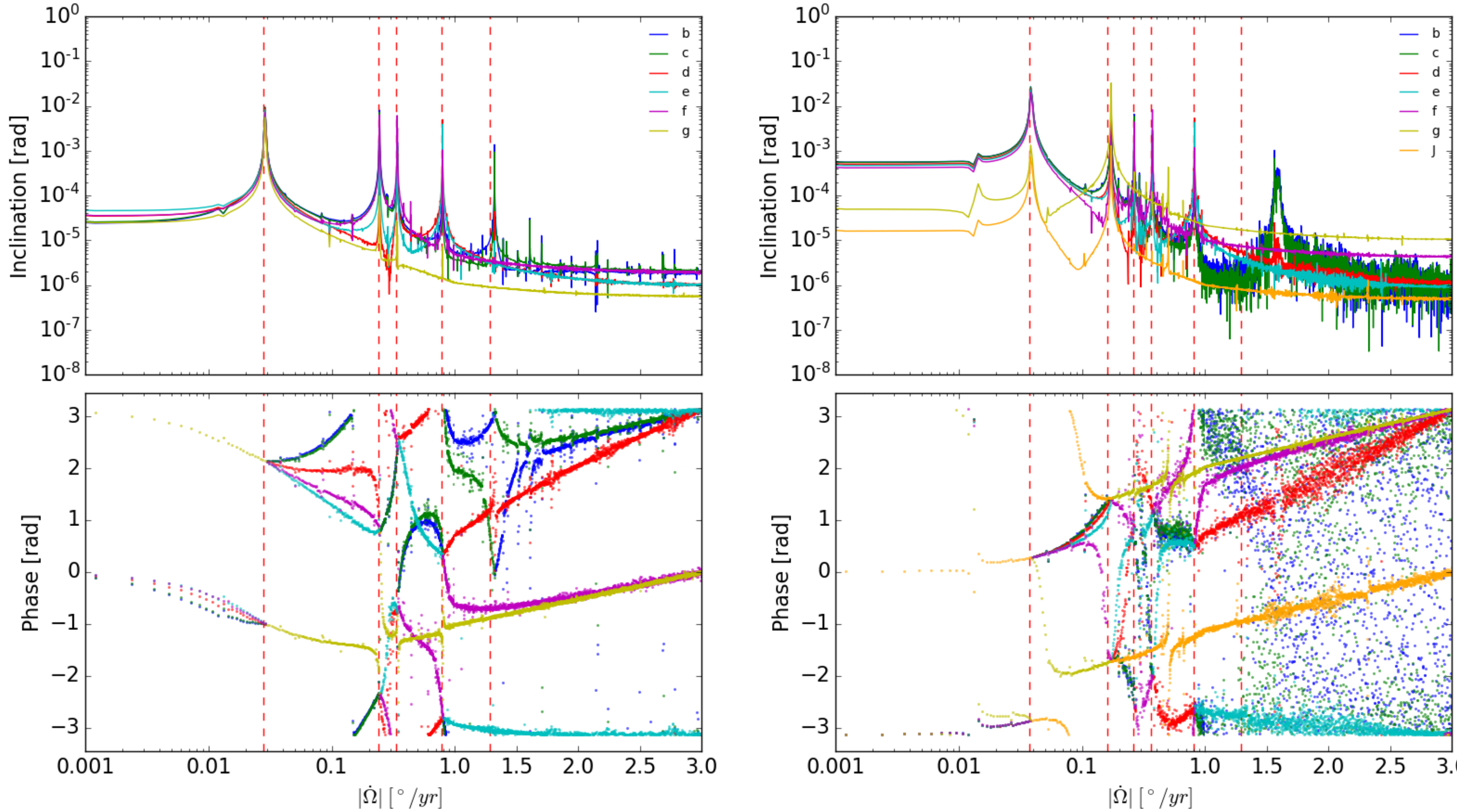

Figure 4.11: Comparison of the theoretical and synthetic nodal precession frequencies and phases of K11 (left) and K11+ (right). *Top panels:* Nodal precession spectra, there is a closer alignment of the principal precession frequencies with the eigenfrequencies than in the apsidal case. *Bottom panels:* Phase angle of the nodes; in both systems it is clear that there is some degree of dynamical rigidity, or nodal locking. This locking is probably induced by K11g in K11. When the perturber is present, it causes the nodal locking. K11b and K11c nodes circulate at high nodal precession frequencies, indicating that their nodes do not align on short timescales.

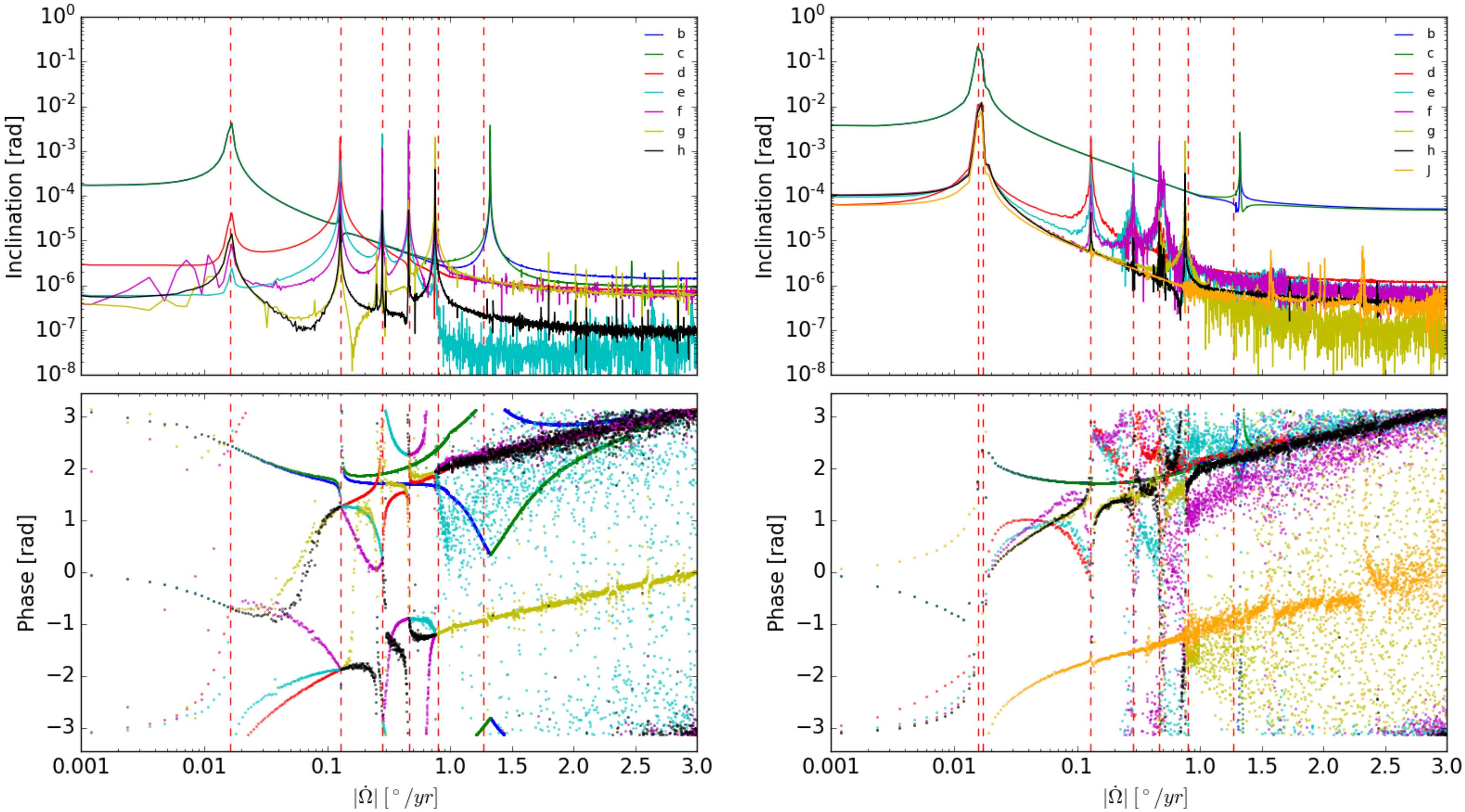

Figure 4.12: Comparison of the theoretical and synthetic nodal precession frequencies and phases of K90 (left) and K90+ (right). The notation used in Fig. 4.11 is adopted here. The characteristic nodal precession frequencies are in close alignment with the eigenfrequencies and the aliasing is minor to moderate. Similar to that seen in in Fig. 4.11, the nodes seem to be locked, which is evidence of dynamical rigidity. In the case K90, K90h seems to be the culprit. The antialignment of K90g might be a result of a metastable configuration. In K90+, as expected, the perturber (in orange) originates a "stronger" rigidity within the STIP, as shown by the aligned planetary node angles.

$i - \Omega$ because the nodal term is associated with i^2. Having this in mind, we will search for possible first-order MMRs in K11 and K90 later in this chapter (Sect. 4.3.1). The MMRs can also add eigenfrequencies to the system, as occurs in the Solar System due to the 5:2 MMR between Jupiter and Saturn (Brouwer and van Woerkom, 1950).

Like the precession spectra, the apsidal phases are not as coherent and well defined as the nodal phases. Large phase changes occur at the principal precession frequencies, with the typical phase changes being near $\pm\pi$ or an exchange of phases between two or more planets. The latter is often seen between the two innermost planets in K11(+) and K90(+), for both in the nodes and pericenters.

The study of the apsidal phases of a system as a function of precession frequency indicate the alignment of the pericenters and the correspondent timescales. For planets in or near MMRs, this alignment can determine whether the configuration is stable, which also depends on the eccentricity and closest approach of the two planets at conjunction (Murray and Dermott, 2000, Ch. 8). We will describe briefly the apsidal alignments and frequency ranges where these are encountered. The further stability study as a function of pericenter conjunctions is out of the scope of this dissertation. The apsidal phases of K11(+) and K90(+) have similar characteristics. In K11 (left panels in Fig. 4.9), the periapses are aligned at very short frequencies, but change phase drastically when $|\dot{\varpi}| > 0.01° \text{ yr}^{-1}$. For $|\dot{\varpi}| > 1.0° \text{ yr}^{-1}$, planets K11b and K11c become antialigned for $|\dot{\varpi}| > 1.5° \text{ yr}^{-1}$, with the latter being aligned with K11g. The right panel shows the pericenter phases for K11+ in which the perturber is displayed in orange. There is no such preferred phase alignment in this case. In Fig. 4.10, which shows the results for K90(+), the periapses of K90 change phase even more notoriously than in K11 (Fig. 4.9), with a slight alignment for $|\dot{\varpi}| < 0.05° \text{ yr}^{-1}$. There is also clear phase swapping between K90b and K90c. In K90+, the apsidal phases do not show coherent structure, except for K90b, K90c and K90J, which are aligned for $|\dot{\varpi}| > 0.1° \text{ yr}^{-1}$.

The nodal phases provide information about the orientation of the nodes within a STIP, and can be used to determine whether a planetary system shows dynamical rigidity. The node of K11g, in K11, is approximately π rad out-of-phase with respect to the rest of the planets for short precession frequencies (see left bottom panel Fig. 4.12) within the region $|\dot{\Omega}| < 0.2° \text{ yr}^{-1}$. At higher nodal frequencies, the node of K11f aligns to K11g's making them both antialigned to the nodes of the other planets in the system. This major nodal conjunction within a STIP is an indication that one of the planets in the STIP is locking the nodes, in this case K11g. In comparison, the nodes of the inner planets of K11+ are aligned with each other but π rad away from the perturber's node at frequencies $|\dot{\Omega}| < 1.5° \text{ yr}^{-1}$ and $|\dot{\Omega}| \geq 0.8° \text{ yr}^{-1}$. The nodes of K11b and K11c circulate at precession frequencies $|\dot{\Omega}| > 1.0° \text{ yr}^{-1}$. K90 nodal phases (Fig. 4.12) are difficult to interpret for precession frequencies below $|\dot{\Omega}| < 1.0° \text{ yr}^{-1}$. Above this threshold the planetary nodes are aligned, except for K90g, which is antialigned to the other planets. K90h seems to drive the nodes of most of the planets. Something similar occurs with the nodes

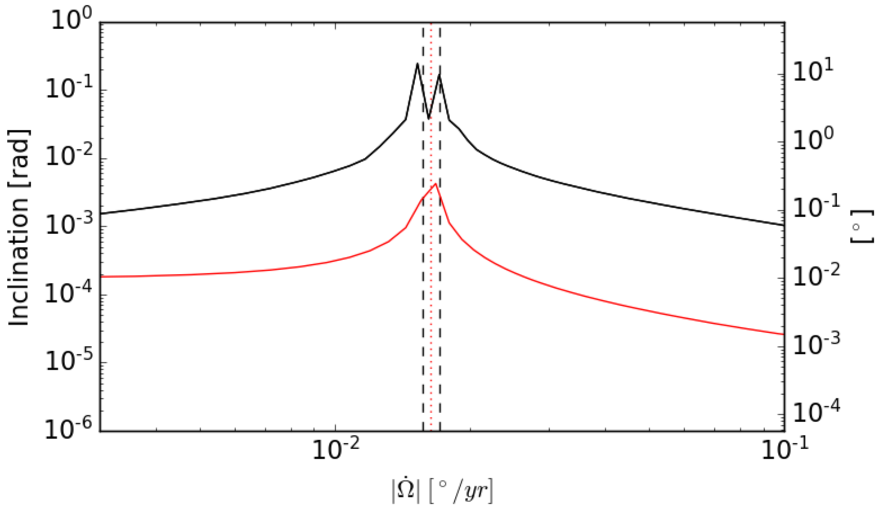

Figure 4.13: Zoom-in of the nodal principal component of planet b in K90 (red line) and K90+ (black line). In this case, K90+ was evolved for 0.4 Myrs, which increased the resolution of the Fourier transform. The K90+ dominant peak on the top right of Fig. 4.12 splits into two peaks when the resolution is increased. The vertical black dashed-lines represent the eigenfrequencies for K90+ in the given range, while the red dotted line corresponds to the eigenfrequency for K90 in that range.

of K90+, but in this case all nodes in the STIP are aligned with K90h (including K90g) and misaligned to Jupiter's node. This is another example of internal node locking within a STIP.

The main precession period of each planet, in K11(+) and K90(+), and the corresponding amplitude are displayed in Table 4.2. In the four systems, the two innermost planets have the same main precession period ($\dot{\varpi}$ and $\dot{\Omega}$) and their precession spectra are almost indistinguishable, confirming the strong coupling of these planetary pairs. Furthermore, in K11, the nodes of the six planets are dominated by the same period, suggesting that K11g is dominating the nodal precession, which causes a dynamical rigidity in the orbital plane. On the other hand, there are two distinct pericenter precession periods, in which K11b and K11c have an apsidal period of $P_{K11b-c} \simeq 1346$ yr and K11d through K11g have periods of $P_{K11d-g} \simeq 33340$ yr. The perturber in K11+ changes the frequencies and decouples K11g; K11g's node precesses at the same rate as the perturber, which is around 4 times faster than the rest of planets in K11+. In contrast to K11, the main nodal precession periods of K90 do not suggest an intrinsic dynamical rigidity, although there is strong coupling between K90b and K90c, as well as K90g and K90h. However in K90+, there are two distinct nodal precession periods that are different by only 7%. These nearly overlapping eigenfrequencies (Fig. 4.12) suggest that a secular resonance is causing the large change in inclinations for K90b and K90c (Fig. 4.5). The amplitude of the broad frequency peak seen in Fig. 4.12 dominates the spectra by one order of magnitude or more. When the K90+ simulation is allowed to evolve to 0.4 Myrs,[32] it is possible to identify the

[32]The integration time is limited by instability of the system after 0.4 Myrs

Planet	K11		K11+		K90		K90+	
	$P_{\rm ap}$ (yrs)	e	$P_{\rm ap}$ (yrs)	e	$P_{\rm ap}$ (yrs)	e	$P_{\rm ap}$ (yrs)	e
b	1346	0.0225	1266	0.0276	104	0.0008	6667	0.0028
c	1346	0.0201	1266	0.0246	104	0.0011	6667	0.0026
d	33340	0.0131	3615	0.0158	2703	0.0007	2655	0.0110
e	33340	0.0146	3615	0.0157	138	0.0007	1230	0.0078
f	33340	0.0194	3615	0.0142	205	0.0012	695	0.0050
g	33340	0.0988	2190	0.0908	205	0.0121	216	0.0047
h	···	···	···	···	205	0.0026	6667	0.0039
J	···	···	60012	0.0436	···	···	60006	0.0398
	$P_{\rm node}$ (yrs)	i (°)	$P_{\rm node}$ (yrs)	i (°)	$P_{\rm node}$ (yrs)	i (°)	$P_{\rm node}$ (yrs)	i (°)
b	12503	0.3815	9377	1.0840	21431	0.1738	23079	8.8099
c	12503	0.3777	9377	1.0728	21431	0.1732	23079	8.7856
d	12503	0.3492	9377	0.9740	2831	0.0831	21431	0.4781
e	12503	0.3374	9377	0.9362	1288	0.0988	21431	0.4999
f	12503	0.2893	9377	0.8085	785	0.1174	21431	0.4982
g	12503	0.2253	2084	1.3211	480	0.0864	21431	0.4880
h	···	···	···	···	480	0.0164	21431	0.4829
J	···	···	2084	0.0525	···	···	21431	0.3145

Table 4.2: Main precession period and amplitude of each planet in K11, K11+, K90, and K90+. $P_{\rm ap}$ and $P_{\rm node}$ denote the apsidal and nodal period, respectively. The values of e and i provided here are the maximum amplitudes from Figures 4.9, 4.11, 4.10 and 4.12 for each planet, and whenever pertinent, the perturber. The apparent switch of the nodal precession from planets K90b and K90c to K90+d through K90+h is an artifact of the Fourier frequency spacing, along with a modest change in the eigenfrequency structure. Comparing the tabulated periods among the planets in a system helps to highlight which planets exhibit tight coupling.

two close frequency components in this dominant broad peak, as expected from secular theory for K90+. These are shown in Fig. 4.13, with the peaks corresponding to $P_{\rm node} \simeq 23100$ yr and $P_{\rm node} \simeq 21400$ yr, which straddle the eigenfrequency associated with K90 in that range. The amplitude of these two frequencies varies when the spectra is calculated from a shorter or longer integration, which complicates the identification of the main precession frequency among these two. The whole precession spectra of the longer N-body integration is not shown in Fig. 4.13, due to severe aliasing at large frequencies.

The identification of the frequency components in the apsidal precession spectra of K90 and K90+ (top panels in Fig. 4.10) is complicated due to aliasing. Even so, we can discern a substantial misalignment of the main frequency components compared with the nearest eigenfrequency, as mentioned above. In K90, there is a double-peaked feature corresponding to K90b and K90c at $\dot{\varpi} \sim 0.05^\circ$ yr^{-1}. This is absent in the spectra of the other planets, which could originate from a non-linear secular resonance or from an MMR.

4.3.1 Mean motion resonances MMRs

The discrepancies between the precession spectra of K11 and K90 and their secular eigenfrequencies demonstrate that either additional physics should be included in the secular theory or that we need to consider a higher order expansion in e, i, and mass. Some of the physical effects that we know we are neglecting in the secular code include GR and MMRs. The GR contribution to the precession rates is small; it only affects the apsidal precession frequencies of the synthetic spectra by $\lesssim 2\%$, with K90 being the most affected. GR does not shift the nodal spectra in either system. A MMR, depending on the order, can affect linear terms in eccentricity and inclination.

K11 and K90 exhibit TTVs (Lissauer et al., 2011a; Cabrera et al., 2014), which occur if there are strong gravitational interactions between the planets. The discovery papers of both K11 and K90 also discussed MMRs for different planet combinations. The period ratios of K11b-K11c, and K90b-K90c suggest a 5:4 near commensurability in both systems. In addition, Cabrera et al. (2014) discussed a possible 2:3:4 near resonance between K90d, K90e and K90f. These initial claims of MMR in the systems were based on the period ratios of neighboring planets, but dynamically an MMR might not occur, due to the resonance's dependence on the eccentricity and inclination. To confirm the existence of an MMR in a pair of planets, it is necessary to estimate their resonant angle.

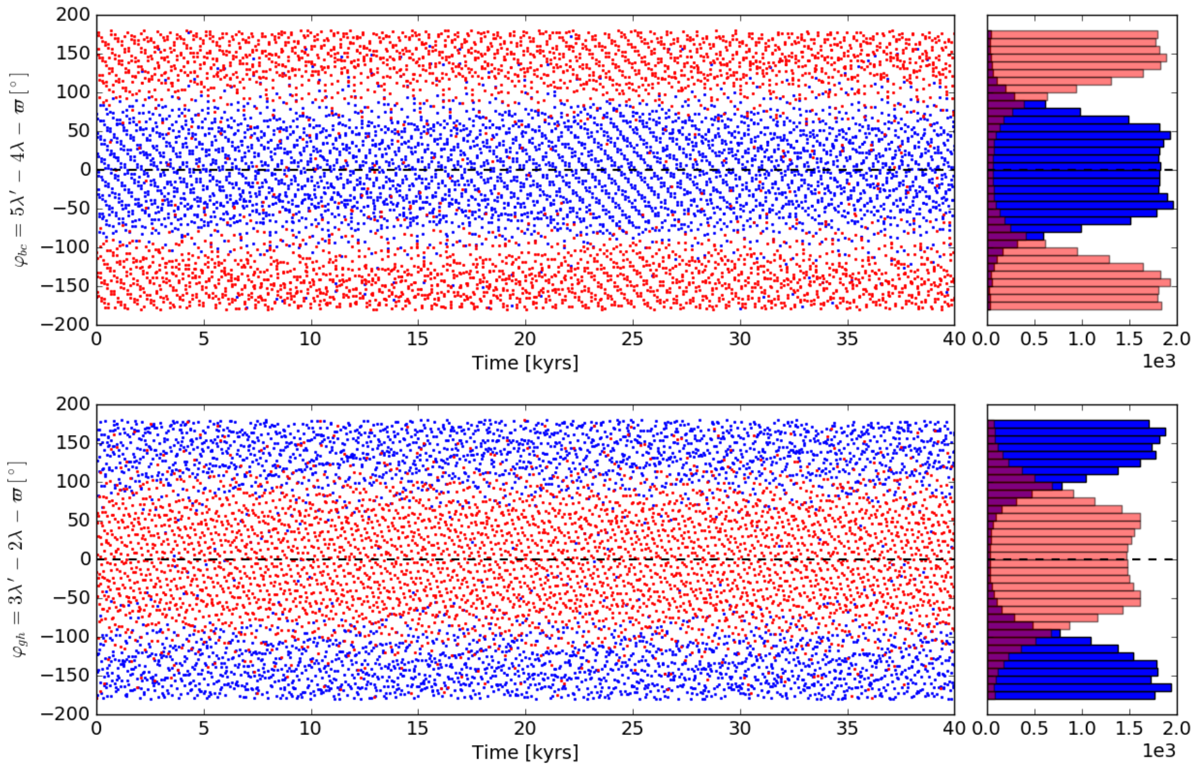

Figure 4.14: Librating resonant angles in K90. In blue is the interaction with the external planet, φ', and in red with the internal, φ. For clarity, the left panels show the time evolution of the resonant angle only within the first 40 kyr of the simulation; while the right panel (vertical histograms) summarize the behavior of φ' and φ over 0.3 Myrs. The top panel corresponds to the 5:4 near-MMR between K90b and K90c. The bottom panel shows the resonant angle between K90g and K90h in a 3:2 near-MMR.

The two resonant angles for a first-order MMR between neighboring planets can be calculated from the N-body simulations using

$$\varphi' = j\lambda' + (1-j)\lambda - \varpi', \tag{4.2}$$

$$\varphi = j\lambda' + (1-j)\lambda - \varpi, \tag{4.3}$$

where λ is the mean longitude and ϖ is the longitude of pericenter. The prime here denotes the external planet. If the planets are in an MMR, one or both resonant angles will librate. Using the given masses and orbital elements for K11, we find that all the resonant angle combinations circulate at all times. Thus, we cannot confirm a 5:4 near-MMR between K11b and K11c. In K90's case, two pairs of neighboring planets display a librating first-order resonant angle (Fig. 4.14). These plots suggest that K90b is in 5:4 MMR with K90c and that K90g is in a 3:2 MMR with K90h. In both cases, the resonant angle librates with large-amplitude around 0° and 180°. The existence of the 5:4 resonance between K90b-c suggests that some migration could have taken place. The possible 3-body resonance between d, e and f noted by Cabrera et al.

(2014) would correspond to a resonant angle $\varphi = 2\lambda_{\mathrm{d}} - 6\lambda_{\mathrm{e}} + 4\lambda_{\mathrm{f}}$. After plotting this angle from our simulations, we find that the resonant angle circulates through the length of the realization. The 3:2 MMR between K90g and K90h could be contributing to the instability present in the K90 simulations with secular resonances that were not accounted in our secular theory calculations. This instability would depend on the exact masses of the planets, particularly those for K90g and K90h (Cabrera et al., 2014), which are the most massive. Although, the nominal masses of K90 planets are unknown, the impact of these massive planets on the system stability could be strengthened by their apparent MMR.

The behavior of the K11 and K90 analogues explored here show a range of dynamical outcomes that STIPs could have in the presence of an outer (undetected) perturber. To date, it is uncertain whether the detected planets among the known exoplanet systems represent a complete set or whether there are undetected planets in those systems. Follow up measurements of orbital inclinations of STIPs, using transit duration variations (TDVs), could reveal dynamic rigidity in the orbital plane and as a consequence, could be used as an indirect detection method for an outer planet. The observational determination of the longitudes of the nodes of planets in a given STIP could tell us whether there is an external perturber should the $\Delta\Omega$s for all the planets be $\lesssim 20^{\circ}$ (this value coming from Figs. 4.1 and 4.2). In a non-perturbed STIP, the nodes would not preferentially align to a specific value, although it might be the case that a subset of the planets present nodal alignment due to coupling. Moreover, an external perturber will cause a coherent change in the inclination of the planets, causing the duration of their transits to change coherently. An outer planet could also cause large breaks in the nominal orbital plane, which could explain some spin-orbit misalignment of low mass planets or reduce the number detected by transits.

Chapter 5

Discussion

In Chapters 3 and 4 we discussed the results of the respective individual studies. Here, we expand on this discussion, considering the methodologies and results of the work as a whole. We also highlight caveats and future directions throughout the chapter.

5.1 Close-in giant planets as an extreme outcome of planet-planet scattering.

In the simulations that explored the metastability of STIPs and corresponding planet consolidation, the outcomes were very different between simulations with and without gaseous tidal damping. Undoubtedly, this damping has an important effect on the stability of the systems. The initial conditions that we used in these studies also likely played a key role in determining the results. In particular, systems that were K11 analogues had a higher mass than the six-planet synthetic systems, which was an unintended consequence of the experimental design. Specifically, the K11 analogues contained $30.1\,M_{\oplus}$ in planets, while the six-planet systems explored with tidal damping had on average a much smaller total planetary mass. Thus three critical cores would form in principle in the K11 analogues, while typically only one, and in many cases none, could form in the synthetic systems (Fig. 3.2). This inconsistency between studies was introduced in an attempt to use random planetary masses within a specific range that also did not already have essentially a critical core. This approach would seem to be reasonable. However, a multiplicity larger than six should have been used to increase the range of possible STIP masses. Moreover, gaseous tidal timescales are inversely proportional to a planet's mass, causing small planets to damp quickly. This could justify having a large number of small planets packed tightly together as an initial condition for proto-STIPs in gas.

While not conducted as part of this work, the project's outcomes could be readdressed by fixing a total system mass, and making many realizations of planet masses and multiplicity to build synthetic STIPs. The total mass could then be associated with a surface density profile inside a given semi-major axis, e.g., 1 au, or orbital period, particularly if a non-solar star is considered in the calculation.

In the synthetic systems, planetary spacings were determined using a fixed number of mutual

Hill radii. Because the planetary masses were randomly assigned, the physical separation between the planets varied as a result. Even though actual planetary spacings in multiple systems follow a distribution with a mean between 12 and 15 mutual Hill radii, the fixed Hill separations were used here for simplicity and also to investigate how the spacings at the end of the simulations would compare with those at the beginning. It is clear that other methodologies could be used. For example, both the initial masses and Hill separations could be randomly assigned through, e.g., uniform, Gaussian, or Rayleigh distributions that are, unfortunately, unconstrained at this time.

While the current simulations require further tuning to properly address the formation of critical cores through STIP instability, they nonetheless reveal an interesting result for the period distributions of the planets. Figures 3.6, 3.7 and 3.9 show that the system evolves to a similar period ratio distribution regardless of the initial separations. Moreover, the structure in the distributions near first-order MMRs has some similarities to the actual period ratio distribution (Fig. 1.2) in that the exact commensurability is depleted, followed by a spike in density at larger period ratios. It would be worth verifying whether we can reproduce the period ratio distribution from our simulations using other initial spacings strategies, planet multiplicities, and disk profiles. The results so far lend support to the idea that the features near MMRs in the actual period ratio distribution are due to dissipative processes. In this case, eccentricity excitation from mutual gravitational perturbations followed by gaseous tidal damping are sculling the distribution. The apparent universality in the period ratio distribution at the end of the simulations suggests that the simulated and known distributions should match, particularly if the gaseous tidal damping is the main driving planet-disk interaction. The evident discrepancy between the observed period ratio distribution (Fig. 1.2) and the one found in Chapter 3 (Figures 3.6, 3.7 and 3.9) points to non-dissipative forces acting on the observed planetary systems, either before or after gas dispersal.

Regardless of the initial mass distribution, critical cores did consolidate in the simulation sets with very tight initial conditions, i.e., small mutual Hill spacings of $f = 1.5$ and $f = 3.0$. We take this apparent efficiency result with caution because the initial separations were within the feeding zone of planetary embryos, and therefore strong instability was expected. Nonetheless, we note that the instability was not halted instantaneously. The unstable systems had approximately 100 orbits to consolidate into a lower multiplicity configuration with more massive components. The period ratio distribution of these sets preserve the general structure of the more initially spaced experiments ($f = 5, 9.5$) and the peak delimited by the 3:2 and 2:1 resonances remains significant. The mutual interaction of among planets and the disk structures the separation of the planets, even in unstable configurations.

We are aware that the gas surface density used, i.e., a MMEN disk, might not be representative of primordial protoplanetary disks. It was used in our simulations in the absence of a better constraint. Other parametrizations of the surface density could be used in subsequent studies.

It would be interesting to test the values used by Dawson et al. (2015), which found that higher solid surface densities form rocky planets on shorter timescales. This correlates with a higher total planetary mass within a given period range.

At the end of the simulations with tidal damping, the planets are on coplanar and nearly circular orbits ($e \lesssim 3 \times 10^{-4}$). When these systems are evolved to much longer timescales without gas, they remain stable. If, on the other hand, the planets are given small eccentricity and inclination perturbations (Sect. 3.3.1), then the systems again exhibit metastability, showing sudden transitions to an unstable state. Should a mechanism exist, whether internal or external, which prevents the planets from becoming perfectly circular, then instability rates could be higher that found in our simulations, even in the presence of gaseous tidal damping. While we have so far only included gaseous eccentricity and inclination damping, there are gas-planet interactions that could cause eccentricity excitation (Benítez-Llambay et al., 2015; Eklund and Masset, 2017). In future studies, such excitation mechanisms could be added to `IAS15`, and should be explored further, including the parametrizations necessary for capturing the effects. Regardless, if instability does set it, then the formation of critical cores should be treated carefully, as dusty/metal-rich environments could cause significant delays in runaway gas accretion (Lee et al., 2014).

An unexpected outcome of our simulations was the formation of coorbital planets. The occurrence rate is low, and a few limited studies have also seen the formation of coorbitals. While it might be easy to dismiss these configurations as flukes of a simulation, should a highly dissipative environment be present during the early evolution of STIPs, coorbital planets are physically possible. A big question to answer here is whether we are capable of detecting coorbital planets should they exist. We pointed out that several detection techniques for coorbital planets have been suggested and some surveys have also been carried out, although no coorbital planets have been found so far. However, many of these studies have focused on the tadpole configuration rather than a horseshoe. This has stability reasoning behind it, because tadpole orbits are usually longer-lived in simulations than are horseshoe orbits. The same situation occurs in the Solar System: a larger number of low mass objects are known to orbit in or near the L4 and L5 Lagrange points than exist in horseshoe configurations. A deeper study of horseshoe orbits is therefore necessary.

A short test of the stability mass limit for horseshoe orbits (Laughlin and Chambers, 2002) showed that the existing threshold in the literature may be incorrect, albeit of the right order of magnitude. According to previous results, two Saturn-mass planets in a horseshoe configuration around a solar-mass star should be stable over long timescales. Preliminary test with Mercury6, on the other hand, resulted in planetary collisions when using initial conditions of previous studies. We did not include this test in the results of Ch. 3, but it could be easily tested and constrained in future work.

More research for understanding transit lightcurves of coorbital horseshoe planets is needed. An analysis similar to that used in studying transit timing variations (TTVs) could help to identify planets in this configuration, especially if results have a resemblance to Fig. 3.13. Success using a TTV analysis would depend on the horseshoe period of the orbits and the observing time. In this sense, it is important to determine an approximate relation for the horseshoe period and the stellar and planetary parameters so that one can determine what type of horseshoe configurations might be detected with a given survey.

Coorbital planets are unlikely to appear in the period ratio distribution, although, as mentioned in Ch. 1, we found six pairs of exoplanets with period ratios close to the 1:1 MMR. Half of these pairs are only candidates and further assessment is challenging. More observations are needed of the K0624, K00521 and K02248 systems. Among the other three pairs, two are thought to orbit different stars (i.e., Kepler-132b and c, and Kepler-271 d and b, Lissauer et al. 2012; Rowe et al. 2014; Morton et al. 2016). The remaining pair, Kepler-1625 b and Kepler-1625 b I (Teachey et al., 2018; Teachey and Kipping, 2018; Heller, 2018), has been claimed to be the first observed exomoon. However, careful examination of their folded lightcurves shows that they are similar to the bottom panel of Fig. 3.16, particularly if the period is mistaken to be double its real value. This can occur in folded transit lightcurves when coorbital planets are at their maximum separation: in the periodogram the highest amplitude corresponds to twice the physical period. The resulting lightcurve folded to the wrong period could look similar to what one might expect for a moon. We could determine whether the published lightcurve of Kepler-1625 b is due to a moon or a coorbital planetary companion by running N-body simulations of a moon orbiting a planet and generating the correspondent transit lightcurve, akin to what was done in Sect. 3.4. The comparison between the folded transit lightcurves of coorbital planets with that of a planet-moon system should show that in the planet-moon system the phase of the second transit does not vary significantly, and it is zero on average with respect to the planetary transit. As was shown, the phase of a coorbital planet pair explores most values except for a $\Delta\phi$ centered at zero.

5.2 STIPs and external planetary perturbers: effects on observability and stability.

The dynamical rigidity of planetary systems has also been observed in the N-body simulations of 55 Cancri (Kaib et al., 2011; Boué and Fabrycky, 2014b) and HD 20794 (Boué and Fabrycky, 2014b). Boué and Fabrycky (2014b) further studied in detail the theory behind the dynamical rigidity of planetary systems in a hierarchical setting, in which the host star is part of a binary or an outer giant planet is present. They particularly explored the conditions needed to drive spin-orbit misalignments (Boué and Fabrycky, 2014a).

Hansen (2017) also found dynamical rigidity while working on the hypothesis that the *Kepler* Single Tranet[33] Excess (KSTE)[34] could be explained by secular resonances driven by long-period giant planets. The KSTE is the fractional surplus of single transiting planets based on the expected fraction determined from the systems with multiple transiting planets. Hansen (2017) found that a fraction of the excess could be explained by a mixed population of Jovian and Saturn analogues, but only if they had high inclinations. They used in their numerical simulations a selection of prototype planetary systems from Hansen and Murray (2013), which included systems with a multiplicity of 3 to 10 planets and masses from 1 to 10 $M_\oplus$. The mass weighted semi-major axis for the systems was $\langle a \rangle_M = 0.26$-$0.5$ au, and external perturbers were placed between 1 and 5 au.

We present a case study of two *Kepler* systems with high multiplicity, which is complementary to Hansen (2017). We demonstrate that it is possible to drive high inclinations of low-mass planets through secular resonances without a highly inclined perturber and confirm that the eccentricities of a STIP are not necessarily affected or interchanged with the high inclinations, as occurs in the Lidov-Kozai effect (Kozai, 1962; Lidov, 1962), driven by a massive planetary outer perturber. In our particular case, the inclination resonance excited the orbit of the two innermost planets in K90+; a single planet could be driven to a similar outcome through secular resonances. It is unclear where in a STIP a secular resonance will develop due the presence of outer planetary companions; more case studies are needed to understand these dynamical effects.

A subset of planets in a system having high mutual inclinations has observational implications. For example, the transit method is biased toward detecting planets that have low inclinations with respect to the observer's line of sight. In the case of K90+, the transit method would detect either two or five planets instead of all seven. An RV observation of the system could make the detection of the out-of-sight planets possible, because the independent velocity amplitude of the two innermost planets would only decay by about 5% ($I \approx 20°$), depending on the overall alignment of the system. In this particular case, the convolution of RV amplitudes is governed by K90g and K90h due to their mass. A quick analysis of the RV observability of K90+ and similar systems could be done by extracting the stellar radial velocity of the N-body simulations and calculating the amplitude of the signal at different observational inclinations.

In these simulations, the Jovian perturber was placed on a low eccentricity orbit ($e \leq 0.05$). If the perturber's orbital eccentricity were to be increased, which affects the width and power of secular resonances, we would expect additional instability. For example, Clement and Kaib (2017) showed that increasing the nominal eccentricity of Jupiter and Saturn by a factor of two enhances chaos within the inner Solar System and reduces the system's stability.

[33] Transiting planet (Tremaine and Dong, 2012).
[34] Also known as the Kepler dichotomy.

As a first step, only a single Jovian perturber was considered in our simulations. Future work will need to include the effects of multiplicity among outer planetary systems. Having two or more Jovian planets would modify the orbital precession frequencies and increase the complexity of the system' secular frequency spectrum, particularly if the giant planets are mutually interacting. This would have consequences for the dynamics and stability of STIPs and could increase the fraction of inner systems that become unstable. As an example, consider studies based, at least in part, on the Solar System, which show that the stability of the inner Solar System or inner system analogues can depend sensitively on the orbital configuration of the Solar System's outer planets (e.g., Lithwick and Wu, 2011; Agnor and Lin, 2012; Clement and Kaib, 2017). The lack of planets detected with orbital periods between 1000 and 10000 days its mainly due to detection biases. A deeper understanding of the gravitational effects of unseen outer planetary systems on configurations like the detected STIPs might help to improve the statistics in this period range. Further research is needed.

5.3 STIPs and giant planets

Migration and in-situ formation are not necessarily exclusive mechanisms. There are many uncertainties in both situations, but there are also physical reasons for thinking that either one could operate, at least under some situations. Both should be explored.

The in-situ formation paradigm could give rise to a rich variety of planetary types on hot, warm or cold orbital distances. The details of their formation may be strongly related to the disk density and the corresponding gas-to-solid fraction. One important consideration for the formation models is the fraction of massive, rocky planets with and without a gaseous envelope, since many planets are close to the typical critical mass (Lee et al., 2014). In our in-situ paradigm, rocky, massive planets would be those that consolidated late, when the gaseous disk had already dissipated.

A present concern is how to determine whether STIPs are just the inner region of a more complex system, or if these configurations are complete systems. One option is to determine the behavior of the inner system with the aid of N-body simulations, and analyze the possible implications in the dynamics and subsequent observation, as we did in Chapter 4. Other options would involve simulating the simultaneous formation of STIPs and an outer system of giant planets. The last option is computationally more difficult to realize because it would need hydrodynamical simulations and depends on many unknown parameters for the initial conditions.

Chapter 6

Conclusions

In Chapter 3, we tested the hypothesis that HJ formation is an extreme outcome of metastability in a STIP. For this study, we have run simulations of STIPs and explored the consolidation of critical cores in both gas-free and gas-rich environments. The gas-rich simulations are N-body realizations with a prescription for gaseous tidal damping. We find that the consolidation of critical cores is only possible in the gas-free environment, because the gaseous tidal damping efficiently removes any source of instability. However, as discussed in Chapter 5, there are many other considerations that need to be explored before we can say that STIP instability is not possible in the presence of gas. The systems that resulted from evolution with gaseous tidal damping were long-term stable. However, instability would still occur if their eccentricities were perturbed to values ~ 0.01.

The period-ratio distribution of the damped systems is independent of the initial orbital distribution and has a characteristic shape and behavior. The period ratios avoid first-order MMRs, especially the 2:1 resonance. Although the tendency is to avoid $i{:}i+1$ resonances, the distribution presents overdensities at slightly larger values. The two highest peaks in the distribution are located at 1.57 and 1.38, just beyond the 3:2 and 4:3 ratios.

Among the N-body simulations of STIPs with gaseous tidal damping, we found two realizations in which planets evolved into coorbital configurations. One of these remains in the 1:1 MMR throughout the length of the simulation and is stable for at least 10 Myr after the gas was removed. Following up this discovery, we examined the detection of the pair with the transit method by synthesizing their lightcurve at 3 different epochs, mimicking *Kepler* observations, with the three epochs reflecting the different regions of the coorbital interaction. The transit separations between the primary and secondary were found to change linearly, non-linearly, or remain roughly constant with time, depending on the epoch. The synthetic transit lightcurves were then analyzed with the Kepler Transit Planet Search pipeline (TPS). Only the bigger planet can be detected without modifying or constraining the searching parameters of the pipeline. The detection of the smaller planet (about 10 times smaller) was only possible on the linear transit lightcurve and if the pipeline was constrain to search for periods within 10% the period of the larger planet. Our preliminary tests of the transit method as a viable technique for detecting coorbital planets seems promising. More testing is needed, however. If successful, transit observations could provide an initial determination of the total mass of the coorbital pair and the mass ratio between them, not only of their sizes and periods.

In Chapter 4, we studied the stability and observability of two known high-multiplicity STIPs, K11 and K90, in the presence of an outer Jupiter-like planet, through both N-body simulations and secular theory. The presence of the perturber causes dynamical rigidity about a common orbital plane for the inner planets, while the stability of the system remains unaltered when compared with unperturbed realizations for most perturber locations. The observed instability seems to be inherent to STIPs, suggesting secular resonances among the planets. The rigid behavior of the orbital plane occurred for most of the parameter space that we explored as long as no instability developed. The presence of the perturber also caused two possible effects on systems that are otherwise stable: (1) the orbital plane of the planets could be separated into two distinct planes, as in K90+; and (2) the system could become unstable for particular perturber locations. The N-body simulations and secular analysis demonstrate that the instability and multiple orbital planes are consequences of the eccentricity and inclination secular resonances, respectively. For K11, we suggest that the eccentricity resonance close to K11b is the source of the system's inherent instability.

Comparing STIP secular eigenfrequencies to the synthetic counterparts provides a deeper insight into the coupling and possible presence of MMRs between planets. K11's nodal precession frequencies indicate dynamical rigidity, seemingly due to K11g, although this is dependent on the actual mass of K11g. In K90, our simulations show a 5:4 MMR between K90b and K90c, as well as a 3:2 MMR between K90g and K90h.

Observations of the rigid behavior of a STIP would indicate the existence of an outer planetary system. It is possible that some of the detected planetary systems with low multiplicity are part of higher multiplicity STIPs that are affected by secular resonances.

Chapter 7

Future work

Here, I briefly describe a number of follow-up studies that could be carried out. Each is complementary to the work in this dissertation, and is a natural extension of many of the projects. The reasoning behind each point is described throughout Chapter 5.

1. The total planetary mass of the synthetic planetary systems in Sects. 3.1.2 and 3.3, was on average 15 $M_\oplus$, which in the best of circumstances could end up consolidating one critical core. To further evaluate the feasibility of the in-situ formation of gas short-period giant (gSPG) a higher average planetary per system should be explored. As a consequence, follow-up of the present work we will need to produce synthetic STIPs with a total mass of at least 30 $M_\oplus$ and run simulations with the same methodology as that used in Ch. 3. Finally, a comparison with the present work would indicate whether the in-situ formation paradigm is feasible.

2. Due to the unknown parameters that realistically describe protoplanetary disks, like typical gas surface densities or temperature profiles, different scalings and radial profiles of $\tau_{\rm local}$ (Eq. 2.5) could be explored in the gaseous tidal damping experiments. I am particularly interested in testing how variations in $\tau_{\rm local}$ shape the final period-ratio distribution.

3. As mentioned before, the gaseous tidal damping is one of several planet-disk interactions that are known to affect the dynamics of planetary systems. I plan to include the parametrization of additional planet-disk interactions within my `IAS15` code. Immediately, I am interested in interactions that excite the eccentricity and inclination of the planets (e.g., Benítez-Llambay et al., 2015; Eklund and Masset, 2017). After the parametrizations are included in `IAS15`, the experiment exploring the formation of critical cores would be repeated and analyzed accordingly.

4. Although, the longterm stability of planets in horseshoe configuration has been previously evaluated (Laughlin and Chambers, 2002; Ćuk et al., 2012). I found an inconsistency with the published threshold after running preliminary simulations to confirm the validity of that threshold. I seek to properly verify the longterm stability for horseshoe configurations with detailed and systematic N-body simulations.

5. Section 3.4 demonstrated that the detection of horseshoe planets with the transit method seems promising, but that more research is needed to properly characterize the transit lightcurves. As a logical continuation, I plan to expand the research on coorbital transit lightcurves and detection by synthesizing and analyzing lightcurves produced by different planetary sizes, masses and semi-major axes.

6. As part of the horseshoe parameter characterization, it is necessary to determine the correlation of the horseshoe period with planetary masses and semi-major axes.

From Chapter 3, Sect. 3.3, has not yet been published which could be done as a single paper taking into account the lack of critical core consolidation, period distribution and evaluation of coorbital transit lightcurves. An alternative is to publish the work in Sect. 3.3 with additional complementary work in two papers. One could focus on the critical core consolidation in the presence of gas, with its respective period distribution, including an additional spacing setup among planets to verify the behavior of the period ratio with gaseous tidal damping. The second could be about transit lightcurves of horseshoe planets, and verification of the longterm stability threshold. In the latter paper, I could also include the transit lightcurve of a moon for comparison and evaluate whether Kepler-1625 bI (Teachey et al., 2018) is likely to be a coorbital planet or an exomoon.

Bibliography

Abramowitz, M. and Stegun, I. A.: 1964, *Handbook of mathematical functions with formulas, graphs, and mathematical tables*, U.S. Govt. Print. Off.

Agnor, C. B. and Lin, D. N. C.: 2012, *Astrophys. J.* **745**, 143

Agol, E., Steffen, J., Sari, R., and Clarkson, W.: 2005, *MNRAS* **359**, 567

Alibert, Y., Mordasini, C., Benz, W., and Winisdoerffer, C.: 2005, *Astron. Astrophys.* **434**, 343

Armitage, P. J.: 2007, *ArXiv e-prints*

Bailes, M., Bates, S. D., Bhalerao, V., Bhat, N. D. R., Burgay, M., Burke-Spolaor, S., D'Amico, N., Johnston, S., Keith, M. J., Kramer, M., Kulkarni, S. R., Levin, L., Lyne, A. G., Milia, S., Possenti, A., Spitler, L., Stappers, B., and van Straten, W.: 2011, *Science* **333**, 1717

Ballard, S. and Johnson, J. A.: 2016, *Astrophys. J.* **816**, 66

Batalha, N. M., Rowe, J. F., Bryson, S. T., Barclay, T., Burke, C. J., Caldwell, D. A., Christiansen, J. L., Mullally, F., Thompson, S. E., Brown, T. M., Dupree, A. K., Fabrycky, D. C., Ford, E. B., Fortney, J. J., Gilliland, R. L., Isaacson, H., Latham, D. W., Marcy, G. W., Quinn, S. N., Ragozzine, D., Shporer, A., Borucki, W. J., Ciardi, D. R., Gautier, Thomas N., I., Haas, M. R., Jenkins, J. M., Koch, D. G., Lissauer, J. J., Rapin, W., Basri, G. S., Boss, A. P., Buchhave, L. A., Carter, J. A., Charbonneau, D., Christensen-Dalsgaard, J., Clarke, B. D., Cochran, W. D., Demory, B.-O., Desert, J.-M., Devore, E., Doyle, L. R., Esquerdo, G. A., Everett, M., Fressin, F., Geary, J. C., Girouard, F. R., Gould, A., Hall, J. R., Holman, M. J., Howard, A. W., Howell, S. B., Ibrahim, K. A., Kinemuchi, K., Kjeldsen, H., Klaus, T. C., Li, J., Lucas, P. W., Meibom, S., Morris, R. L., Prša, A., Quintana, E., Sanderfer, D. T., Sasselov, D., Seader, S. E., Smith, J. C., Steffen, J. H., Still, M., Stumpe, M. C., Tarter, J. C., Tenenbaum, P., Torres, G., Twicken, J. D., Uddin, K., Van Cleve, J., Walkowicz, L., and Welsh, W. F.: 2013, *Astrophys. J., Suppl. Ser.* **204**, 24

Bate, M. R., Lodato, G., and Pringle, J. E.: 2010, *MNRAS* **401**, 1505

Batygin, K.: 2012, *Nature* **491**, 418

Batygin, K., Morbidelli, A., and Tsiganis, K.: 2011, *Astron. Astrophys.* **533**, A7

Beaugé, C. and Nesvorný, D.: 2012, *Astrophys. J.* **751**, 119

Beaugé, C., Sándor, Z., Érdi, B., and Süli, Á.: 2007, *Astron. Astrophys.* **463**, 359

Becker, J. C., Vanderburg, A., Adams, F. C., Rappaport, S. A., and Schwengeler, H. M.: 2015, *Astrophys. J.* **812**, L18

Benítez-Llambay, P., Masset, F., Koenigsberger, G., and Szulágyi, J.: 2015, *Nature* **520**, 63

Boley, A. C.: 2009, *Astrophys. J.* **695**, L53

Boley, A. C., Granados Contreras, A. P., and Gladman, B.: 2016, *Astrophys. J., Lett.* **817**, L17

Boley, A. C., Morris, M. A., and Ford, E. B.: 2014, *Astrophys. J., Lett.* **792**, L27

Borucki, W. J., Agol, E., Fressin, F., Kaltenegger, L., Rowe, J., Isaacson, H., Fischer, D., Batalha, N., Lissauer, J. J., Marcy, G. W., Fabrycky, D., Désert, J.-M., Bryson, S. T., Barclay, T., Bastien, F., Boss, A., Brugamyer, E., Buchhave, L. A., Burke, C., Caldwell, D. A., Carter, J., Charbonneau, D., Crepp, J. R., Christensen-Dalsgaard, J., Christiansen, J. L., Ciardi, D., Cochran, W. D., DeVore, E., Doyle, L., Dupree, A. K., Endl, M., Everett, M. E., Ford, E. B., Fortney, J., Gautier, T. N., Geary, J. C., Gould, A., Haas, M., Henze, C., Howard, A. W., Howell, S. B., Huber, D., Jenkins, J. M., Kjeldsen, H., Kolbl, R., Kolodziejczak, J., Latham, D. W., Lee, B. L., Lopez, E., Mullally, F., Orosz, J. A., Prsa, A., Quintana, E. V., Sanchis-Ojeda, R., Sasselov, D., Seader, S., Shporer, A., Steffen, J. H., Still, M., Tenenbaum, P., Thompson, S. E., Torres, G., Twicken, J. D., Welsh, W. F., and Winn, J. N.: 2013, *Science* **340**, 587

Boué, G. and Fabrycky, D. C.: 2014a, *Astrophys. J.* **789**, 110

Boué, G. and Fabrycky, D. C.: 2014b, *Astrophys. J.* **789**, 111

Brouwer, D. and Clemence, G. M.: 1961, *Methods of celestial mechanics*, Academic Press, New York

Brouwer, D. and van Woerkom, A. J. J.: 1950, in *Astronomical Papers American Ephemeris*, Vol. 13, pp 81–107

Bryan, M. L., Knutson, H. A., Howard, A. W., Ngo, H., Batygin, K., Crepp, J. R., Fulton, B. J., Hinkley, S., Isaacson, H., Johnson, J. A., Marcy, G. W., and Wright, J. T.: 2016, *Astrophys. J.* **821**, 89

Burke, C. J., Bryson, S. T., Mullally, F., Rowe, J. F., Christiansen, J. L., Thompson, S. E., Coughlin, J. L., Haas, M. R., Batalha, N. M., Caldwell, D. A., Jenkins, J. M., Still, M., Barclay, T., Borucki, W. J., Chaplin, W. J., Ciardi, D. R., Clarke, B. D., Cochran, W. D., Demory, B.-O., Esquerdo, G. A., Gautier, III, T. N., Gilliland, R. L., Girouard, F. R., Havel, M., Henze, C. E., Howell, S. B., Huber, D., Latham, D. W., Li, J., Morehead, R. C., Morton, T. D., Pepper, J., Quintana, E., Ragozzine, D., Seader, S. E., Shah, Y., Shporer, A., Tenenbaum, P., Twicken, J. D., and Wolfgang, A.: 2014, *Astrophys. J., Suppl. Ser.* **210**, 19

Burrows, A., Hubbard, W. B., Lunine, J. I., and Liebert, J.: 2001, *Reviews of Modern Physics* **73**, 719

Cabrera, J., Csizmadia, S., Lehmann, H., Dvorak, R., Gandolfi, D., Rauer, H., Erikson, A., Dreyer, C., Eigmüller, P., and Hatzes, A.: 2014, *Astrophys. J.* **781**, 18

Chambers, J. E.: 1999, *MNRAS* **304**, 793

Chambers, J. E. and Wetherill, G. W.: 1998, *Icarus* **136**, 304

Chatterjee, S. and Ford, E. B.: 2015, *Astrophys. J.* **803**, 33

Chatterjee, S., Ford, E. B., Matsumura, S., and Rasio, F. A.: 2008, *Astrophys. J.* **686**, 580

Chen, J. and Kipping, D.: 2017, *Astrophys. J.* **834**, 17

Chiang, E. and Laughlin, G.: 2013, *MNRAS* **431**, 3444

Chiang, E. and Youdin, A. N.: 2010, *Annual Review of Earth and Planetary Sciences* **38**, 493

Clement, M. S. and Kaib, N. A.: 2017, *Icarus* **288**, 88

Cresswell, P., Dirksen, G., Kley, W., and Nelson, R. P.: 2007, *Astron. Astrophys.* **473**, 329

Cresswell, P. and Nelson, R. P.: 2006, *Astron. Astrophys.* **450**, 833

Cresswell, P. and Nelson, R. P.: 2008, *Astron. Astrophys.* **482**, 677

Crida, A. and Batygin, K.: 2014, *Astron. Astrophys.* **567**, A42

Ćuk, M., Hamilton, D. P., and Holman, M. J.: 2012, *MNRAS* **426**, 3051

Cumming, A.: 2004, *MNRAS* **354**, 1165

Cumming, A., Butler, R. P., Marcy, G. W., Vogt, S. S., Wright, J. T., and Fischer, D. A.: 2008, *Publications of the Astronomical Society of the Pacific* **120**, 531

Dawson, R. I., Chiang, E., and Lee, E. J.: 2015, *MNRAS* **453**, 1471

Dawson, R. I. and Murray-Clay, R. A.: 2013, *Astrophys. J., Lett.* **767**, L24

Dones, H., Zahnle, K. J., and Alvarellos, J. L.: 2018, in *American Astronomical Society, DDA meeting #49, id. #102.02*

Dong, S. and Zhu, Z.: 2013, *Astrophys. J.* **778**, 53

Eklund, H. and Masset, F. S.: 2017, *MNRAS* **469**, 206

Everhart, E.: 1985, in A. Carusi and G. B. Valsecchi (eds.), *Dynamics of Comets: Their Origin and Evolution*, Vol. 115 of *Proceedings of IAU*, p. 185, Dordrecht: Reidel, Astrophysics and Space Science Library

Fabrycky, D. and Tremaine, S.: 2007, *Astrophys. J.* **669**, 1298

Fabrycky, D. C., Lissauer, J. J., Ragozzine, D., Rowe, J. F., Steffen, J. H., Agol, E., Barclay, T., Batalha, N., Borucki, W., Ciardi, D. R., Ford, E. B., Gautier, T. N., Geary, J. C., Holman, M. J., Jenkins, J. M., Li, J., Morehead, R. C., Morris, R. L., Shporer, A., Smith, J. C., Still, M., and Van Cleve, J.: 2014, *Astrophys. J.* **790**, 146

Fabrycky, D. C. and Winn, J. N.: 2009, *Astrophys. J.* **696**, 1230

Fischer, D. A. and Valenti, J.: 2005, *Astrophys. J.* **622**, 1102

Ford, E. B.: 2014, *Proceedings of the National Academy of Science* **111**, 12616

Ford, E. B. and Gaudi, B. S.: 2006, *Astrophys. J., Lett.* **652**, L137

Ford, E. B. and Holman, M. J.: 2007, *Astrophys. J., Lett.* **664**, L51

Fressin, F., Torres, G., Charbonneau, D., Bryson, S. T., Christiansen, J., Dressing, C. D., Jenkins, J. M., Walkowicz, L. M., and Batalha, N. M.: 2013, *Astrophys. J.* **766**, 81

Fulton, B. J., Petigura, E. A., Howard, A. W., Isaacson, H., Marcy, G. W., Cargile, P. A., Hebb, L., Weiss, L. M., Johnson, J. A., Morton, T. D., Sinukoff, E., Crossfield, I. J. M., and Hirsch, L. A.: 2017, *Astron. J.* **154**, 109

Gaudi, B. S., Seager, S., and Mallen-Ornelas, G.: 2005, *Astrophys. J.* **623**, 472

Gilliland, R. L., Chaplin, W. J., Dunham, E. W., Argabright, V. S., Borucki, W. J., Basri, G., Bryson, S. T., Buzasi, D. L., Caldwell, D. A., Elsworth, Y. P., Jenkins, J. M., Koch, D. G., Kolodziejczak, J., Miglio, A., van Cleve, J., Walkowicz, L. M., and Welsh, W. F.: 2011, *Astrophys. J., Suppl. Ser.* **197**, 6

Gillon, M., Jehin, E., Lederer, S. M., Delrez, L., de Wit, J., Burdanov, A., Van Grootel, V., Burgasser, A. J., Triaud, A. H. M. J., Opitom, C., Demory, B.-O., Sahu, D. K., Bardalez Gagliuffi, D., Magain, P., and Queloz, D.: 2016, *Nature* **533**, 221

Ginzburg, S. and Sari, R.: 2016, *Astrophys. J.* **819**, 116

Gladman, B.: 1993, *Icarus* **106**, 247

Goldreich, P., Lithwick, Y., and Sari, R.: 2004, *Ann. Rev. of Astron. Astrophys.* **42**, 549

Goldreich, P. and Schlichting, H. E.: 2014, *Astron. J.* **147**, 32

Goldreich, P. and Tremaine, S.: 1980, *Astrophys. J.* **241**, 425

Gonzalez, G.: 1997, *MNRAS* **285**, 403

Granados Contreras, A. P. and Boley, A. C.: 2018, *Astron. J.* **155**, 139

Güttler, C., Krause, M., Geretshauser, R. J., Speith, R., and Blum, J.: 2009, *Astrophys. J.* **701**, 130

Haghighipour, N., Capen, S., and Hinse, T. C.: 2013, *Celestial Mechanics and Dynamical Astronomy* **117**, 75

Han, E., Wang, S. X., Wright, J. T., Feng, Y. K., Zhao, M., Fakhouri, O., Brown, J. I., and Hancock, C.: 2014, *Publ. Astron. Soc. Pac.* **126**, 827

Hands, T. O., Alexander, R. D., and Dehnen, W.: 2014, *MNRAS* **445**, 749

Hansen, B. M. S.: 2017, *MNRAS* **467**, 1531

Hansen, B. M. S. and Murray, N.: 2012, *Astrophys. J.* **751**, 158

Hansen, B. M. S. and Murray, N.: 2013, *Astrophys. J.* **775**, 53

Hatzes, A. P. and Rauer, H.: 2015, *Astrophys. J.* **810**, L25

Hayashi, C.: 1981, *Progress of Theoretical Physics Supplement* **70**, 35

Helled, R., Bodenheimer, P., Podolak, M., Boley, A., Meru, F., Nayakshin, S., Fortney, J. J., Mayer, L., Alibert, Y., and Boss, A. P.: 2014, in *Protostars and Planets VI*, p. 643

Heller, R.: 2018, *Astron. Astrophys.* **610**, A39

Hildebrand, F. B.: 1987a, *Introduction to numerical analysis*, Dover Publications, New York, 2nd edition

Hildebrand, F. B.: 1987b, *Introduction to numerical analysis*, Chapt. 8.11, Dover Publications, New York, 2nd edition

Hippke, M. and Angerhausen, D.: 2015, *Astrophys. J.* 811

Howard, A. W., Marcy, G. W., Bryson, S. T., Jenkins, J. M., Rowe, J. F., Batalha, N. M., Borucki, W. J., Koch, D. G., Dunham, E. W., Gautier, III, T. N., Van Cleve, J., Cochran, W. D., Latham, D. W., Lissauer, J. J., Torres, G., Brown, T. M., Gilliland, R. L., Buchhave, L. A., Caldwell, D. A., Christensen-Dalsgaard, J., Ciardi, D., Fressin, F., Haas, M. R., Howell, S. B., Kjeldsen, H., Seager, S., Rogers, L., Sasselov, D. D., Steffen, J. H., Basri, G. S., Charbonneau, D., Christiansen, J., Clarke, B., Dupree, A., Fabrycky, D. C., Fischer, D. A., Ford, E. B., Fortney, J. J., Tarter, J., Girouard, F. R., Holman, M. J., Johnson, J. A., Klaus, T. C., Machalek, P., Moorhead, A. V., Morehead, R. C., Ragozzine, D., Tenenbaum, P., Twicken, J. D., Quinn, S. N., Isaacson, H., Shporer, A., Lucas, P. W., Walkowicz, L. M., Welsh, W. F., Boss, A., Devore, E., Gould, A., Smith, J. C., Morris, R. L., Prsa, A., Morton, T. D., Still, M., Thompson, S. E., Mullally, F., Endl, M., and MacQueen, P. J.: 2012, *Astrophys. J., Suppl. Ser.* **201**, 15

Howard, A. W., Marcy, G. W., Johnson, J. A., Fischer, D. A., Wright, J. T., Isaacson, H., Valenti, J. A., Anderson, J., Lin, D. N. C., and Ida, S.: 2010, *Science* **330**, 653

Huang, C., Wu, Y., and Triaud, A. H. M. J.: 2016, *Astrophys. J.* **825**, 98

Ida, S. and Lin, D. N. C.: 2004a, *Astrophys. J.* **604**, 388

Ida, S. and Lin, D. N. C.: 2004b, *Astrophys. J.* **616**, 567

Ikoma, M., Nakazawa, K., and Emori, H.: 2000, *Astrophys. J.* **537**, 1013

Janson, M.: 2013, *Astrophys. J.* 774

Johansen, A., Davies, M. B., Church, R. P., and Holmelin, V.: 2012, *Astrophys. J.* **758**, 39

Kahan, W.: 1965, *Communications of the ACM* **8(1)**, 40

Kaib, N. A., Raymond, S. N., and Duncan, M. J.: 2011, *Astrophys. J., Lett.* **742**, L24

Kenyon, S. J. and Bromley, B. C.: 2006, *Astron. J.* **131**, 1837

Kokubo, E., Kominami, J., and Ida, S.: 2006, *Astrophys. J.* **642**, 1131

Kozai, Y.: 1962, *Astron. J.* **67**, 591

Lai, D.: 2014, *MNRAS* **440**, 3532

Laskar, J.: 1985, *Astron. Astrophys.* **144**, 133

Laskar, J.: 1986, *Astron. Astrophys.* **157**, 59

Laskar, J.: 1994, *Astron. Astrophys.* **287**, L9

Latham, D. W., Rowe, J. F., Quinn, S. N., Batalha, N. M., Borucki, W. J., Brown, T. M., Bryson, S. T., Buchhave, L. A., Caldwell, D. A., Carter, J. A., Christiansen, J. L., Ciardi, D. R., Cochran, W. D., Dunham, E. W., Fabrycky, D. C., Ford, E. B., Gautier, Thomas N., I., Gilliland, R. L., Holman, M. J., Howell, S. B., Ibrahim, K. A., Isaacson, H., Jenkins, J. M., Koch, D. G., Lissauer, J. J., Marcy, G. W., Quintana, E. V., Ragozzine, D., Sasselov, D., Shporer, A., Steffen, J. H., Welsh, W. F., and Wohler, B.: 2011, *Astrophys. J.* **732**, L24

Laughlin, G. and Chambers, J. E.: 2002, *Astron. J.* **124**, 592

Lee, E. J., Chiang, E., and Ormel, C. W.: 2014, *Astrophys. J.* **797**, 95

Lee, M. H. and Peale, S. J.: 2002, *Astrophys. J.* **567**, 596

Leleu, A., Robutel, P., and Correia, A. C. M.: 2015, *Astron. Astrophys.* 581

Lidov, M. L.: 1962, *Planetary and Space Science* **9**, 719

Lillo-Box, J., Barrado, D., Figueira, P., Leleu, A., Santos, N. C., Correia, A. C. M., Robutel, P., and Faria, J. P.: 2018, *Astron. Astrophys.* 609

Lin, D. N. C., Bodenheimer, P., and Richardson, D. C.: 1996, *Nature* **380**, 606

Lin, D. N. C. and Papaloizou, J.: 1986, *Astrophys. J.* **309**, 846

Lissauer, J.: 2018, in *American Astronomical Society, DDA meeting #49, id. #300.04*

Lissauer, J. J.: 1993, *Ann. Rev. of Astron. Astrophys.* **31**, 129

Lissauer, J. J., Dawson, R. I., and Tremaine, S.: 2014a, *Nature* **513**, 336

Lissauer, J. J., Fabrycky, D. C., Ford, E. B., Borucki, W. J., Fressin, F., Marcy, G. W., Orosz, J. A., Rowe, J. F., Torres, G., Welsh, W. F., Batalha, N. M., Bryson, S. T., Buchhave, L. A., Caldwell, D. A., Carter, J. A., Charbonneau, D., Christiansen, J. L., Cochran, W. D., Desert, J.-M., Dunham, E. W., Fanelli, M. N., Fortney, J. J., Gautier, III, T. N., Geary, J. C., Gilliland, R. L., Haas, M. R., Hall, J. R., Holman, M. J., Koch, D. G., Latham, D. W., Lopez, E., McCauliff, S., Miller, N., Morehead, R. C., Quintana, E. V., Ragozzine, D., Sasselov, D., Short, D. R., and Steffen, J. H.: 2011a, *Nature* **470**, 53

Lissauer, J. J., Jontof-Hutter, D., Rowe, J. F., Fabrycky, D. C., Lopez, E. D., Agol, E., Marcy, G. W., Deck, K. M., Fischer, D. A., Fortney, J. J., Howell, S. B., Isaacson, H., Jenkins, J. M., Kolbl, R., Sasselov, D., Short, D. R., and Welsh, W. F.: 2013, *Astrophys. J.* **770**, 131

Lissauer, J. J., Marcy, G. W., Bryson, S. T., Rowe, J. F., Jontof-Hutter, D., Agol, E., Borucki, W. J., Carter, J. A., Ford, E. B., Gilliland, R. L., Kolbl, R., Star, K. M., Steffen, J. H., and Torres, G.: 2014b, *Astrophys. J.* **784**, 44

Lissauer, J. J., Marcy, G. W., Rowe, J. F., Bryson, S. T., Adams, E., Buchhave, L. A., Ciardi, D. R., Cochran, W. D., Fabrycky, D. C., Ford, E. B., Fressin, F., Geary, J., Gilliland, R. L., Holman, M. J., Howell, S. B., Jenkins, J. M., Kinemuchi, K., Koch, D. G., Morehead, R. C., Ragozzine, D., Seader, S. E., Tanenbaum, P. G., Torres, G., and Twicken, J. D.: 2012, *Astrophys. J.* **750**, 112

Lissauer, J. J., Ragozzine, D., Fabrycky, D. C., Steffen, J. H., Ford, E. B., Jenkins, J. M., Shporer, A., Holman, M. J., Rowe, J. F., Quintana, E. V., Batalha, N. M., Borucki, W. J., Bryson, S. T., Caldwell, D. A., Carter, J. A., Ciardi, D., Dunham, E. W., Fortney, J. J., Gautier, III, T. N., Howell, S. B., Koch, D. G., Latham, D. W., Marcy, G. W., Morehead, R. C., and Sasselov, D.: 2011b, *Astrophys. J., Suppl. Ser.* **197**, 8

Lithwick, Y. and Wu, Y.: 2011, *Astrophys. J.* **739**, 31

Lopez, E. D. and Fortney, J. J.: 2014, *Astrophys. J.* **792**, 1

Madhusudhan, N. and Winn, J. N.: 2009, *Astrophys. J.* **693**, 784

Mahajan, N. and Wu, Y.: 2014, *Astrophys. J.* **795**, 32

Malhotra, R., Fox, K., Murray, C. D., and Nicholson, P. D.: 1989, *Astron. Astrophys.* **221**, 348

Mamajek, E. E.: 2009, in T. Usuda, M. Tamura, and M. Ishii (eds.), *American Institute of Physics Conference Series*, Vol. 1158 of *American Institute of Physics Conference Series*, pp 3–10

Marzari, F.: 2014, *MNRAS* **442**, 1110

Masset, F. S., D'Angelo, G., and Kley, W.: 2006, *Astrophys. J.* **652**, 730

Mayor, M., Marmier, M., Lovis, C., Udry, S., Ségransan, D., Pepe, F., Benz, W., Bertaux, J. ., Bouchy, F., Dumusque, X., Lo Curto, G., Mordasini, C., Queloz, D., and Santos, N. C.: 2011, *ArXiv e-prints*

Mayor, M. and Queloz, D.: 1995, *Nature* **378**, 355

Mizuno, H.: 1980, *Progress of Theoretical Physics* **64**, 544

Moorhead, A. V. and Adams, F. C.: 2005, *Icarus* **178**, 517

Morton, T. D., Bryson, S. T., Coughlin, J. L., Rowe, J. F., Ravichandran, G., Petigura, E. A., Haas, M. R., and Batalha, N. M.: 2016, *Astrophys. J.* **822**, 86

Murray, C. D. and Dermott, S. F.: 2000, *Solar System Dynamics*, Cambridge University Press

NASA Exoplanet Archive: 2018, *Exoplanet and Candidate Statistics*, Online

Nobili, A. and Roxburgh, I. W.: 1986, in J. Kovalevsky and V. A. Brumberg (eds.), *Relativity in Celestial Mechanics and Astrometry. High Precision Dynamical Theories and Observational Verifications*, Vol. 114 of *IAU Symposium*, pp 105–110

Obertas, A., Van Laerhoven, C., and Tamayo, D.: 2017, *Icarus* **293**, 52

Ogilvie, G. I.: 2014, *Ann. Rev. of Astron. Astrophys.* **52**, 171

Paardekooper, S. J., Baruteau, C., Crida, A., and Kley, W.: 2010, *MNRAS* **401**, 1950

Paardekooper, S. J., Baruteau, C., and Kley, W.: 2011, *MNRAS* **410**, 293

Paardekooper, S. J. and Mellema, G.: 2006, *Astron. Astrophys.* **459**, L17

Papaloizou, J. C. B. and Larwood, J. D.: 2000, *MNRAS* **315**, 823

Perryman, M. A.: 2011, *The exoplanet handbook*, Cambridge University Press, Cambridge, New York

Petigura, E. A., Marcy, G. W., and Howard, A. W.: 2013, *Astrophys. J.* **770**, 69

Petigura, E. A., Marcy, G. W., Winn, J. N., Weiss, L. M., Fulton, B. J., Howard, A. W., Sinukoff, E., Isaacson, H., Morton, T. D., and Johnson, J. A.: 2018, *Astron. J.* **155**, 89

Piso, A.-M. A., Youdin, A. N., and Murray-Clay, R. A.: 2015, *Astrophys. J.* 800

Pollack, J. B., Hubickyj, O., Bodenheimer, P., Lissauer, J. J., Podolak, M., and Greenzweig, Y.: 1996, *Icarus* **124**, 62

Press, W. H., Teukolsky, S. A., Vetterling, W. T., and Flannery, B. P.: 1992a, *Numerical Recipes in C*, Chapt. 16.4, Cambridge University Press

Press, W. H., Teukolsky, S. A., Vetterling, W. T., and Flannery, B. P.: 1992b, *Numerical Recipes in C*, Cambridge University Press

Pu, B. and Wu, Y.: 2015, *Astrophys. J.* **807**, 44

Rafikov, R. R.: 2006, *Astrophys. J.* **648**, 666

Rafikov, R. R.: 2011, *Astrophys. J.* 727

Rasio, F. A. and Ford, E. B.: 1996, *Science* **274**, 954

Raymond, S. N.: 2010, *Formation and Evolution of Exoplanets*, Chapt. Formation of Terrestrial Planets, pp 123–144, Wiley Online Library

Raymond, S. N., Kokubo, E., Morbidelli, A., Morishima, R., and Walsh, K. J.: 2014, *Protostars and Planets VI* pp 595–618

Rein, H. and Spiegel, D. S.: 2015, *MNRAS* **446**, 1424

Rogers, L. A.: 2015, *Astrophys. J.* **801**, 41

Rogers, L. A. and Seager, S.: 2010a, *Astrophys. J.* **712**, 974

Rogers, L. A. and Seager, S.: 2010b, *Astrophys. J.* **716**, 1208

Rogers, T. M., Lin, D. N. C., and Lau, H. H. B.: 2012, *Astrophys. J., Lett.* **758**, L6

Rogers, T. M., Lin, D. N. C., McElwaine, J. N., and Lau, H. H. B.: 2013, *Astrophys. J.* **772**, 21

Rowe, J. F., Bryson, S. T., Marcy, G. W., Lissauer, J. J., Jontof-Hutter, D., Mullally, F., Gilliland, R. L., Issacson, H., Ford, E., Howell, S. B., Borucki, W. J., Haas, M., Huber, D., Steffen, J. H., Thompson, S. E., Quintana, E., Barclay, T., Still, M., Fortney, J., Gautier, III, T. N., Hunter, R., Caldwell, D. A., Ciardi, D. R., Devore, E., Cochran, W., Jenkins, J., Agol, E., Carter, J. A., and Geary, J.: 2014, *Astrophys. J.* **784**, 45

Santerne, A., Moutou, C., Tsantaki, M., Bouchy, F., Hébrard, G., Adibekyan, V., Almenara, J. M., Amard, L., Barros, S. C. C., Boisse, I., Bonomo, A. S., Bruno, G., Courcol, B., Deleuil, M., Demangeon, O., Díaz, R. F., Guillot, T., Havel, M., Montagnier, G., Rajpurohit, A. S., Rey, J., and Santos, N. C.: 2016, *Astron. Astrophys.* 587

Santos, N. C., Israelian, G., and Mayor, M.: 2004, *Astron. Astrophys.* **415**, 1153

Schmitt, J. R., Wang, J., Fischer, D. A., Jek, K. J., Moriarty, J. C., Boyajian, T. S., Schwamb, M. E., Lintott, C., Lynn, S., Smith, A. M., Parrish, M., Schawinski, K., Simpson, R., LaCourse, D., Omohundro, M. R., Winarski, T., Goodman, S. J., Jebson, T., Schwengeler, H. M., Paterson, D. A., Sejpka, J., Terentev, I., Jacobs, T., Alsaadi, N., Bailey, R. C., Ginman, T., Granado, P., Vonstad Guttormsen, K., Mallia, F., Papillon, A. L., Rossi, F., and Socolovsky, M.: 2014, *Astron. J.* **148**, 28

Schneider, J., Dedieu, C., Le Sidaner, P., Savalle, R., and Zolotukhin, I.: 2011, *Astron. Astrophys.* **532**, A79

Schwarz, R., Bazsó, Á., Funk, B., and Zechner, R.: 2015, *MNRAS* **453**, 2308

Shallue, C. J. and Vanderburg, A.: 2018, *Astron. J.* **155**, 94

Sinukoff, E., Howard, A. W., Petigura, E. A., Fulton, B. J., Crossfield, I. J. M., Isaacson, H., Gonzales, E., Crepp, J. R., Brewer, J. M., Hirsch, L., Weiss, L. M., Ciardi, D. R., Schlieder, J. E., Benneke, B., Christiansen, J. L., Dressing, C. D., Hansen, B. M. S., Knutson, H. A., Kosiarek, M., Livingston, J. H., Greene, T. P., Rogers, L. A., and Lépine, S.: 2017, *Astron. J.* 153

Smith, A. W. and Lissauer, J. J.: 2009, *Icarus* **201**, 381

Southworth, J.: 2011, *MNRAS* **417**, 2166, Last modified: 2017/05/06

Steffen, J. H. and Agol, E.: 2005, *MNRAS* **364**, L96

Steffen, J. H., Ragozzine, D., Fabrycky, D. C., Carter, J. A., Ford, E. B., Holman, M. J., Rowe, J. F., Welsh, W. F., Borucki, W. J., Boss, A. P., Ciardi, D. R., and Quinn, S. N.: 2012, *Proceedings of the National Academy of Science* **109**, 7982

Stevenson, D. J.: 1982, *Planetary and Space Science* **30**, 755

Stoer, J. and Bulirsch, R.: 1980, *Introduction to Numerical Analysis*, Chapt. 7.2.14, New York: Springer-Verlag

Tan, J. C., Chatterjee, S., Hu, X., Zhu, Z., and Mohanty, S.: 2015, *ArXiv e-prints*

Tanaka, H. and Ward, W. R.: 2004, *Astrophys. J.* **602**, 388

Teachey, A. and Kipping, D. M.: 2018, *Science Advances* 4(10)

Teachey, A., Kipping, D. M., and Schmitt, A. R.: 2018, *Astron. J.* **155**, 36

Tremaine, S. and Dong, S.: 2012, *Astron. J.* **143**, 94

Udry, S., Mayor, M., and Santos, N. C.: 2003, *Astron. Astrophys.* **407**, 369

Valencia, D., O'Connell, R. J., and Sasselov, D.: 2006, *Icarus* **181**, 545

Vokrouhlický, D. and Nesvorný, D.: 2014, *Astrophys. J.* 791

Volk, K. and Gladman, B.: 2015, *Astrophys. J., Lett.* **806**, L26

Wadhwa, M., Amelin, Y., Davis, A. M., Lugmair, G. W., Meyer, B., Gounelle, M., and Desch, S. J.: 2007, in B. Reipurth, D. Jewitt, and K. Keil (eds.), *Protostars and Planets V*, p. 835

Ward, W. R.: 1997, *Icarus* **126**, 261

Weidenschilling, S. J.: 1977a, *MNRAS* **180**, 57

Weidenschilling, S. J.: 1977b, *Astrophys. J., Suppl. Ser.* **51**, 153

Weidenschilling, S. J. and Marzari, F.: 1996, *Nature* **384**, 619

Weiss, L. M. and Marcy, G. W.: 2014, *Astrophys. J.* **783**, L6

Weiss, L. M., Marcy, G. W., Petigura, E. A., Fulton, B. J., Howard, A. W., Winn, J. N., Isaacson, H. T., Morton, T. D., Hirsch, L. A., Sinukoff, E. J., Cumming, A., Hebb, L., and Cargile, P. A.: 2018, *Astron. J.* **155**, 48

Winn, J. N. and Fabrycky, D. C.: 2015, *Ann. Rev. of Astron. Astrophys.* **53**, 409

Winn, J. N., Noyes, R. W., Holman, M. J., Charbonneau, D., Ohta, Y., Taruya, A., Suto, Y., Narita, N., Turner, E. L., Johnson, J. A., Marcy, G. W., Butler, R. P., and Vogt, S. S.: 2005, *Astrophys. J.* **631**, 1215

Wisdom, J. and Holman, M.: 1991, *Astron. J.* **102**, 1528

Wisdom, J., Holman, M., and Touma, J.: 1996, *Fields Institute Communications* **10**, 217

Wolfgang, A., Rogers, L. A., and Ford, E. B.: 2016, *Astrophys. J.* **825**, 19

Wolszczan, A. and Frail, D. A.: 1992, *Nature* **355**, 145

Wright, J. T., Fakhouri, O., Marcy, G. W., Han, E., Feng, Y., Johnson, J. A., Howard, A. W., Fischer, D. A., Valenti, J. A., Anderson, J., and Piskunov, N.: 2011, *Publ. Astron. Soc. Pac.* **123**, 412

Wright, J. T., Marcy, G. W., Howard, A. W., Johnson, J. A., Morton, T. D., and Fischer, D. A.: 2012, *Astrophys. J.* **753**, 160

Wright, J. T., Upadhyay, S., Marcy, G. W., Fischer, D. A., Ford, E. B., and Johnson, J. A.: 2009, *Astrophys. J.* **693**, 1084

Wu, Y. and Lithwick, Y.: 2013, *Astrophys. J.* **772**, 74

Zapolsky, H. S. and Salpeter, E. E.: 1969, *Astrophys. J.* **158**, 809

Zsom, A. and Dullemond, C. P.: 2008, *Astron. Astrophys.* **489**, 931

Appendix A

Complementary material

A.1 Laplace-Lagrange literal expansion of the disturbing function.

A.1.1 Direct term

The literal expansion of the direct term in disturbing function to second-order in inclination and eccentricity, and first in masses, is

$$
\begin{aligned}
\mathcal{R}_{\mathrm{D}} = & \left\{ \frac{1}{2} b_{1/2}^{(k)} + \frac{1}{8}\left(e_i^2 + e_j^2\right)\left(-4k^2 + 2\alpha D + \alpha^2 D^2\right) b_{1/2}^{(k)} \right. \\
& \left. - \frac{1}{4}\alpha\left(s_i^2 + s_j^2\right)\left(b_{3/2}^{(k-1)} + b_{3/2}^{(k+1)}\right)\right\} \cos(k\lambda_j - k\lambda_i) \\
& + \left\{ \frac{1}{4}\, e_i e_j \left(2 + 6k + 4k^2 - 2\alpha D - \alpha^2 D^2\right) b_{1/2}^{(k+1)} \right\} \cos(k\lambda_j - k\lambda_i + \varpi_j - \varpi_i) \\
& + \left\{ s_i s_j \, \alpha \, b_{3/2}^{(k+1)} \right\} \cos(k\lambda_j - k\lambda_i + \Omega_j - \Omega_i) \\
& + \left\{ \frac{1}{2} e_i \left(-2k - \alpha D\right) b_{1/2}^{(k)} \right\} \cos(k\lambda_j - (k-1)\lambda_i - \varpi_i) \\
& + \left\{ \frac{1}{2} e_j \left(-1 + 2k + \alpha D\right) b_{1/2}^{(k-1)} \right\} \cos(k\lambda_j - (k-1)\lambda_i - \varpi_j) \\
& + \left\{ \frac{1}{8} e_i^2 \left(-5k + 4k^2 - 2\alpha D + 4k\alpha D + \alpha^2 D^2\right) b_{1/2}^{(k)} \right\} \cos(k\lambda_j - (k-2)\lambda_i - 2\varpi_i) \\
& + \left\{ \frac{1}{4} e_i e_j \left(-2 - 6k - 4k^2 + 2\alpha D - 4k\alpha D - \alpha^2 D^2\right) b_{1/2}^{(k-1)} \right\} \\
& \quad \times \cos(k\lambda_j - (k-2)\lambda_i - \varpi_j - \varpi_i) \\
& + \left\{ \frac{1}{8} e_j^2 \left(2 - 7k + 4k^2 - 2\alpha D + 4k\alpha D + \alpha^2 D^2\right) b_{1/2}^{(k-2)} \right\} \cos(k\lambda_j - (k-2)\lambda_i - 2\varpi_j) \\
& + \left\{ \frac{1}{2} s_i^2 \, \alpha \, b_{3/2}^{(k-1)} \right\} \cos(k\lambda_j - (k-2)\lambda_i - 2\Omega_i) \\
& - \left\{ s_i s_j \, \alpha \, b_{3/2}^{(k-1)} \right\} \cos(k\lambda_j - (k-2)\lambda_i - \Omega_j - \Omega_i) \\
& + \left\{ \frac{1}{2} s_j^2 \, \alpha \, b_{3/2}^{(k-1)} \right\} \cos(k\lambda_j - (k-2)\lambda_i - 2\Omega_j). \qquad \text{(A.1)}
\end{aligned}
$$

Here, $s_k = \sin\dfrac{I_k}{2}$ for bodies $k = i, j$ and inclination I_k.

A.1.2 Indirect terms

Similarly, the explicit expansion of the external indirect term is

$$
\begin{aligned}
\mathcal{R}_\mathrm{E} \approx & \left[-1 + \frac{1}{2}(e_i^2 + e_j^2) + s_i^2 + s_j^2\right]\cos(\lambda_j - \lambda_i) \\
& - e_i e_j \cos(2\lambda_j - 2\lambda_i - \varpi_j + \varpi_i) - 2\, s_i s_j \cos(\lambda_j - \lambda_i - \Omega_j + \Omega_i) \\
& - \frac{1}{2}\, e_i \cos(\lambda_j - 2\lambda_i + \varpi_i) - \frac{3}{2}\, e_i \cos(\lambda_j - \varpi_i) - 2\, e_j \cos(2\lambda_j - \lambda_i - \varpi_j) \\
& - \frac{3}{8}\, e_i^2 \cos(\lambda_j - 3\lambda_i + 2\varpi_i) - \frac{1}{8}\, e_i^2 \cos(\lambda_j + \lambda_i - 2\varpi_i) \\
& + 3\, e_i e_j \cos(2\lambda_i - \varpi_j - \varpi_i) - \frac{1}{8}\, e_j^2 \cos(\lambda_j + \lambda_i - 2\varpi_j) \\
& - \frac{27}{8}\, e_j^2 \cos(3\lambda_j - \lambda_i - 2\varpi_j) - s_i^2 \cos(\lambda_j + \lambda_i - 2\Omega_i) \\
& + 2\, s_i s_j \cos(\lambda_j + \lambda_i - \Omega_j - \lambda_i) - s_j^2 \cos(\lambda_j + \lambda_i - 2\Omega_j).
\end{aligned} \tag{A.2}
$$

Finally, the internal indirect part is

$$
\begin{aligned}
\mathcal{R}_\mathrm{I} \approx & \left[-1 + \frac{1}{2}(e_i^2 + e_j^2) + s_i^2 + s_j^2\right]\cos(\lambda_j - \lambda_i) \\
& - e_i e_j \cos(2\lambda_j - 2\lambda_i - \varpi_j + \varpi_i) - 2\, s_i s_j \cos(\lambda_j - \lambda_i - \Omega_j + \Omega_i) \\
& - 2\, e_i \cos(\lambda_j - 2\lambda_i + \varpi_i) + \frac{3}{2}\, e_i \cos(\lambda_i - \varpi_j) - \frac{1}{2}\, e_j \cos(2\lambda_j - \lambda_i - \varpi_j) \\
& - \frac{27}{8}\, e_i^2 \cos(\lambda_j - 3\lambda_i + 2\varpi_i) - \frac{1}{8}\, e_i^2 \cos(\lambda_j + \lambda_i - 2\varpi_i) \\
& + 3\, e_i e_j \cos(2\lambda_i - \varpi_j - \varpi_i) - \frac{1}{8}\, e_j^2 \cos(\lambda_j + \lambda_i - 2\varpi_j) \\
& - \frac{3}{8}\, e_j^2 \cos(3\lambda_j - \lambda_i - 2\varpi_j) - s_i^2 \cos(\lambda_j + \lambda_i - 2\Omega_i) \\
& + 2\, s_i s_j \cos(\lambda_j + \lambda_i - \Omega_j - \lambda_i) - s_j^2 \cos(\lambda_j + \lambda_i - 2\Omega_j)
\end{aligned} \tag{A.3}
$$

A.2 Laplace-Lagrange solution for more than two secondary masses.

The disturbing function for more than two secondary masses, using the Laplace-Lagrange solution is

$$
\mathcal{R}_i = n_i a_i^2 \left[\frac{1}{2} A_{ii}\, e_i^2 + \frac{1}{2} B_{ii}\, I_i^2\right.
$$

$$+ \sum_{j=1,j\neq i}^{N} A_{ij}\, e_i e_j \cos(\varpi_i - \varpi_j) + \sum_{j=1,j\neq i}^{N} B_{ij}\, I_i I_j \cos(\Omega_i - \Omega_j)\Bigg], \tag{A.4}$$

with

$$A_{ii} = \frac{1}{4}\frac{n_i}{m_c + m_i} \sum_{j=1,j\neq i}^{N} m_j\, \alpha_{ij}\, \bar{\alpha}_{ij}\, b_{3/2}^{(1)}(\alpha_{ij}) \tag{A.5}$$

$$A_{ij} = -\frac{1}{4}\frac{n_i}{m_c + m_i}\, m_j\, \alpha_{ij}\, \bar{\alpha}_{ij}\, b_{3/2}^{(2)}(\alpha_{ij}) \tag{A.6}$$

$$B_{ii} = -\frac{1}{4}\frac{n_i}{m_c + m_i} \sum_{j=1,j\neq i}^{N} m_j\, \alpha_{ij}\, \bar{\alpha}_{ij}\, b_{3/2}^{(1)}(\alpha_{ij}) \tag{A.7}$$

$$B_{ij} = \frac{1}{4}\frac{n_i}{m_c + m_i}\, m_j\, \alpha_{ij}\, \bar{\alpha}_{ij}\, b_{3/2}^{(1)}(\alpha_{ij}) \tag{A.8}$$

where

$$\alpha_{ij} = \begin{cases} a_j/a_i & \text{internal perturber, if } a_i > a_j \\ a_i/a_j & \text{external perturber, if } a_i < a_j \end{cases}, \tag{A.9}$$

and

$$\bar{\alpha}_{ij} = \begin{cases} 1 & \text{internal perturber, if } a_i > a_j \\ a_i/a_j & \text{external perturber, if } a_i < a_j \end{cases}, \tag{A.10}$$

Using the eccentricity and inclination vector definitions, Eq. A.4 transforms to

$$\mathcal{R}_i = n_i a_i^2 \Bigg[\frac{1}{2} A_{ii}\,(h_i^2 + k_i^2) + \frac{1}{2} B_{ii}\,(p_i^2 + q_i^2)$$
$$+ \sum_{j=1,j\neq i}^{N} A_{ij}\,(h_i h_j + k_i k_j) + \sum_{j=1,j\neq i}^{N} B_{ij}\,(p_i p_j + q_i q_j)\Bigg],. \tag{A.11}$$

According to Brouwer and Clemence (1961) the derivatives of the eccentricity and inclination vector in Eq. A.11 are

$$\dot{h}_i = A_{ii}\, k_i + \sum_{j=1,j\neq i}^{N} A_{ij}\, k_j \tag{A.12}$$

$$\dot{k}_i = -A_{ii}\, h_i - \sum_{j=1,j\neq i}^{N} A_{ij}\, h_j \tag{A.13}$$

$$\dot{p}_i = B_{ii}\, q_i + \sum_{j=1,j\neq i}^{N} B_{ij}\, q_j \tag{A.14}$$

$$\dot{q}_i = -B_{ii}\, p_i - \sum_{j=1,j\neq i}^{N} B_{ij}\, p_j \tag{A.15}$$

and the solution changes to

$$h_i = \sum_{j=1}^{N} e_{ij} \sin(g_j\, t + \beta_j), \qquad k_i = \sum_{j=1}^{N} e_{ij} \cos(g_j\, t + \beta_j) \tag{A.16}$$

$$p_i = \sum_{j=1}^{N} I_{ij} \sin(f_j\, t + \gamma_j), \qquad q_i = \sum_{j=1}^{N} I_{ij} \cos(f_j\, t + \gamma_j) \tag{A.17}$$

The matrices **A** and **B** seen in Sect. 2.2 are still square matrices, but with $N \times N$ dimension. The process to find the eigenfrequencies, eigenvectors, forced inclination and eccentricity is the same that in Sect. 2.2 and in Murray and Dermott (2000). The subindex i indicates a body, and j the mode.

A.3 Orbital evolution of coorbital realizations in the corotating frame

(a) r-054 (b) r-628

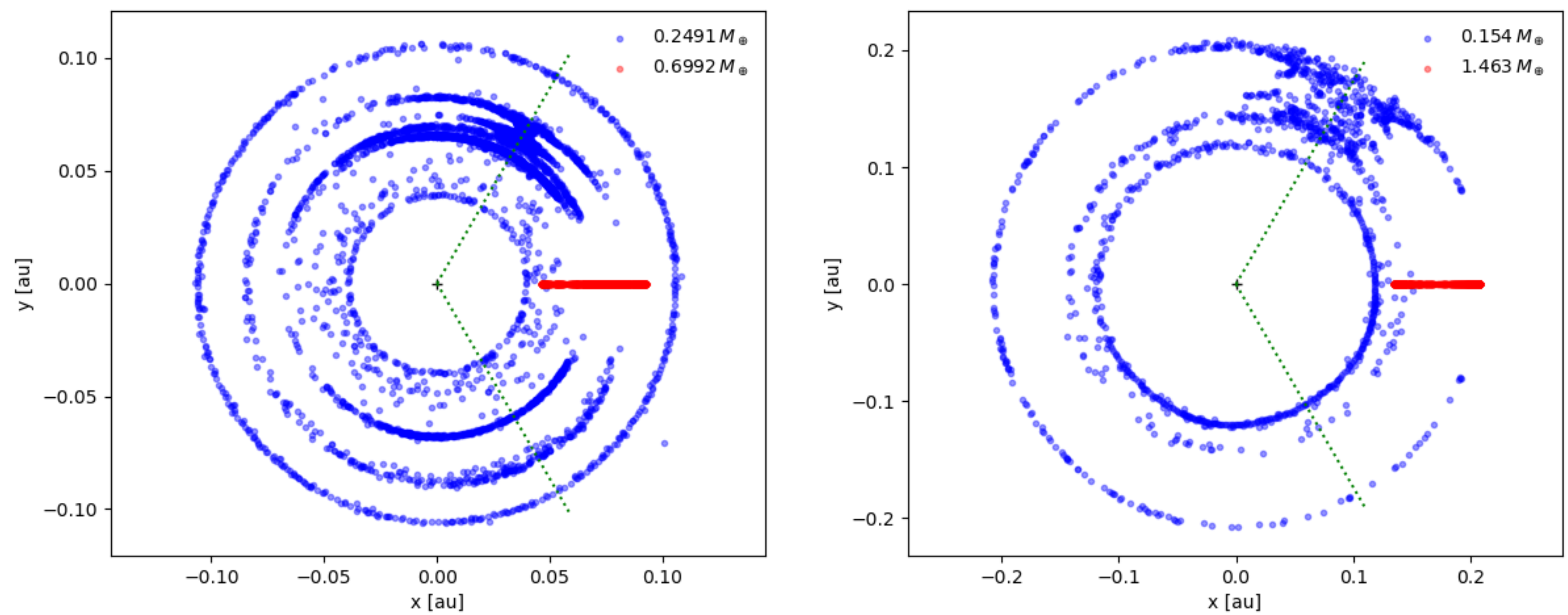

Figure A.1: Phase-on corotational evolution of the realizations in Fig. 3.12 in the frame of the larger planet. The angular location of the L4 and L5 Lagrange points are indicated as green dotted-lines. The richness of the orbital evolution in function of time is evident. In panel (a), the smaller planet, initially at a higher semi-major axis, due the eccentricity and inclination damping is forced to migrate inwards and catches up with the planet in red, resulting in a 1:1 MMR capture and shifts between tadpole and horseshoe orbits. (b) Starting at a lower semi-major axis, the smaller planet moves outwards and is trapped in a tadpole orbit than then evolves into a horseshoe.

A.4 `IAS15` integration procedure.

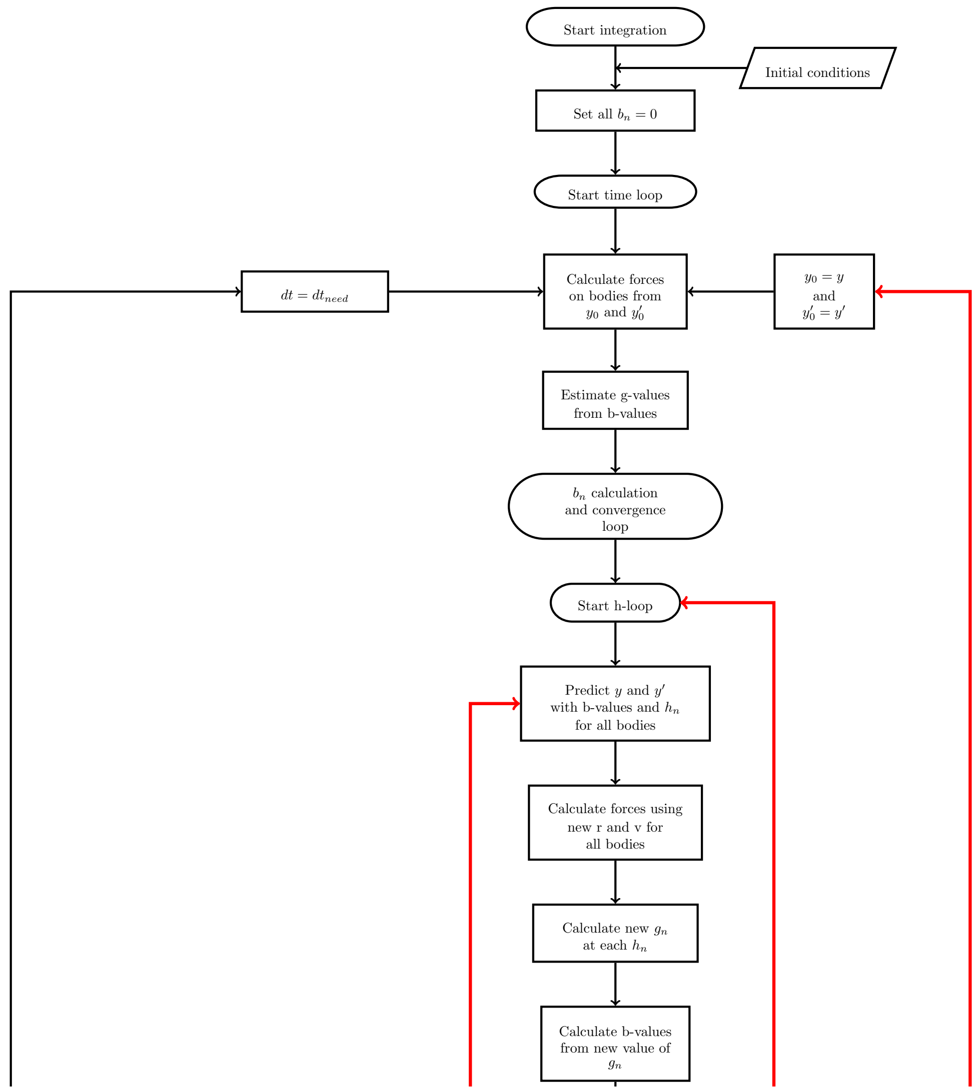

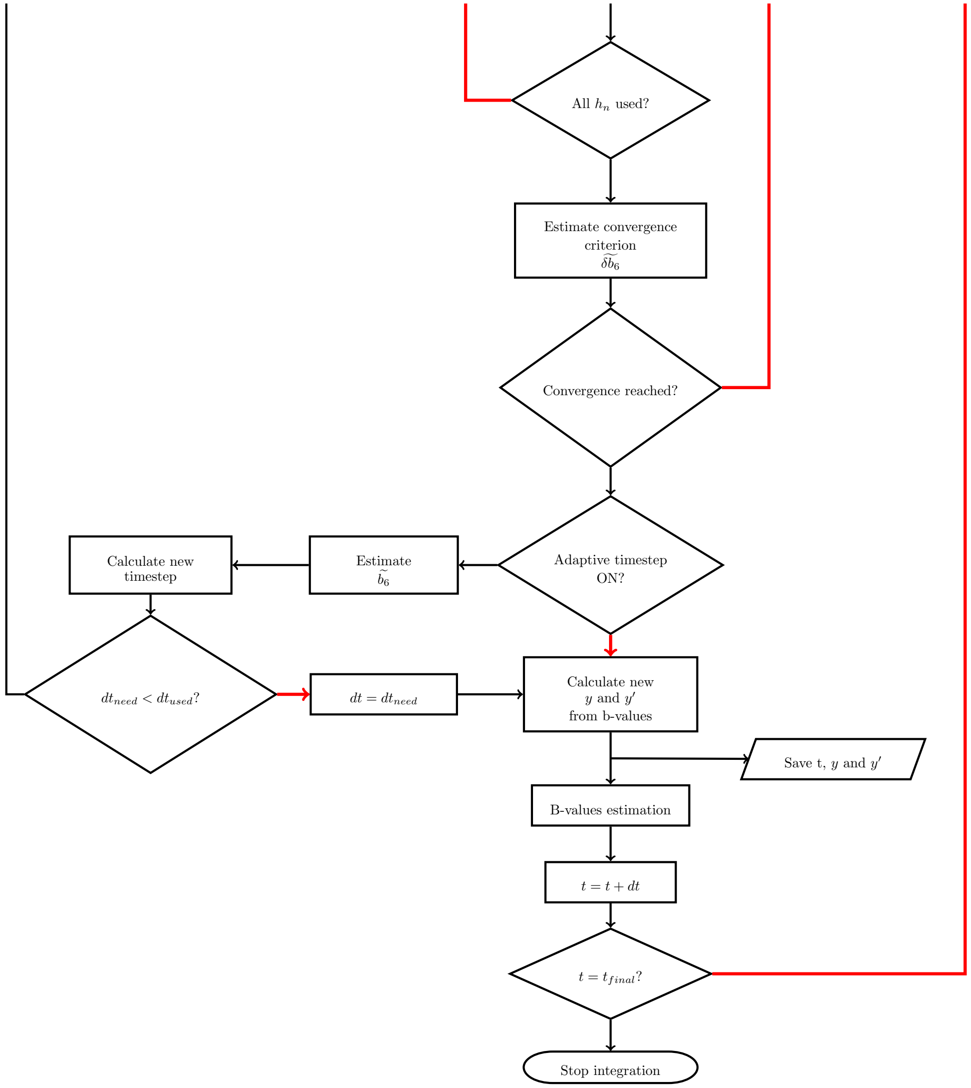

Figure A.2: `IAS15` integration procedure. The red lines represent a negative answer to the questions inside each of the decision taking rhombus.